One-dimensional beam ordering of protons at ion storage ring, S-LSR(Dissertation_全文)

AUTHOR(S):

Shirai, Toshiyuki

One-dimensional Beam Ordering of Protons at Ion Storage Ring, S-LSR

Dissertation

by

Toshiyuki SHIRAI

to

The Department of Physics
Graduate School of Science
Kyoto University

May 2007

Abstract

The ion storage ring, S-LSR has been constructed to study the beam cooling, especially for the physics of the extreme cold ion beam. The magnetic rigidity is 1 Tm and the circumference is 22.557 m. The lattice of the ring was designed to suppress the beam heating as small as possible. The construction was completed in the summer of 2005 and the beam commissioning using 7 MeV protons was started in October, 2005.

The electron cooler at S-LSR has an effective cooling length of 0.44 m (2 % of the circumference). The 7 MeV proton beam was successfully cooled in November, 2005. After the improvements and the optimization of the electron cooler, the maximum cooling force of 0.12 eV/m is achieved with the electron energy of 3.8 keV and the electron current of 56 mA. The estimated electron temperature is 25 μeV.

Since February, 2006, the one-dimensional ordering experiment of protons has been performed using the electron cooling. The first proton ordering was successfully confirmed in July, 2006. Abrupt drop in the momentum spread and the Schottky noise power have been observed at a proton number of $\sim$2000 with electron currents of 25 mA, 50 mA and 100 mA. The transition temperatures of the proton ordering are 0.17 meV and 1 meV in the longitudinal and transverse direction, respectively. The transverse proton temperature is much below the transverse electron temperature, which is the result of the magnetized electron cooling. Below the transition, the longitudinal proton temperature is cooled down to 26 μeV, which is close to the longitudinal electron temperature.

The transition temperature of the proton ordering is much lower than those of the highly charged heavy ions at ESR because of the weak Coulomb interaction. Nevertheless, the particle reflection model agrees well with the experimental result of the proton ordering. The reflection probability of the proton at the transition is close to those of the heavy ions. It shows that the one-dimensional ordering of the proton occurs by the same mechanism as the highly charged heavy ions. The beam simulations using the molecular dynamics method also agree well with the experimental results.

Contents

Chapter 1

Introduction

1.1 Beam Cooling

Charged particle beams generated by accelerators are very powerful tools in many fields, such as fundamental sciences, applied sciences, industrial and medical applications. Since the applications of particle beams spread out widely, various kinds of beams are required. Especially, a high quality beam with a small beam size and a small energy spread is preferable in many cases.

A velocity of particle beams is usually very fast (close to speed of light) in the laboratory frame. On the other hand, each particle has a small relative velocity in the particle rest frame. This relative motion of particles creates a finite beam size and energy spread of the beam. Usually, the beam quality is represented by the emittance, which is the phase space volume occupied by the particles. It is also convenient to define the beam temperature T by the velocities in the particle rest frame,

$$\frac{3}{2}k_B T = \frac{1}{2}m\langle v^2\rangle, \tag{1.1}$$

$$k_B T_x = m\langle v_x^2\rangle, \tag{1.2}$$

$$k_B T_y = m\langle v_y^2\rangle, \tag{1.3}$$

$$k_B T_s = m\langle v_s^2\rangle, \tag{1.4}$$

where k_B is the Boltzmann constant and m is the mass of the particle. $\sqrt{\langle v^2\rangle}$ is the rms velocity spread in the particle rest frame. The definition of the velocity components is shown in Fig.1.1. T_x, T_y and T_s are the beam temperature components in the x, y and s directions, respectively. The beam temperature also represents the beam quality. It is shown later that the emittance is proportional to $\langle v^2\rangle$ (see Eqs.(5.2, 5.8)).

A beam cooling is a method to improve a quality of beam stored in a circular accelerator. The phase space volume occupied by the particles is constant in accelerators according to the Liouville theorem. In order to break this restriction, the beam cooling introduces the dissipative force to the beam. It enables the reduction of the relative velocity of particles

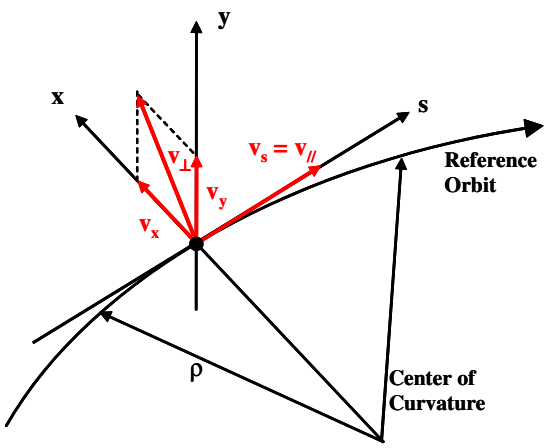

Figure 1.1: Definition of the velocity components in the particle rest frame.

and compression of the phase space volume without particle loss. As the result, the beam density is increased. It can be expressed that the beam cooling reduces the temperature of the beam.

In electron and positron storage rings, an energy spread and a beam emittance are damped by a synchrotron radiation. It is called "radiation damping" (not called "cooling"). The radiated power P_r from a charged particle with a energy E and a mass m is given by,

$$P_r = \frac{2cr_c}{3(mc^2)^3}\frac{E^4}{\rho^2}, \tag{1.5}$$

where c is the speed of light, r_c is the classical particle radius, ρ is the curvature radius of the particle motion. Because the particles with higher energy radiate more power, the energy spread is reduced. The radiation damping is a very strong tool to obtain the brilliant beam for electrons and positrons. In the linear collider, a special damping ring will be inserted between the linear accelerators to reduce the beam emittance.

However, even at very high energy (> TeV), ions are not so efficiently damped by the radiation because of their heavy mass. An artificial dissipative force is necessary for the ion beam cooling. Many people have challenged to this fascinating subject. The important step was a proposal of an "electron cooling" by G. Budker in the 1960s for the cooling of antiproton [1]. If hot ions and cold electrons overlap between each other and move with the same velocity in some distance, the heat exchange occurs through the Coulomb interaction and the hot ions are cooled. Figure 1.2 shows the illustration of this scheme. This idea was verified at NAP-M in BINP, Novosibirsk [2]. Later, the cooling experiments were performed at ICE in CERN [3] and at Test Ring in Fermilab [4].

A stochastic cooling was proposed by van der Meer around the same time [5]. It is based on a beam feedback theory. In a standard beam feedback, the position of the beam center-of-gravity is measured by a pickup and moved to the ideal orbit by a kicker. If the bandwidth of

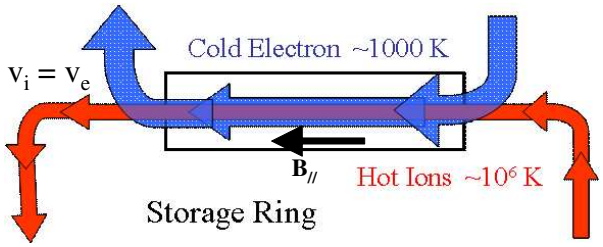

Figure 1.2: Illustration of the electron cooling.

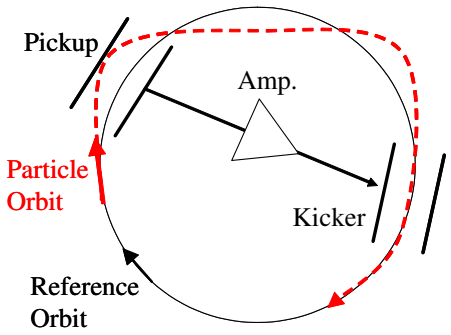

Figure 1.3: Principle of the transverse stochastic cooling.

the pickup and the kicker is infinite and a noise level in the feedback is zero, each particle in the beam moves to the center and the emittance would be zero. Figure 1.3 shows the scheme of the transverse stochastic cooling. In practice, the bandwidth and the noise level are finite, only a group of the particles is manipulated in the stochastic cooling. The stochastic cooling gave the successful result for the first antiproton cooling [6] and is widely used for the high energy cooling now.

Laser cooling is a new cooling method in the field of the accelerator. It was originally developed for ion trap. The frequency of the laser light is tuned near the transition of ions, for example 280 nm for Mg^+. In the accelerator, ions have a wide spread of the velocity, which creates the frequency spread of the absorbed light due to the Doppler shift. If the frequency of the copropagating laser light is swept, the ions get the momentum from the light and are accelerated (see Fig.1.4). Finally, the energy spread is reduced. The important features of the laser cooling are a low beam temperature and a high cooling rate.

There are also activities to develop new cooling methods. An ionization cooling for muons is a hot topic now. It is a key device for a future neutrino factory and muon collider. The verification experiments for the ionization cooling are prepared at some laboratories [7]. An optical stochastic cooling is studied to extend the bandwidth of the stochastic cooling to the optical region [8]. The applications for very high energy ions and for the damping ring of electrons are proposed. The verification experiment using the low energy electron beam is

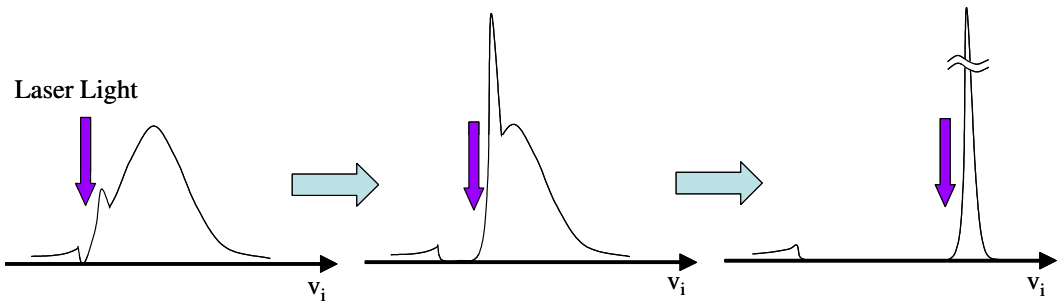

Figure 1.4: Change of the ion velocity distribution caused by the frequency sweep of the copropagating laser.

prepared at MIT-Bates [9].

Now, the beam cooling has been used for many applications from the high energy physics to low energy atomic, molecular physics. One important role of the cooling is to increase the beam density. Especially, it is crucial in collider rings. Many efforts have been continued for the high energy beam cooling. Recently, Fermilab succeeded the electron cooling of 8.9 GeV/c antiproton to increase the luminosity in Tevatron collider [10]. Another important role is to increase the intensity of the beam. If the beam volume is compressed in the phase space, a new beam can be injected into the empty space again. It was very successful for the accumulation of antiprotons and it is used in many heavy ion cooler rings. A increase of a beam lifetime is also important, especially for an internal target experiments. The beam cooling suppresses the diffusion of the beam, which is induced by collisions with a internal target and residual gas. Sometimes, an electron cooler is used as a tool for the atomic and molecular physics, because electrons in the cooler cause atomic reactions with the circulating ions. The dedicated electron cooler for this purpose is called "electron target" [11].

1.2 Ion Beam Ordering by Electron Cooling

The motivation of the study in this thesis is a realization of a high quality ion beam in an accelerator, especially for protons. The ion beam cooling is a very strong tool but the quality of the beam is limited by the equilibrium between the cooling rate and the heating (diffusion) rate by the intrabeam scattering (IBS), which is the small angle Coulomb scattering between ions. In other word, a zero-emittance beam is never realized as long as the IBS heating exists. However, if a phase transition of the beam ordering occurs at a low temperature, the IBS is suppressed and the beam heating decreases. In principle, the zero-emittance beam is possible under this condition. Such phase transitions have been observed in cold plasma of electrons and ions. The phase transition is a key concept to achieve the very high quality ion beam, combined with the beam cooling.

In order to reach the transition temperature, the beam cooling is necessary, especially the

lowest temperature is important. From this view point, the stochastic cooling is not suitable, because it takes long cooling time to achieve the low temperature beam. For example, it takes around 1000 seconds to reach the momentum spread of 1×10^{-4} ($\sim 10^5$ K) for 10^9 particles, [12]. The electron cooling is more suitable to generate the cold ions. The lowest ion temperature is determined by the electron temperature itself, which is typically 1 K in the longitudinal direction, but 1000 K in the transverse direction. The laser cooling is most suitable to achieve the low temperature beam. The limitation of the temperature comes from the random walk of the ions due to the absorption and the radiation of the light. It is around 1 mK for Mg^+ beam. However, the specific ions with a electron are necessary for the laser cooling and the proton beam cannot be cooled. The electron cooling is the only method for protons.

Concerning this subjects, the important report was presented by V.V. Parkhomchuk at the international conference on the electron cooling at Karlsruhe in 1984 (ECOOL84). This conference was held to discuss the possibilities of the electron cooling in the nuclear and atomic physics. Many new projects of the electron cooling were discussed there, such as LEAR at CERN, ESR at GSI, CELSIUS at Uppsala, COSY at Jülich, ASTRID at Aarhus, CRYRING at Stockholm, TSR at MPI-Heidelberg, IUCF cooler at Indiana and TARN-II at Tokyo [13, 14, 15]. His presentation about the NAP-M experiment received keen attention. They achieved a very small momentum spread of 1.1×10^{-6} for the proton beam at the stored current of 10μA and the momentum spread was constant below 10μA [16]. It is ruled out by the intrabeam scattering (IBS) theory [17]. From the IBS theory, the momentum spread of 1.1×10^{-6} is too small at this beam current (normally $10^{-4} - 10^{-5}$). Furthermore, it is expected from the IBS theory that the momentum spread decreases according to the reduction of the beam current, because the Coulomb collision between particles is reduced, while the electron cooling rate is constant. The Schottky noise power from the protons also decreased compared with the uncooled beam. He presented the interpretation that the cooled proton beam started ordering and the particles were equally spaced in the ring. Therefore, the intrabeam scattering was suppressed and the small momentum spread was achieved. However, there was no clear indication of the phase transition of the beam ordering and there have been discussions about the results of the proton ordering at NAP-M.

After the report from NAP-M, ordering experiments using electron cooling has been continued in other storage rings. The important achievement was reported by M. Steck at ESR [18]. As in the case of NAP-M, the momentum spread of cooled Au^{79+} was measured with reduction of the particle number. When the particle number reached 2000, the momentum spread dropped abruptly from 5×10^{-6} to 5×10^{-7}. The difference of this experiment from NAP-M were a highly charged heavy ion and a very small particle number of 4000, while the ion was the single charge proton and the particle number was 10^7 at NAP-M. This sudden drop of the momentum spread was considered to be an indication of the phase transition of ordering. After the experiments at ESR, similar transitions for highly charged heavy ions

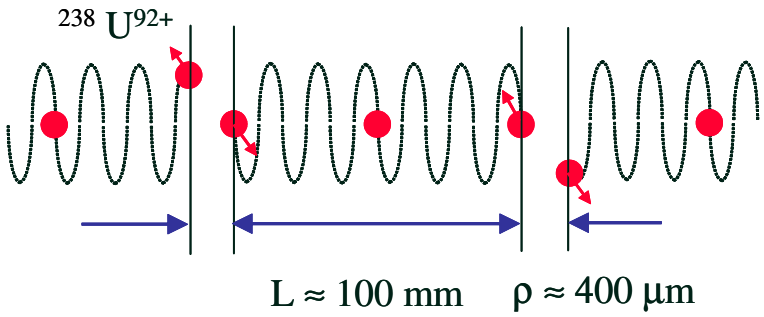

Figure 1.5: Illustration of the model of the one-dimensional beam ordering.

were found at CRYRING by H. Danared [19] and at SIS [20]. SIS is a high energy heavy ion synchrotron at GSI and equipped with an electron cooler.

The well-known parameter to show the relation between the kinetic energy and the Coulomb interaction is a plasma parameter Γ,

$$\Gamma = \frac{(Ze)^2}{4\pi\epsilon_0 d}\frac{1}{k_B T}, \tag{1.6}$$

where Ze is the ion charge, T is the beam temperature and d is the average inter-particle distance. In order to align the ions with the same inter-particle distance in the ring, the plasma parameter must be larger than 1. From the experimental data of U^{92+} at ESR, the longitudinal temperature was 300 K and the average inter-particle distance was 100 mm. The plasma parameter was only $\Gamma \cong 4 \times 10^{-3}$ below the jump of the momentum spread. It suggests that the influence of the Coulomb interaction was very weak.

Concerning this phenomenon, many theoretical works were performed by analytical methods and by numerical simulations. R.W. Hasse proposed a particle reflection model [21]. When the beam is cooled down to a certain temperature with a low density, the particles cannot pass through each other (or reflect) in the longitudinal direction due to the Coulomb potential barrier. On the other hand, when the particles are far from each other, they move freely in the longitudinal direction. Figure 1.5 shows an illustration of this model. The transverse oscillation is a betatron one. Although the position of the particles is not fixed in the particle rest frame and the inter-particle distance is not constant, they are confined in the longitudinal direction. Therefore, the intrabeam scattering is suppressed. He calculated the reflection probability in the longitudinal direction using Monte Carlo simulation. The transition temperature at ESR coincides with the threshold value of the reflection. Now, it is considered that this phenomenon is a string-like ordering and it is called "one-dimensional beam ordering".

The one-dimensional beam ordering of U^{92+}, Pb^{55+}, Au^{79+}, Xe^{54+}, Kr^{36+}, Zn^{30+}, Ni^{17+}, Ar^{18+} was found at ESR, SIS and CRYRING [18, 19, 22]. Recently, the ordering of C^{6+}

was found at ESR, which was the lightest ordered ion [22]. However, the ordering of single charged ions and lighter ions than carbon was not found.

1.3 One-dimensional Ordering of Protons

Since the NAP-M experiment, the ordering of protons has been a big question. The ordering experiment of protons has been performed at COSY but the jump of the momentum spread has not been observed [23]. The momentum spread became constant at 2×10^{-6} at the proton number of 2×10^{5}.

Even if the phase transition of the proton ordering occurs, the lower transition temperature is expected, because the Coulomb interaction of protons is much smaller than that of the highly charged heavy ions, which is proportional to Z^2. For the proton ordering, the low electron temperature in the cooler and the small heating in the ring are necessary. The high stability of the cooler and the ring is also required. In other word, if the ordering of protons is achieved, the ordering of most of ions would be possible, including antiprotons.

We have performed the experiment of the one-dimensional ordering of protons at Small-Laser Storage Ring (S-LSR) at Institute for Chemical Research, Kyoto University [24]. S-LSR is the first storage ring optimized for the high space charge beam. The lattice of the ring is designed so that the betatron tune in a superperiod becomes as small as possible. It is essentially important to avoid the resonance heating due to the space charge. It also has a small magnetic field error and a stable power supply. As the results, the drift and the orbit distortion are small, and the stopband of the resonance is also small. It is an advantage over the existing cooler rings such as COSY. In the summer of 2006, we have succeeded to achieve the proton ordering for the first time. This result is the main subject in this thesis.

1.4 Outline of Thesis

This thesis has six main chapters. Chapter 2 described the details of the design, the construction and the commissioning of the ion storage ring, S-LSR. It is the first storage ring, optimized for the high space charge beam. The related points are mainly described. Chapter 3 introduces the electron cooler at S-LSR. For the beam ordering, the important parameters are a cooling force and an electron temperature. The design and the measurement are presented. Chapter 4 contains the beam monitors for the ordering experiment. The beam properties, such as a particle number, a momentum spread and a beam size have to be measured at 1000 protons. Because the beam signal is proportional to Z^2, it is much more difficult than highly charged ions. The details of each monitor are presented. Chapter 5 shows the experimental results of the proton ordering. The essence of the results was published in Ref.[25]. The more details are described in this chapter. In Chapter 6, the comparisons of the experimental results with the ordering model and the MD simulations are discussed. The

comparison between the proton and the heavy ions and the relation between the ordered beam and the crystalline beam are also discussed.

Chapter 2

Ion Storage Ring, S-LSR

A storage ring is a dedicated accelerator to store a charged particle beam for a certain period. The ion storage ring, S-LSR stored 7 MeV proton beam for the electron cooling and 40 keV Mg^+ beam for the laser cooling. It has been constructed to study a beam physics and applications of cooled beams, especially the study of an extreme cold ion beam.

In order to obtain a cold ion beam, not only cooling devices, but also a storage ring is very important, because the cooling is easily disturbed by the heating from the space charge of the beam and the imperfection of the magnetic field in the ring. How to realize a "non-heating" storage ring is a key issue for the S-LSR project. Major source of the beam heating is a betatron resonance of the ring. Even if an initial betatron tune is far away from resonances, a cooled beam crosses the resonance due to a space charge tune shift, because it has a high space charge density. The details of the resonance and the space charge tune shift are described in Appendix B.2 and C.1. S-LSR is the first ring to avoid the such kind of effect by the lattice design of the ring. It is an essentially different point from the existing ring. It is described in the first section in this chapter. A strength of a resonance heating and a distortion of a beam orbit depend on field errors of the magnets. At S-LSR, many efforts have been made in order to reduce the field error by a design and a construction method of the magnets and the ring. After the brief review of the magnets, an alignment of the magnets is described in the second section. The beam commissioning results are reported in the third section.

A residual gas is also a heating source for the cooled beam. The vacuum system is out of the scope of this thesis and the present status of the vacuum condition at S-LSR is described in Ref.[26]. The average vacuum pressure in the ring was less than 1×10^{-8} Pa at the period of the beam ordering experiment. It is expected from the beam simulation that the residual gas heating is not crucial for 7 MeV protons at the present pressure level [27].

Most of the storage rings use only a magnetic field to bend and confine charged particle beams but recently electrostatic storage rings were built in Aarhus University [28] and KEK [29]. The electrostatic field is suitable for low energy heavy ions, especially for the heavy molecules. S-LSR has a hybrid bending element, which applies the magnetic and electric

field simultaneously. The details of the hybrid bending element is described in Ref.[30]. In this thesis, I concentrate the results using only magnetic field.

2.1 Design of S-LSR

2.1.1 Necessary Conditions for Ring

At first, let us consider the ideal storage ring in this section without a magnetic field error or a misalignment. In order to achieve a high density (high space charge) beam such as a crystalline beam, some conditions are necessary for the ring. The crystalline beam is a straightforward extension of an ion crystal in a trap, which was realized by a laser cooling [31, 32]. The crystalline beam is briefly introduced in Appendix A. These necessary conditions were found by the extensive analytical and MD simulation studies in Refs.[33, 34, 35, 36]. The conditions depend on the particle density and the crystalline beam structure (see Fig.A.1),

1. One-dimensional ordered beam or string with low beam density,
2. String crystal with high beam density and a two-dimensional structure, such as zigzag crystal,
3. A simple three-dimensional structure, such as a single shell crystal,
4. Complicated three-dimensional structure, such as two shell crystal and higher dimensional crystal.

Concerning the one-dimensional ordered beam or string with low density (case 1), there is no restriction of the betatron tune. Even after the deep cooling, the tune shift is small because of the low beam density. However, it is found that there are some engineering requirements. This kind of beam is a target of the electron cooling experiment and the requirements are discussed in the following chapters.

In order to achieve the string crystal with high beam density or zigzag crystal (case 2), the storage ring has to satisfy the so called "maintenance conditions" of a crystalline beam [33].

- The beam energy is less than the transition energy, or,

$$\gamma < \gamma_t, \tag{2.1}$$

  where γ and γ_t are the Lorentz factors of the beam and the transition energy, respectively. The definition of the transition energy is described in Appendix B.1.

- The number of the superperiod N_{sp} is,

$$N_{sp} > 2\sqrt{2} \times \nu_{x,y}. \tag{2.2}$$

The first condition comes from a criterion of the stable horizontal motion of the crystal under strong Coulomb interaction. The second condition was found by MD simulations at first. Later, it was recognized as a linear resonance (a half integer resonance) condition. When the beam density increases by the cooling, the betatron tune decreases from ν to 0, because the focusing force by the external magnetic field is canceled by the strong space charge force (see Appendix C.1). On the other hand, the coherent tune of the breathing mode decreases from 2ν to $\sqrt{2}\nu$ (see Appendix C.2). The linear resonance condition is $nN_{sp}/2$ (n =1, 2, 3 ...), when the ring has N_{sp}-fold symmetry. If the coherent tune $\sqrt{2}\nu$ is less than the lowest linear resonance $N_{sp}/2$ (n=1), the crystalline state is stable, because there is no resonance between the crystalline beam and the lattice structure. Eq.(2.2) shows this relation.

In order to create a crystal which has a horizontal structure, such as a single shell (case 3), we have to cancel a shear force. It is schematically shown in Fig.2.1. The difference of the angular velocity of each particle deforms the crystal structure and destroys it finally. It is inevitable in the magnetic storage ring. At S-LSR, the electrostatic deflectors are installed in the bending magnets in order to suppress the shear force [37]. This is out of the scope of this thesis and the experiment is ongoing now.

For more complicated crystalline beam, a more strict condition is required in addition to the above all conditions. Because the heating of the breathing mode becomes stronger, the initial coherent tune 2ν must be less than the lowest linear resonance $N_{sp}/2$. In this case, the coherent tune is always lower than the linear resonance during the cooling process. From the condition of $2\nu < N_{sp}/2$,

$$N_{sp} > 4 \times \nu_{x,y}. \tag{2.3}$$

In summary, the storage ring must satisfy the conditions of the transition energy and the betatron tune of Eqs.(2.1, 2.2, 2.3).

2.1.2 Lattice Design

From Eqs.(2.2, 2.3), a large number of the superperiod is preferable. On the other hand, the ring diameter must be less than around 7 m, because the available space of the accelerator room is 16 m $\times$ 8 m. It is also necessary that the length of a drift space in the ring is longer than 1.5 m in order to install an electron cooler. Therefore, it is difficult to design the ring with the superperiod of 8. Because the superperiod of 4 is too low symmetry, only the superperiod of 6 is possible in the available space.

The design guideline of S-LSR is following.

1. The number of the superperiod is 6.

2. The diameter of the ring is around 7 m.

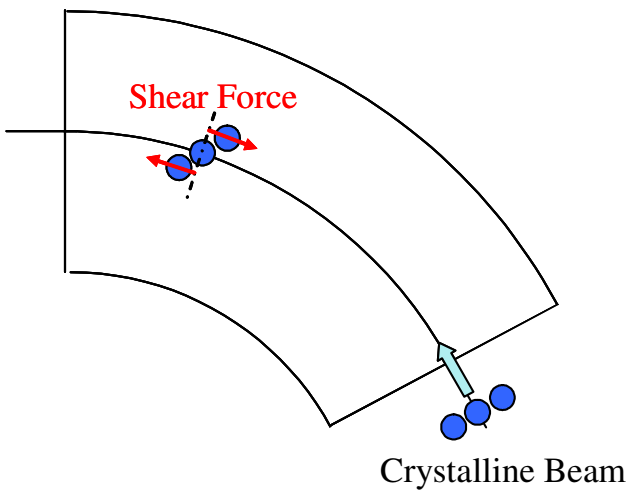

Figure 2.1: Illustration of a shear force. If the crystalline beam is bent by a magnetic field, the angular velocity difference induces the beam heating.

3. The minimum horizontal and vertical betatron tune is less than 1.5 ($=N_{sp}/4$).

4. The length of the drift space is longer than 1.5 m.

In addition, the following conditions are also preferable,

1. Small chromaticity without correction for the beam with the large momentum spread.

2. Small and smooth variation of the β-function in the ring.

Figure 2.2(a) shows an example of the design candidate [38]. The average diameter is 6.28 m and the drift space is 1.5 m. The curvature of the bending magnet is 0.9 m. The quadrupole magnet is a singlet with the length of 0.2 m. It is not a doublet, because there is no space for one more quadrupole magnet. Fig.2.2(b), (c) and (d) shows twiss parameters in one period. The twiss parameters are calculated by the program code MAD8 [39]. The differences of three cases are bending magnets. They are a bending magnet with an edge angle (b), a combined function bending magnet with n-value (c) and a bending magnet with normal entrance (d). In the case of Fig.2.2(b) and (c), the horizontal and vertical focusing are made by the bending magnets. The quadrupole magnets are used for the betatron tune adjustment for the experiments. In the case of Fig.2.2(d), the horizontal focusing is made by the radial focusing of the bending magnets and the vertical focusing is made by the quadrupole magnets. The corresponding lattice parameters in three cases are shown in Table 2.1.

The betatron tunes are less than 1.5 in all design and they satisfy the above 6 conditions. Especially, the twiss parameters are very smooth in Fig.2.2(c) compared with other two design, because the focusing element is distributed in the bending magnets. The betatron

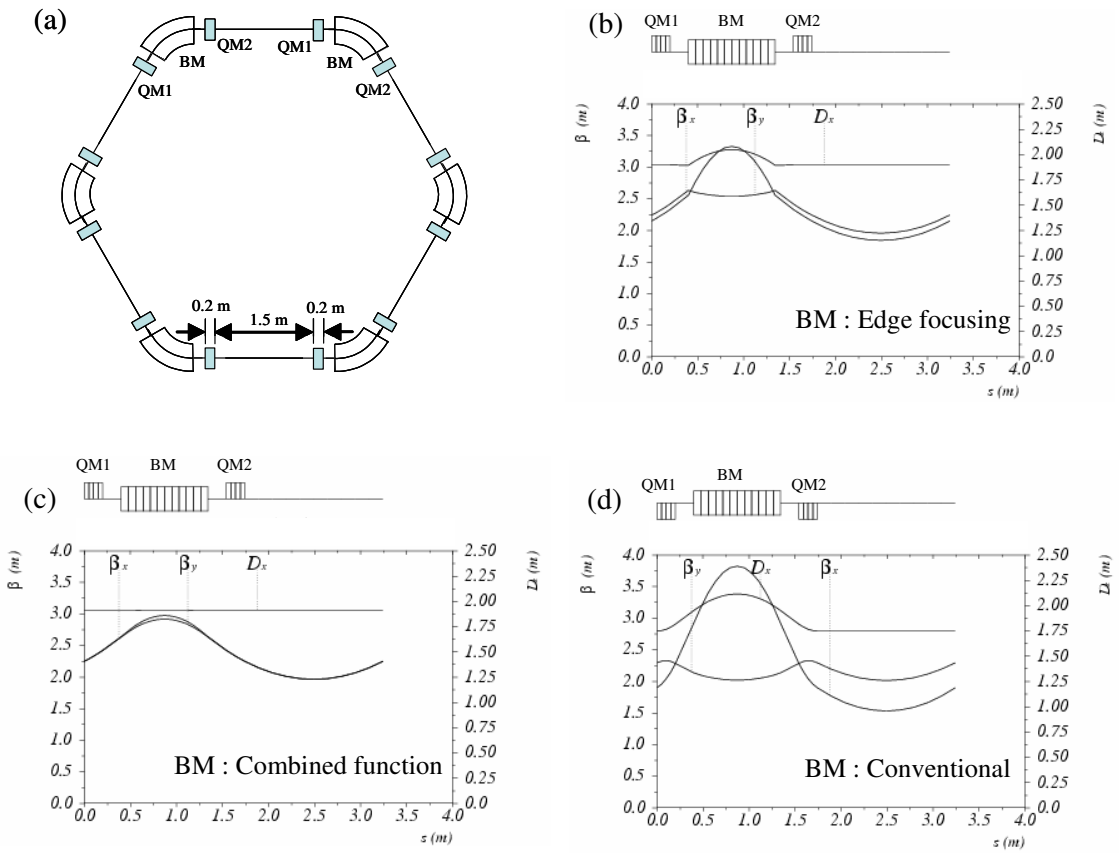

Figure 2.2: Design example of S-LSR (a). The twiss parameters in one period are shown with a bending magnet with an edge angle (b), a combined function bending magnet with n-value (c) and a bending magnet with normal entrance (d).

tune is also smaller than others. In Fig.2.2(b), the vertical β-function changes abruptly at the edge of the bending magnets, because the vertical focusing is concentrated at this position. It might be not appropriate for the crystalline beam generation. The betatron tune is larger than others in the case of the bending magnets with normal entrance.

From the comparison of the twiss parameters, the combined function magnet is attractive, but we must minimize the deviation of the magnetic field to keep the symmetry of the lattice. We will discuss this point in the next section. The combined function magnet is difficult to fabricate with very high accuracy, compared with the standard bending magnets, because the pole face is not flat and three-dimensional machining is necessary. Finally, the bending magnet with normal entrance has been adopted.

When the final design of the electron cooler was fixed, the length of the drift space was extended to 1.86 m. This space is necessary for the electron cooler to keep the effective cooling length of around 0.5 m [40]. From the design study of the quadrupole magnet, the

Table 2.1: Twiss parameters corresponding to the three cases in Fig.2.2(b), (c) and (d).

	Case (b)	Case (c)	Case (d)
Type of BM	Edge focus	Combined function	Normal entrance
Edge angle at BM	17.0 deg	0.0 deg	0.0 deg
Field gradient at BM	0.0	-0.66m^{-2}	0.0 m
Circumference	19.45 m	→	→
Average diameter	6.19 m	→	→
Length of drift space	1.50 m	→	→
Field gradient of QM1	0.0m^{-2}	→	-1.9m^{-2}
Field gradient of QM2	0.0m^{-2}	→	-1.9m^{-2}
Min. Betatron tune	(1.36, 1.36)	(1.33, 1.32)	(1.46, 1.45)
Chromaticity	(-0.30, -0.29)	(-3.9, 1.4)	(-0.11, 1.27)
Max. β-function	(3.3 m, 2.6 m)	(2.9 m, 3.0 m)	(3.8 m, 2.3 m)
Max. horizontal dispersion	2.0 m	1.9 m	2.1 m
Transition γ	1.24	1.27	1.23

length of the quadrupole magnets is determined to be 200 mm. The distance between the bending magnets and the quadrupole magnet is also 200 mm [41]. The iron plate is installed in this space in order to isolate the magnetic field and to avoid the magnetic field interference.

The geometry of one period is shown in Fig.2.3 in the final design. The drift space is 1.86 m and the curvature of the bending magnet is 1.05 m. The curvature of the bending magnet is extended in order to reduce the radial focusing and the betatron tune. The twiss parameters are shown in Fig.2.4 at the minimum betatron tunes of (1.45, 1.44). Table 2.2 shows the major parameters of S-LSR and Table 2.3 shows the lattice parameters at this operating point.

2.1.3 Operating Point

Figure 2.5 shows a betatron tune diagram. The red area is a stable region of the final lattice. The minimum betatron tune of (1.45, 1.44) is shown by the green circle. The operating point which satisfies the condition of Eq.(2.3) is limited from 1.45 to 1.50. The maintenance condition of Eq.(2.2) is satisfied in the wide area of the stable region. When the excitations of QM1 and QM2 are equal, the betatron tune moves along the blue curve. The lattice has mirror symmetry at the center of the drift space in this condition. In practice, when the betatron tune is close to 3, the β-function becomes large and it is not acceptable. The practical range of the betatron tunes is less than 2.5.

Besides the operating point of (1.45, 1.44), there are some operating points for experi-

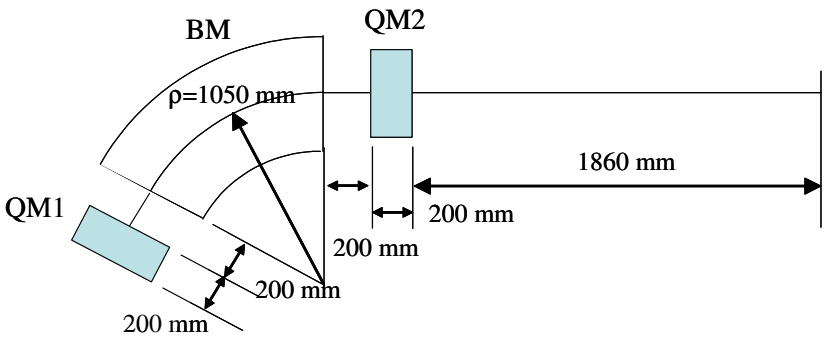

Figure 2.3: Structure of a single period. The ring has 6-fold symmetry.

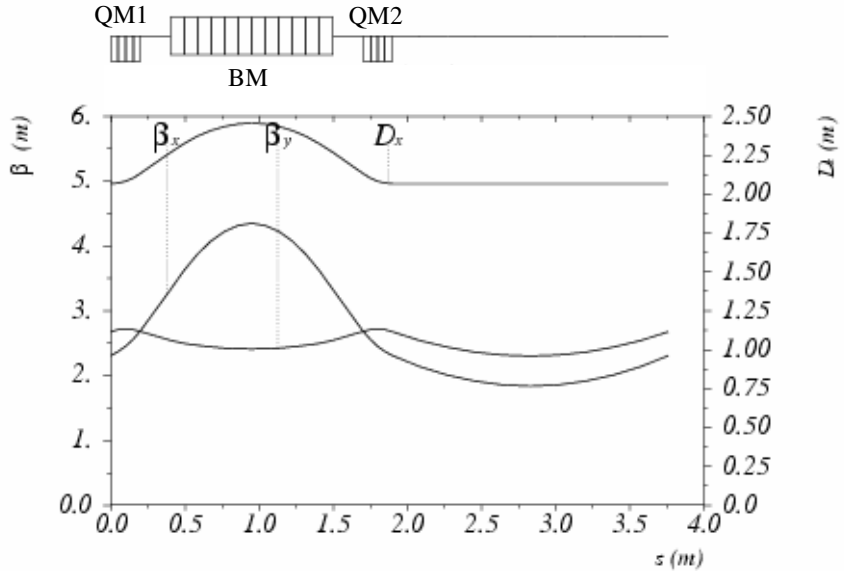

Figure 2.4: Twiss parameters in one period at the operation point of (1.45, 1.44).

Table 2.2: Major parameters of S-LSR and the magnets [42, 43].

Ring	
Circumference	22.557 m
Average diameter	7.18 m
Length of drift space	1.86 m
Number of superperiod	6
Stored beam	7 MeV proton and 40 keV Mg^+
Bending magnet	
Number of Magnets	6
Curvature radius	1.05 m
Gap height	70 mm
Pole width	371 mm
Bending angle	60°
Maximum field	0.95 T
Maximum current	650 A
Turn number of the coil	44 turns × 2 coils
Quadrupole magnet	
Number of Magnets	12 (2 families)
Length	200 mm
Bore radius	70 mm
Maximum field gradient	5 T/m
Maximum current	350 A
Turn number of the coil	28 turn

Table 2.3: Lattice parameters at the operation points of the minimum betatron tune.

Lattice parameters	
Field gradient of QM1	-1.59 m^{-2}
Field gradient of QM2	-1.59 m^{-2}
Betatron tune	(1.45, 1.44)
Chromaticity	(-0.10, 1.26)
Maximum β-function	(4.33 m, 2.74 m)
Maximum horizontal dispersion	2.42 m
Transition γ	1.23

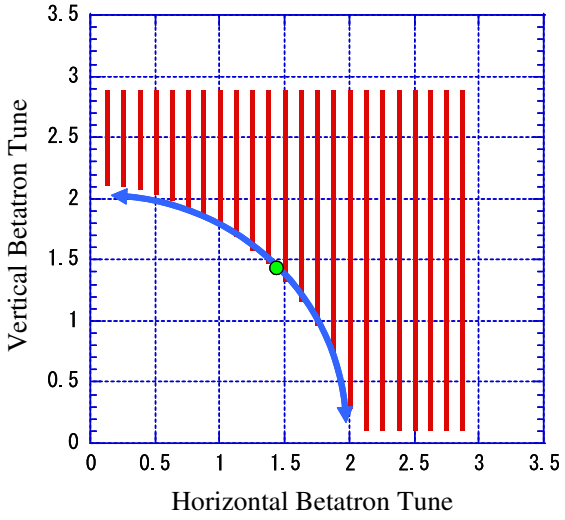

Figure 2.5: Calculated betatron tune diagrams by MAD8. The red area is a stable region. The green circle shows the minimum betatron tune of (1.45, 1.44). When the excitations of QM1 and QM2 are equal, the betatron tune moves along the blue curve.

ments. The electron cooling experiment does not need the small betatron tune and the small dispersion is preferable because the momentum spread of the injected beam is large. It is also better that the operating point is far away from the coupling resonance of $\nu_x = \nu_y$, because the cooling solenoid is a strong transverse coupling source. The standard operating point for the electron cooling is (1.64. 1.20). The ordering experiment by the electron cooling was also carried out at this operation point. Figure 2.6(a) shows the twiss parameters in one period at this operation point. The horizontal dispersion becomes smaller but the vertical β-function becomes larger.

The operating point of (2.07, 1.07) is used for a three-dimensional laser cooling. In the storage ring, the laser cooling works only in the longitudinal direction, because there is not enough interaction length in the transverse direction. In order to cool the ion beam in all directions, a coupled cooling method was proposed [44]. When the synchrotron tune is 0.07, the fractional parts of the three tunes coincide between each other and a strong coupling is induced in three degree of freedom. The betatron tune is larger than 1.5 but still satisfies the maintenance condition of the crystalline beam. Figure 2.6(b) shows the twiss parameters in one period. The lattice does not have mirror symmetry and it is FODO lattice to increase the horizontal tune.

Table 2.4 summarizes the lattice parameters at these operation points. The three operating points are shown in Fig.2.7 with resonance lines. The solid lines are the integer and half-integer resonances and the dotted lines show the third order resonances. The three operation points are enough far from the resonance lines except for the coupling resonance.

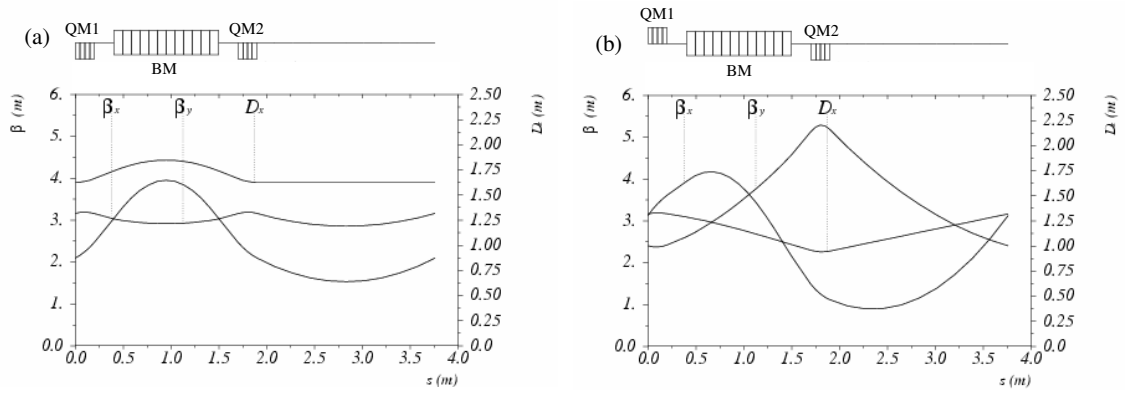

Figure 2.6: Twiss parameters in one period at the operation point of (1.64. 1.20) (a) for the electron cooling and (2.07, 1.07) (b) for the three-dimensional laser cooling.

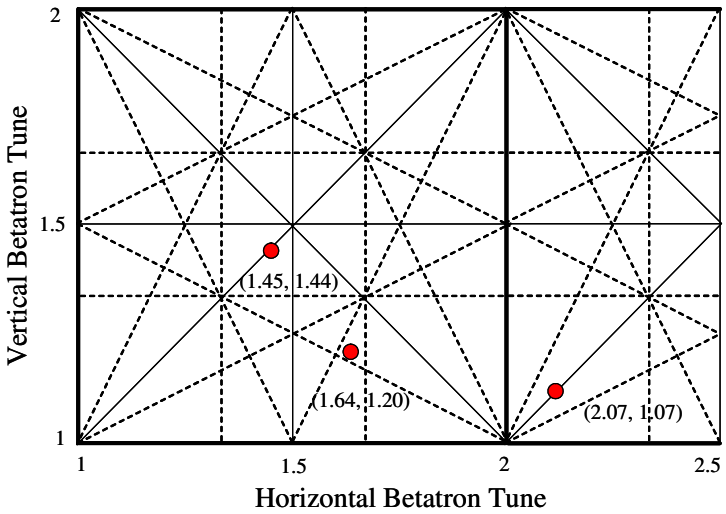

Figure 2.7: Three operating points and the resonance lines. The solid lines are the integer and half-integer resonance and the dotted lines are the third order resonance.

Table 2.4: Lattice parameters at the two operation points for the electron cooling and for the three-dimensional laser cooling.

	Electron Cooling	3-D Laser Cooling
Betatron tune	(1.64, 1.20)	(2.07, 1.07)
Field gradient of QM1	-1.16 m^{-2}	1.42 m^{-2}
Field gradient of QM2	-1.16 m^{-2}	-2.55 m^{-2}
Chromaticity	(-0.53, 0.74)	(-1.21 -0.18)
Maximum β-function	(3.96 m, 3.19 m)	(4.20 m, 5.32 m)
Maximum horizontal dispersion	1.41 m	1.32 m
Transition γ	1.41	1.76

2.2 Ring Magnets and Magnet Alignment

2.2.1 Ring Magnets

Figure 2.8 shows a bending magnet and a quadrupole magnet for S-LSR. The important issues of the magnets were,

- Small field deviation of the fundamental component among magnets,
- Small higher order (nonlinear) magnetic field components.

The fundamental component of the bending magnet is represented by B-L product, which is defined by an integral of the vertical magnetic field B_y along beam path (see Fig.1.1 about the coordinate),

$$BL \equiv \int B_y ds. \tag{2.4}$$

The fundamental component of the quadrupole magnet is represented by G-L product, which is defined by an integral of the field gradient along beam path. If the field deviation is large among the magnets, the 6-fold symmetry is broken and the linear resonance becomes $n/2$, not $nN_{sp}/2$. This linear resonance induces a strong beam heating. The acceptable rms deviation of the magnetic field is around 10^{-4} from the crystalline beam simulation [45].

The field deviation of the bending magnets also creates an orbit distortion of a particle. A closed orbit of a particle exists in a circular accelerator but in practice, it does not coincide with the ideal reference orbit due to the magnetic errors and the misalignment. The deviation of the closed orbit from the reference orbit is called closed orbit distortion (COD). The small COD is preferable for any accelerators, because the COD reduces the effective beam aperture. It is more crucial in the cooler ring, because the overlapping between the ion beam and the electron beam (for electron cooling) or a laser light (for laser cooling) is an essential condition for the efficient cooling. For example, the electron cooling force as a function of an angle

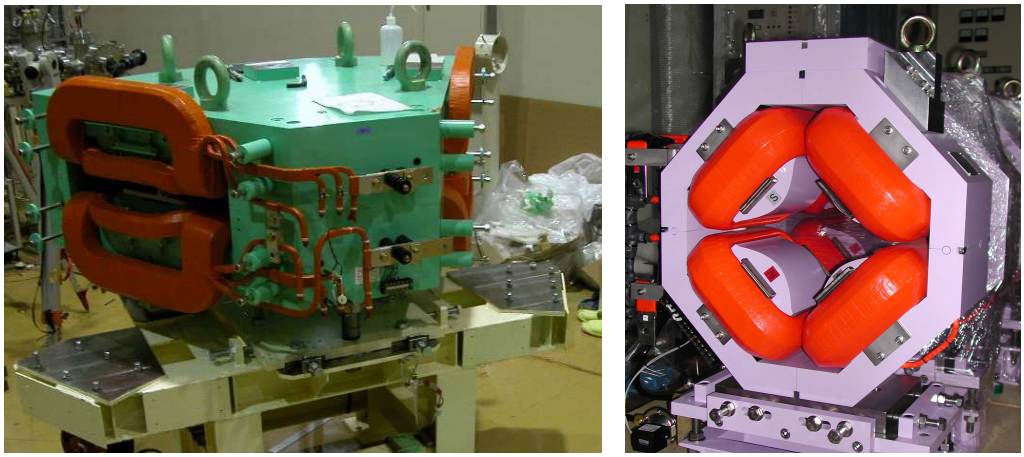

Figure 2.8: View of the bending magnet (left) and the quadrupole magnet (right).

between the ion and the electron beams is shown in Fig.3.13. The alignment accuracy of 0.1 mrad is necessary. The COD must be as small as possible and at least less than 1 mm. Otherwise, it exceeds the range of the fine adjustment by the electron beam or the laser light.

If one bending magnet has a deviation of B-L product $\delta(BL)$, the horizontal COD, $\mathrm{X_{cod}(s)}$ at the position s is given by (see Appendix B.2),

$$X_{cod}(s) = \frac{\sqrt{\beta_x(s)\beta_{BM}}}{2\sin\pi\nu_x}\frac{\delta(BL)}{B\rho}\cos\Phi(s), \tag{2.5}$$

where $\beta_x(s)$ and β_{BM} are the horizontal β-function at the position s and at the bending magnet, respectively. $B\rho$ is the magnetic rigidity and $\Phi(s)$ is the betatron phase. If the betatron phases at the bending magnets are random, the average horizontal COD is,

$$\langle X_{cod}(s)\rangle = \sqrt{\frac{N_{BM}}{2}}\frac{\sqrt{\beta_x\beta_{BM}}}{2\sin\pi\nu_x}\frac{\delta BL}{B\rho}, \tag{2.6}$$

where N_{BM} is the number of the bending magnets (= 6). If the rms deviation of B-L product is 10^{-4}, the calculated COD is 0.33 mm. It is close to the limit of the tolerance, because there are other sources of the COD. Therefore, the target value of the field deviation from the COD is around 10^{-4}.

In the discussion of coherent tune in the previous section, only the fundamental breathing mode was considered without any imperfection of the magnets. In practice, many higher modes exist in the particle motion. They are usually weak and it is possible to overcome by the beam cooling. However, if there are strong nonlinear components of the magnetic field, the corresponding higher order oscillation is resonated and disturbs the cooling. Therefore, the higher order magnetic field components must be as small as possible,

In order to satisfy the above requirements, the bending magnets and the quadrupole magnets were carefully designed by the three-dimensional magnetic field simulation code

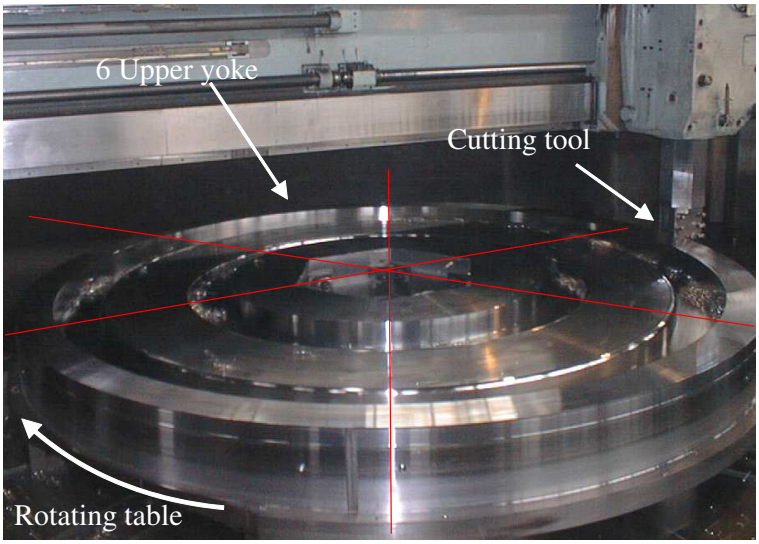

Figure 2.9: Machining of the six upper yokes of the bending magnets, which were fixed on the machine table. The deviation of the gap height is reduced less than ± 10 μm using a simultaneous cutting.

(TOSCA) [46] and fabricated from block iron with high precision. Then, the magnetic field of all magnets were measured by three Hall sensors (Group3 - MPT141) [47] and a shift coil. The details of the design and the results of the field measurement were reported in Refs.[30, 41, 42, 43]. Here, I note a fabrication method of the bending magnets. The error of B-L product is approximately given by,

$$\frac{\delta(BL)}{BL} \cong \frac{\delta B_y}{B_y} + \frac{\delta L}{L}, \tag{2.7}$$

$$\cong \frac{\delta g}{g} + \frac{\delta L}{L}, \tag{2.8}$$

where g is the gap height of the magnet and L is the length of the magnet. If the tolerance is 10^{-4}, the tolerable deviation of the length (1.1 m) is 0.11 mm, but the tolerable deviation of the gap height (70 mm) is only 7 μm. It is very difficult due to the variation of the iron temperature and the condition of the machine tool. We have adopted the simultaneous cutting method for the fabrication. Figure 2.9 shows the six upper yokes of the bending magnets, which were fixed on the machine table. The six yokes were connected each other and cut at the same time. The deviation of the gap height is less than 10 μm by this method.

The measured deviation of the B-L products among 6 bending magnets is shown in Fig. 2.10 [30]. They are within $\pm 3 \times 10^{-4}$ and the rms deviation is 1.5×10^{-4}. It is close to the target value. The further correction of the deviation is made by the control of the excitation current of the coils.

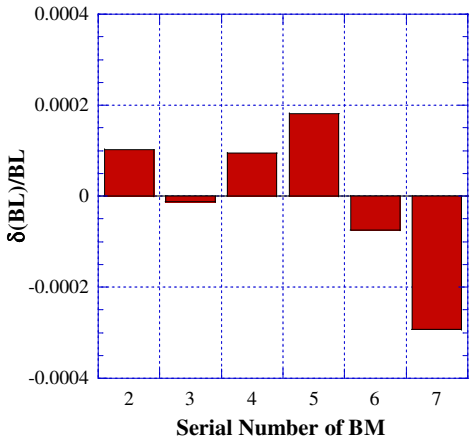

Figure 2.10: Measured deviation of the B-L products among 6 bending magnets. The excitation current is 275 A.

The deviation of the G-L products among 12 quadrupole magnets is shown in Fig. 2.11 [43]. The deviations in QM1 and QM2 families are within $\pm 5\times10^{-3}$ and $\pm 2\times10^{-3}$, respectively. The rms deviation are 3×10^{-3} and 1×10^{-3}, respectively. The correction of the G-L product is possible by a correction coil of the quadrupole magnet, although the further study is necessary, concerning the tolerance of the G-L product deviation at S-LSR.

2.2.2 Magnet Alignment

The precise alignment of the bending and the quadrupole magnets is also important because of the same reason; the symmetry and the COD. The effect of the alignment error on the lattice symmetry is not severe compared with the field deviation, because the length of the superperiod is 3.76 m, while the alignment error is around 0.1 mm. The ratio is less 10^{-4}. The COD is more severe for the alignment. Table 2.5 shows the evaluation results of the COD for each alignment error. They are calculated in the same way as that of the deviation of the B-L product. The COD by a single alignment error is calculated at first, then the averaging over the magnets is taken and it is multiplied by the factor of $\sqrt{N_{BM}}$ or $\sqrt{N_{QM}}$, where N_{QM} is the number of the quadrupole magnets (= 12). Table 2.5 suggests the alignment error within 0.1 mm is necessary to achieve the total COD less than 1 mm.

Figure 2.12 shows a view of the alignment of the magnets. The position of the magnets was measured by a laser tracker (LEICA, LTD800). It can measure three-dimensional coordinates of the tracker target (see lower right photo in Fig.2.12) using a laser light. There are accurate target holes on the magnets (three for BM, two for QM) to put the tracker target (see Fig.2.12). The exact positions of the magnets in 3D coordinate can be calculated from the position of the target holes. The precision of the measurement depends on the distance. For the alignment of S-LSR, the laser tracker was located near the center of the ring and the

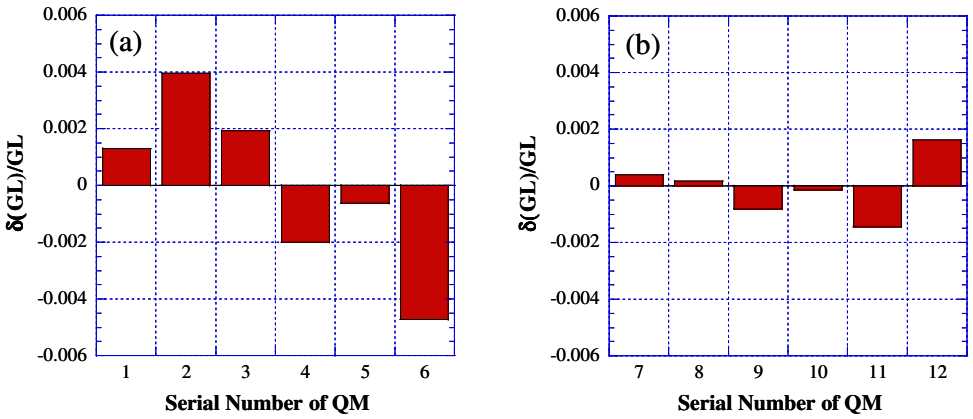

Figure 2.11: Measured deviation of the G-L products in the QM1 family (a) and in the QM2 family (b).

Table 2.5: Evaluation of the COD induced by the magnetic field errors and the alignment errors of the bending and quadrupole magnets. The mark of (H) means the horizontal COD and (V) is the vertical one.

Bending manget

	Error	COD (mm)
B-L Product	10^{-4}	0.33 (H)
Displacement in X-axis	0.1 mm	0.24 (H)
Displacement in Y-axis	0.1 mm	0.02 (H)
Displacement in Z-axis	0.1 mm	0.15 (V)
Rotation in X-axis	0.05 mrad	0.06 (H)
Rotation in Y-axis	0.1 mrad	0.15 (H)
Rotation in Z-axis	0.05 mrad	0.10 (H)

Quadrupole magnet

	Error	COD (mm)
G-L Product	10^{-3}	0.0
Displacement in X-axis	0.1 mm	0.11 (H)
Displacement in Y-axis	0.1 mm	0.11 (H)
Displacement in Z-axis	0.1 mm	0.0
Rotation in X-axis	0.05 mrad	0.01 (H)
Rotation in Y-axis	0.1 mrad	0.02 (H)
Rotation in Z-axis	0.05 mrad	0.0

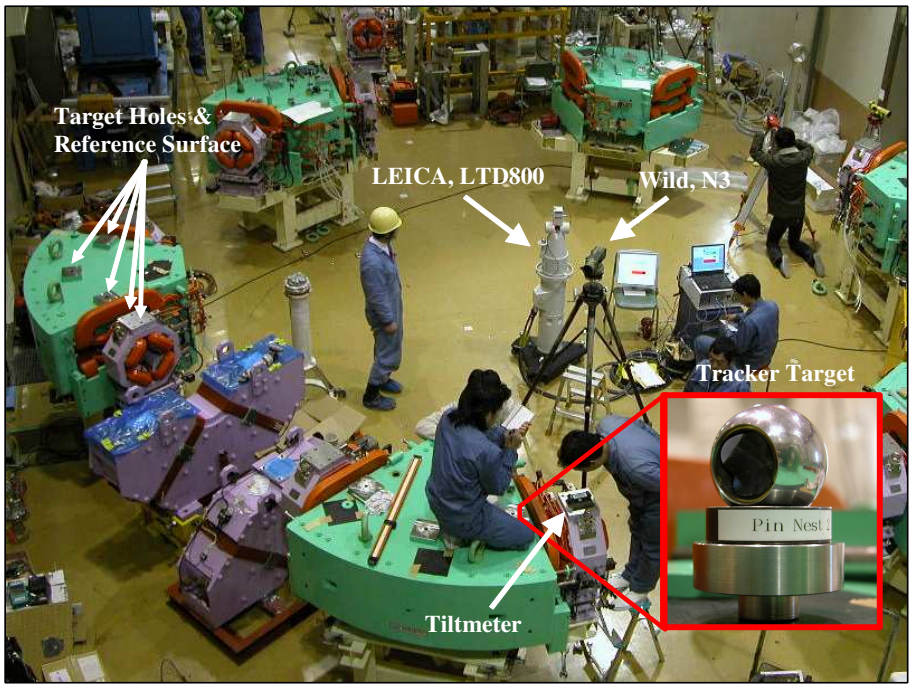

Figure 2.12: View of the alignment. The laser tracker and the precision level were located near the center of the ring.

average distance between the tracker and the target was around 3.5 m. The precision was 40 μm in this condition. This was confirmed by the measurement of the known distance between holes. The vertical level was measured by a precision level (Wild, N3). The reference surfaces on the magnets were measured by the level. The measurement accuracy was 50 μm. The tilt of the magnets was measured by a tiltmeter. The reference surface on the magnets was also used for the measurement of the tilt. The accuracy of the tiltmeter was 20 μm/m.

The alignment of the magnets except for one bending magnet and two quadrupole magnets was carried out in December, 2004. The alignment errors at all target holes were less than 0.1 mm and the errors of the tilt on all reference surfaces were less than 50 μm/m. One month later (January, 2005), the alignment of the remaining magnets was made and the position measurement was repeated by the laser tracker. Figure 2.13 shows a displacement of the target holes. The average displacement of the magnet position is 0.2 mm and the direction is toward the ring center. They are consistent with the expected thermal contraction of the concrete with the temperature reduction of 4.5 °C. The maximum deviation from the ideal contraction is 40 μm, which is comparable with the measurement error.

The final result of the alignment was shown in Fig.2.14. The histogram shows the alignment errors of the target holes on the magnets. There are 18 measured points for the bending magnets and 24 points for the quadrupole magnets. The position errors of the 60 % target

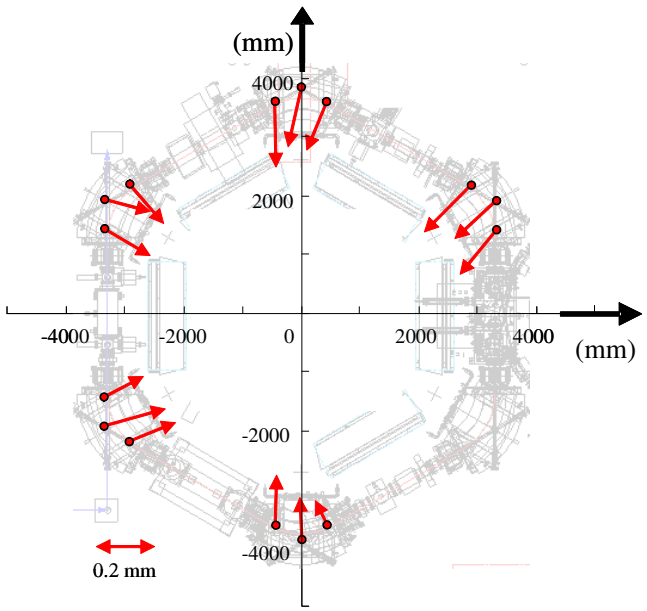

Figure 2.13: Displacement of the target holes between the measurements in December, 2004 and January, 2005. The length of the arrow is extended to 5000 times. They were measured by the laser tracker. The average temperature difference was 4.5 °C.

holes were within ±50 μm and those of all holes were within ±100 μm. The tilts of the all magnets were less than ±50 μm/m.

The calculated COD by MAD8 was shown in Fig.2.15 [48]. The measured alignment errors and the measured deviation of B-L product of the bending magnets were included in the calculation. The maximum CODs were 1.2 mm and 0.7 mm in the horizontal and the vertical directions, respectively. The rms CODs were 0.4 mm and 0.4 mm in the horizontal and vertical direction, respectively. The CODs at the electron cooling section (EC) and the laser cooling section (LC) were within ±0.6 mm. It satisfies the design requirement.

2.3 Beam Commissioning

We had finished the construction of S-LSR in the summer of 2005. The view and the layout of S-LSR are shown in Fig. 2.16 and Fig. 2.17. The first baking was carried out in September, 2005, after installing the various equipments into the vacuum chamber. The baking temperature was 200 °C and the top temperature period was 36 hours. Each vacuum chamber of the bending magnet has two NEG pumps and the electron cooler has three NEG pumps. The vacuum chambers at the straight sections are evacuated by the 8 sputter ion pumps and the 5 Titanium sublimation pumps. The average vacuum pressure was about 1×10^{-7} Pa in the beginning of October, 2005 and we started the beam commissioning using the 7 MeV proton from the linac. After the successful accumulation of the proton beam, the

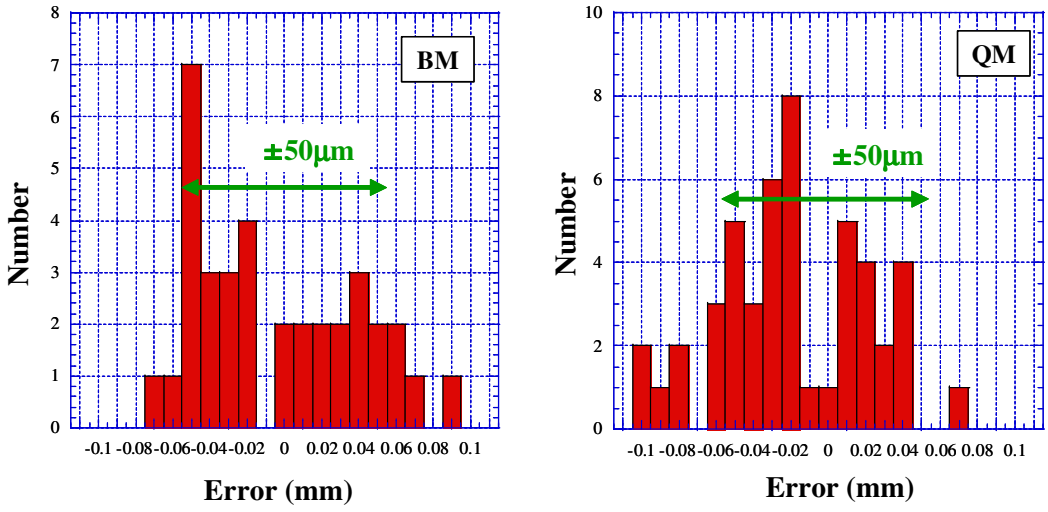

Figure 2.14: Alignment error of the position of the target holes on the bending magnets (3 holes × 6 magnets = 18 points) and the quadrupole magnets (2 holes × 12 magnets = 24 points) .

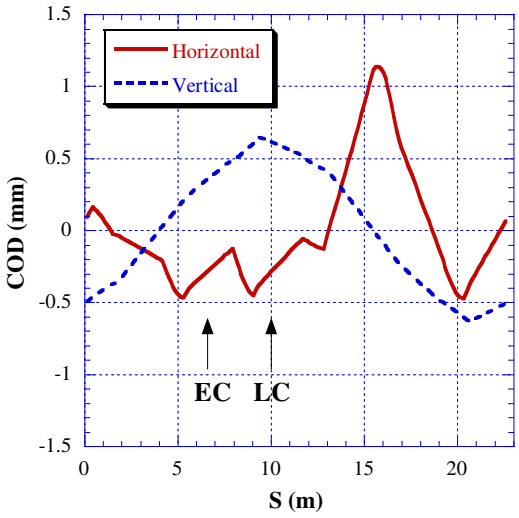

Figure 2.15: Calculated COD by MAD8 with the measured alignment error and deviation of the B-L products of the bending magnets. The marks of EC and LC show the positions of the electron cooling section and the laser cooling section.

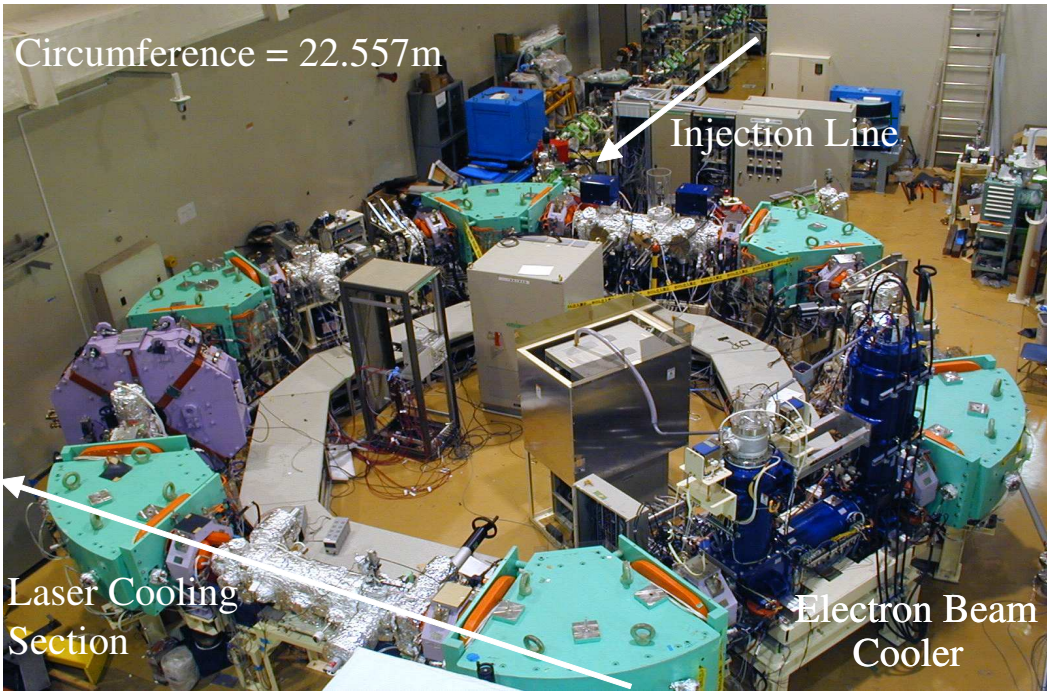

Figure 2.16: Photo of the ion storage ring, S-LSR.

commissioning of the electron cooling was started from November, 2005. The results of the electron cooling are described in the next chapter.

The lifetime of the proton beam was shown in Fig. 2.18. It was a stored beam current measured by DC current transformer (DC-CT) with and without the electron beam cooling. The average vacuum pressure was 2×10^{-8} Pa at this measurement. The lifetime without cooling was 1400 sec, which was determined by the multiple scattering with the residual gas. With the electron cooling, the multiple scattering was suppressed and the lifetime was extended to 23000 sec. After the second baking in June, 2006, the average pressure became around 1×10^{-8} Pa. The beam ordering experiments have been performed in this condition. Although, the vacuum pressure is improved, the lifetime decreases to 17000 sec. It is supposed that the lifetime is determined by the electron capture of the proton beam in the electron cooler,

$$H^+ + e^- \rightarrow H^0. \tag{2.9}$$

The alignment between the proton and electron beam is improved (see Section 3.3) and the cross section of the electron capture is increased. The lifetime of 17000 sec is still enough long for the experiments.

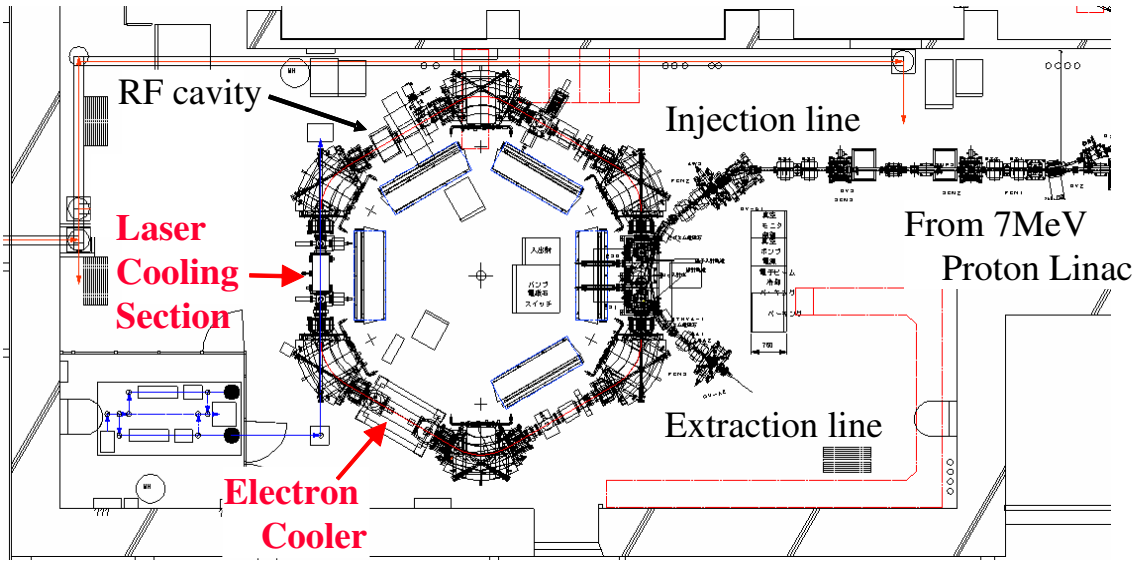

Figure 2.17: Layout of the ion storage ring, S-LSR.

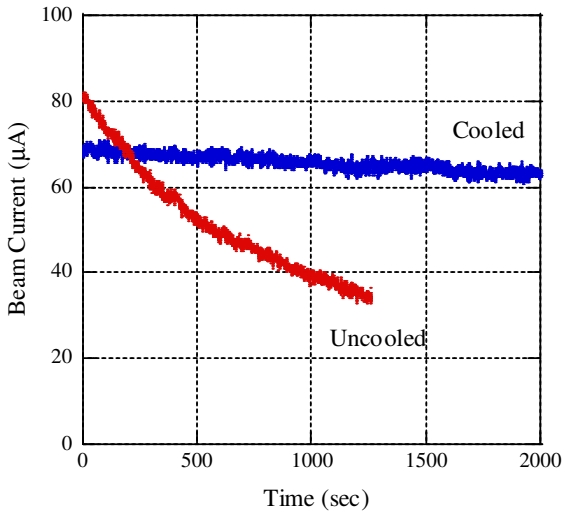

Figure 2.18: Lifetime of the 7 MeV proton beam measured by DC-CT. The average vacuum pressure was 2×10^{-8} Pa. The lifetime was 23000 sec and 1400 sec with and without the electron cooling, respectively.

2.3.1 COD and Twiss Parameter Measurement

The COD and the twiss parameters at S-LSR were measured using the 7 MeV proton beam in order to confirm the accuracy of the magnetic field and the alignment. The precise measurement is possible using the cooled proton beam, because it has a small emittance, a small momentum spread and a long lifetime. The momentum spread was typically 2×10^{-4} and the beam size was 1.2 mm at the ion current of 30 μA. The betatron tune was (1.644, 1.209).

The beam position was measured by electrostatic pickups. The pickup electrode for the position monitor is shown in Fig.2.19(a). It has four triangle plates with the length of 200 mm and the width of 100 mm. The vertical gap is 46 mm. The difference of the signal amplitude among four plates gives the beam position.

$$X = K_x \left(\log \frac{V_b}{V_d} - \log \frac{V_a}{V_c} \right), \tag{2.10}$$

$$Y = K_y \left(\log \frac{V_b}{V_d} + \log \frac{V_a}{V_c} \right), \tag{2.11}$$

where V_a, V_b, V_c and V_d are the pickup voltages from each electrode (see Fig.2.19(b)) K_x and K_y is a constant coefficient, which was measured by the electric calibration. The details of the monitor system are described in Ref.[49]. The measured COD is shown in Fig.2.20 along the longitudinal position. There are 8 position monitors in the ring. The maximum CODs are 2.5 mm and 1.2 mm in the horizontal and vertical directions, respectively. The rms values are 1.4 mm and 0.6 mm, respectively. The vertical COD is comparable with the calculation but the horizontal COD is 3.5 times larger than the calculation and the polarity of the maximum COD is opposite. It is considered that the difference mainly comes from a compensation error of a toroid field. Toroid coils in the electron cooler are placed at s = 7.5 m and produce a vertical magnetic field component. They are not compensated completely by steering magnets beside them. The COD at the electron cooling section is less than 1 mm in both directions and the beam-beam alignment is possible by the optimization of the electron beam orbit (see Section 3.3).

The β-function was measured from a betatron tune shift by a change of a field gradient of a quadruple magnet. The relation between the β-function and the betatron tune shift is given by (see Appendix B.2),

$$\delta\nu_{x,y} = \frac{\beta_{x,y}}{4\pi} \frac{\delta(GL)}{B\rho} \tag{2.12}$$

where $\delta\nu_{x,y}$ is the horizontal and vertical betatron tune shift, respectively. δ(GL) is the change of the G-L product of the quadrupole magnet and $B\rho$ is the magnetic rigidity. The field gradient was changed using the correction coil in the quadrupole magnet. The betatron tune was measured by the beam transfer function (BTF). Figure 2.21 shows the schematic diagram for the BTF measurement. When the frequency of the RF kicker field resonates the

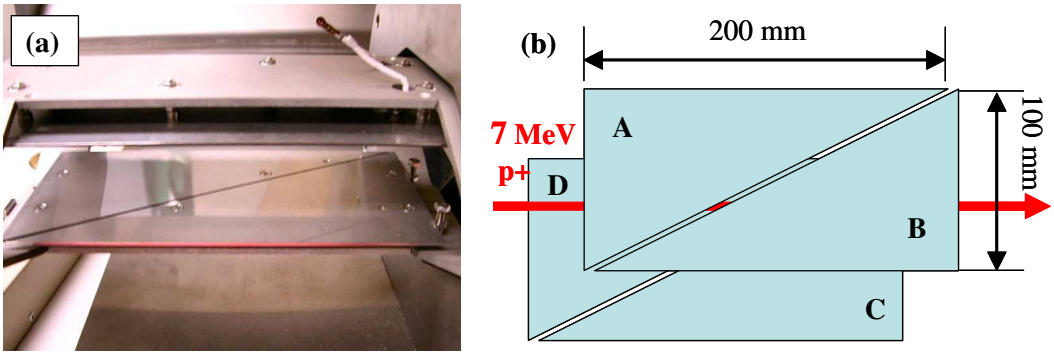

Figure 2.19: (a) View of the electrode for the beam position monitor. There are four triangle plates for the position measurement. (b) Schematic view of the electrode. Each electrode is named A, B, C and D (top view).

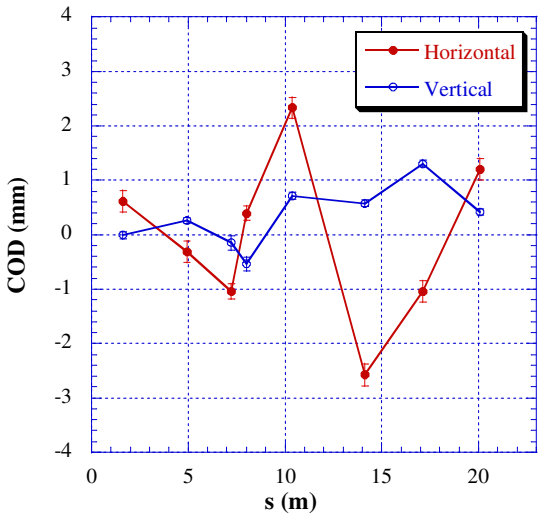

Figure 2.20: Measured closed orbit distortion in the ring. It was measured by the beam position monitors using the electrostatic pickups.

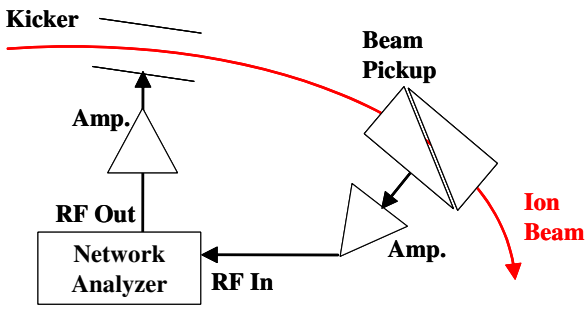

Figure 2.21: Schematic diagram of the beam transfer function (BTF) measurement.

transverse betatron motion of the particle, the amplitude of the transverse oscillation grows rapidly and can be detected by the pickup. One electrode of the position monitor is used as a pickup. The betatron tune can be calculated from the resonance frequency. The accuracy of the tune measurement depends on the width of the resonance. The measurement error of the betatron tune is typically 10^{-4}. Figure 2.22 shows the horizontal and vertical β-functions measured at the quadrupole magnets, together with the calculation. The circles are measured data and the lines are calculations by MAD8. Typically, when the field gradient is change by 5 %, the tune shift is around 0.003. The average β-function at the quadrupole magnets are 2.1 m and 3.0 m in the horizontal and vertical direction, respectively. The calculated ones are 2.2 m and 3.2 m, respectively. The variation of the measured β-function in the ring is within ± 5 % in the both directions. It is comparable with the measurement error.

The horizontal dispersion function η_x gives the relation between the momentum deviation of the particle δp_i and the deviation of the horizontal beam position δx_p,

$$\delta x_p = \eta_x \frac{\delta p_i}{p_i}, \tag{2.13}$$

where p_i is the ion momentum. Under the electron cooling, the ion velocity is equal to the electron velocity. If the electron energy E_e is shifted by δE_e, the momentum of ion is also shifted by $p_i(\delta E_e)/2E_e$ in the non-relativistic approximation. The dispersion can be measured from,

$$\delta x_p = \eta_x \frac{\delta E_e}{2E_e}. \tag{2.14}$$

The beam position shift was measured by the electrostatic position monitors and the electron energy was controlled by the cathode potential of the cooler, which was changed by 0.1 %, typically. The accuracy of the measurement depended on that of the position monitor. Figure 2.23 shows the measured horizontal dispersion. The average dispersion was 1.5 m at the position of the monitors, while the calculation by MAD8 was 1.6 m. The variation of the dispersion function in the ring was within ± 5 %. It was comparable with the measurement error.

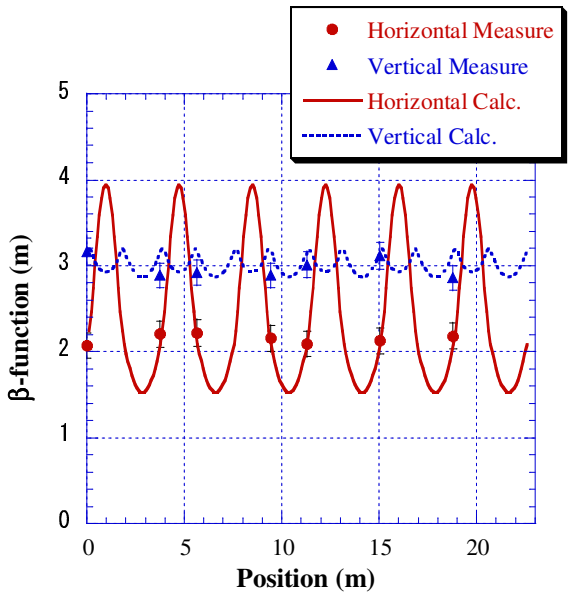

Figure 2.22: Measured and calculated β-function in the ring, when the betatron tune was (1.644, 1.209).

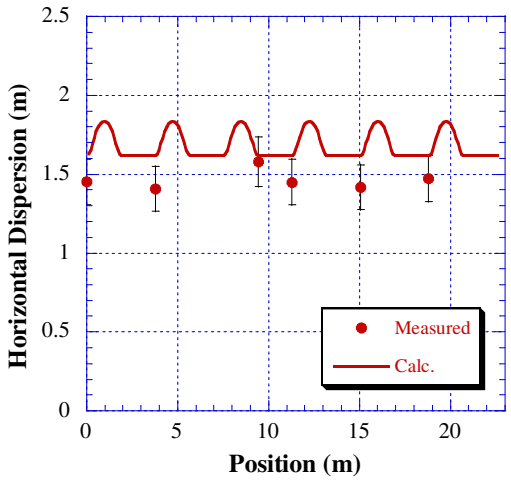

Figure 2.23: Measured and calculated horizontal dispersion function in the ring, when the betatron tune was (1.644, 1.209).

Chapter 3

Electron Cooling

An electron cooler is one of the most important devices for the one-dimensional ordering experiment. The electron cooler at S-LSR was designed by H. Fadil and produced by TOSHIBA Corporation. The details of the design were reported in Ref.[40, 50]. For the one-dimensional ordering, there are two important parameters. One is a limit of the cooling temperature; the other is a cooling force. The ordering or the crystallization of ions is a phase transition phenomenon. The cooling force must be enough large to overcome the heating and reduce the beam temperature down to the transition point. The limit of the cooling temperature must be lower than the transition temperature. If these two conditions are satisfied, the phase transition is realized.

The basics of the electron temperature and the electron cooling force are described in the first section. The electron cooler at S-LSR is briefly introduced in the second section and the measurement results and the optimization of the cooler are reported in the third section.

3.1 Basics of Electron Cooling

3.1.1 Temperature of Cooled Beam

The principle of the electron cooling is very simple. Ions and electrons overlap and move with the same velocity in the electron cooling device. If the electrons have no velocity spread, the energy of ions in the particle rest frame, transfers to the electrons due to the Coulomb collision. In practice, the electrons have a finite velocity spread (temperature) and the final goal of the electron cooling is equilibrium state where the ion and the electron temperature are equal,

$$k_B T_i = k_B T_e, \tag{3.1}$$

where T_i and T_e are the ion and the electron temperature, respectively. In other word, the lowest temperature of the cooled ions is limited by the electron temperature. Therefore, the

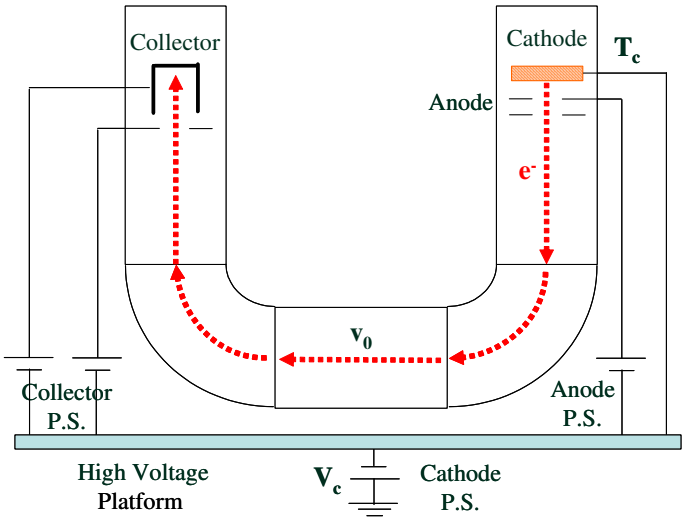

Figure 3.1: Schematic view of the electron cooler.

electron temperature is an important parameter. From Eq.(1.1),

$$\frac{1}{2}m_i\langle v_i^2\rangle = \frac{1}{2}m_e\langle v_e^2\rangle, \tag{3.2}$$

$$\sqrt{\langle v_i^2\rangle} = \sqrt{\langle v_e^2\rangle}\sqrt{\frac{m_e}{m_i}}, \tag{3.3}$$

where m_i and m_e are the ion and the electron mass, respectively. $\sqrt{\langle v_i^2\rangle}$ and $\sqrt{\langle v_e^2\rangle}$ are the rms velocity spread in the particle rest frame of the ions and the electrons, respectively. Because the mass of the electron is much smaller than that of the ion, the ion velocity spread becomes very small.

Figure 3.1 shows the schematic view of the electron cooler. The thermal electrons are emitted from the cathode with the temperature T_c. They are accelerated by the electrostatic voltage V_c and moves with the ions in the same velocity v_0. Finally, the electrons are decelerated in front of the collector and recovered. The electrons are guided by the solenoid field from the gun to the collector in the cooler.

The electron temperature at the cathode is,

$$k_BT_c = k_BT_{c\parallel} + k_BT_{c\perp}, \tag{3.4}$$

where $T_{c\parallel}$ and $T_{c\perp}$ are the longitudinal and transverse electron temperature at the cathode, respectively. The cathode temperature is 1150 K at the S-LSR cooler, which corresponds to 0.1 eV. In the laboratory frame, the transverse temperature is not changed after the acceleration. The transverse electron temperature in the particle rest frame is

$$k_BT_{e\perp} = \gamma_0^2\,(k_BT_{e\perp}^*) \cong k_BT_c, \tag{3.5}$$

where $k_B T^*_{e\perp}$ is the transverse temperature in the laboratory frame and γ is the Lorentz factor. Because the proton energy at S-LSR is 7 MeV, we use the non-relativistic approximation in the following discussion.

In the early days, the transverse electron temperature was equal to the cathode temperature. A method to decrease the transverse temperature was invented at CRYRING [51]. The electron makes a cyclotron motion along the solenoid field in the cooler. If the solenoid field is gradually decreased, the transverse electron motion becomes slow and the transverse temperature is decreased. This is called "adiabatic expansion".

The following quantum is an adiabatic invariant under the change of the magnetic field,

$$\frac{k_B T_{e\perp}}{B_{e\parallel}} \cong const. \tag{3.6}$$

The magnetic expansion factor α_{exp} is defined as,

$$\alpha_{exp} \equiv \frac{B_{\parallel gun}}{B_{\parallel cool}}, \tag{3.7}$$

where $B_{\parallel gun}$ and $B_{\parallel cool}$ are the magnetic field in the electron gun and the cooling solenoid, respectively. The transverse electron temperature is given under the adiabatic expansion,

$$k_B T_{e\perp} = \frac{k_B T_c}{\alpha_{exp}}. \tag{3.8}$$

At the same time, the electron beam radius r_e increases,

$$r_e \rightarrow r_e \times \sqrt{\alpha_{exp}}. \tag{3.9}$$

On the other hand, the longitudinal electron temperature is drastically reduced by the acceleration. The longitudinal velocity $v^*_\parallel$ in the laboratory frame is,

$$\frac{1}{2} m_i \left(v^*_\parallel\right)^2 = eV_c + k_B T_{c\parallel}. \tag{3.10}$$

Let us write, $v^*_\parallel = v_0 + \delta v_e$

$$\frac{1}{2} m_i \left(v_0^2 + 2 v_0 \delta v_e + \delta v^2\right) = \frac{1}{2} m_i v_0^2 + k_B T_{c\parallel}, \tag{3.11}$$

$$m_i v_0 \delta v_e \cong k_B T_{c\parallel}, \tag{3.12}$$

From Eq.(1.1), the longitudinal electron temperature $T_{e\parallel}$ is,

$$k_B T_{e\parallel} = m \delta v^2, \tag{3.13}$$

$$= \frac{\left(k_B T_{c\parallel}\right)^2}{m_e v_0^2}. \tag{3.14}$$

In practice, the higher longitudinal temperatures were reported in many coolers. Because the electron beam is like a gas and the distance between electrons are fluctuated, the electrons

get a potential energy from the local electric field [52]. This situation arises near the electron cathode before acceleration. If the acceleration is rapid and there is no relaxation, the potential energy E_p causes the temperature rise.

$$E_p \cong -\frac{e^2}{4\pi\epsilon_0\langle l_e\rangle} \cong -\frac{e^2 n_e^{1/3}}{4\pi\epsilon_0}, \tag{3.15}$$

where $\langle l_e\rangle$ is the mean electron distance. In many coolers, this term is larger than Eq.(3.14). From Eqs.(3.14, 3.15), the longitudinal electron temperature is,

$$k_B T_{e\parallel} \cong \frac{\left(k_B T_{c\parallel}\right)^2}{m_e v_0^2} + \frac{e^2 n_e^{1/3}}{4\pi\epsilon_0}. \tag{3.16}$$

3.1.2 Cooling Force

The electron cooling is the heat exchange between the ions and the electrons through the Coulomb interaction. The cooling force can be calculated from the Coulomb collision theory. The electron cooling without magnetic field is called "non-magnetized cooling". This is not realistic in the cooler but useful to understand the basic character of the electron cooling. The details are described in Appendix D. The cooling force is given by Eq.(D.14) [53],

$$F(\vec{v_i}) = \frac{4\pi Z^2 e^4 n_e}{(4\pi\epsilon_0)^2 m_e} L_c \int \frac{\vec{v_i} - \vec{v_e}}{|\vec{v_i} - \vec{v_e}|^3} f(v_e) d^3 v_e, \tag{3.17}$$

where L_c is the Coulomb logarithm, $f(v_e)$ is the distribution function of the electron with the velocity of v_e, and $\vec{v_i}$ and $\vec{v_e}$ are the ion and electron velocity in the particle rest frame. From this equation, the cooling force is proportional to the electron density n_e. This was confirmed in the electron cooler at S-LSR. Figure 3.2 shows a numerical example of the longitudinal cooling force at the electron density of 10^7 e^-/cm^3. The longitudinal and transverse electron temperatures are 0.1 meV and 10 meV, respectively. The shapes of the cooling force are much different between the longitudinal and transverse directions because of the different electron temperatures in the two directions.

The cooling force is proportional to the relative velocity, when $|v_i| \ll v_e$. This region is called "linear region" and the cooling force can be written as,

$$F(v_i) = -\alpha_c v_i, \tag{3.18}$$

$$\alpha_c = -\frac{dF(v_i = 0)}{dv_i}, \tag{3.19}$$

$$\tag{3.20}$$

where α_c is a constant. Only this region is interesting for the ordering experiment, because the ion temperature is very low. In the linear region, the cooling rate Γ_c can be calculated from α_c,

$$F(v_i) = -\frac{\alpha_c}{m_i \gamma} p_i. \tag{3.21}$$

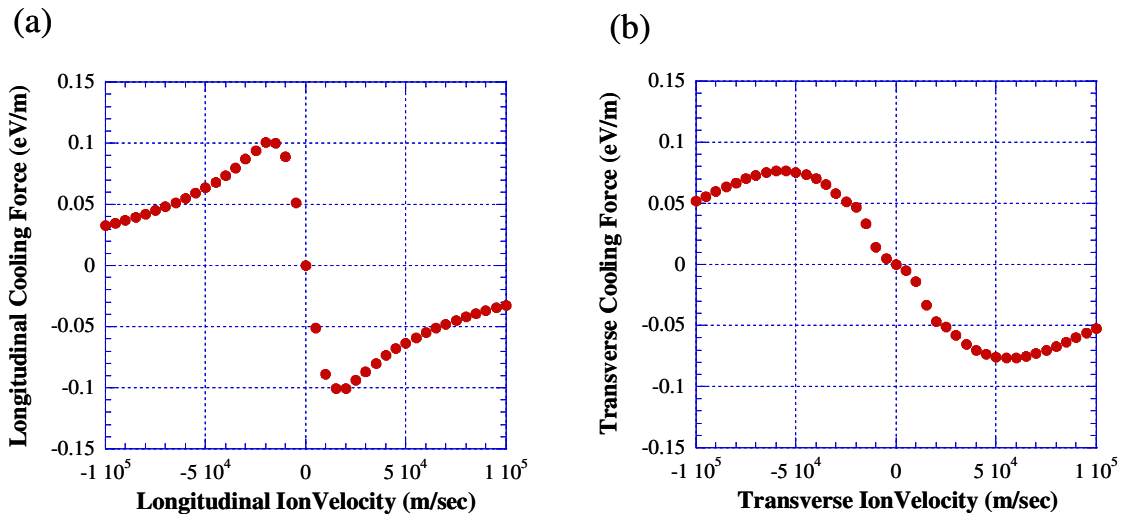

Figure 3.2: Numerical calculation of the longitudinal (a) and transverse (b) non-magnetized cooling force. The electron density is 10^7 e^-/cm^3. The longitudinal and transverse electron temperatures are 0.1 meV and 10 meV, respectively.

The momentum change is,

$$\frac{dp_i}{dt} = -\eta_c \frac{\alpha_c}{m_i \gamma} p_i, \tag{3.22}$$

where η_c is the ratio of the effective length of the electron cooler to the circumference of the ring. Therefore, the cooling rate is,

$$\Gamma_c = \frac{\eta_c \alpha_c}{m_i \gamma}. \tag{3.23}$$

When the strong magnetic field exists in the cooler, the electron motion is changed. The electrons rotate around the magnetic field line with a cyclotron frequency f_c and a Larmor radius r_L. If the impact parameter b is larger than the Larmor radius and the collision time b/v is larger than $1/f_c$, the electron motion in the transverse direction is frozen for the ions. This effect improves the imbalance of the electron temperature in the longitudinal and the transverse direction and increases the cooling force. This is called "magnetized cooling". The magnetized cooling forces in the linear region are given by the formulas [53],

$$F_{\parallel}(v_i) = -\frac{2\pi Z^2 e^4 n_e}{(4\pi\epsilon_0)^2 m_e} v_{i\parallel} \left(\frac{2L_1}{\delta v_{e\perp}^2 \delta v_{e\parallel}} + \frac{L_2}{\delta v_{e\parallel}^3} \right), \tag{3.24}$$

$$F_{\perp}(v_i) = -\frac{2\pi Z^2 e^4 n_e}{(4\pi\epsilon_0)^2 m_e} v_{i\perp} \left(\frac{2L_1}{\delta v_{e\perp}^3} + \frac{L_2}{\delta v_{e\parallel}^3} \right), \tag{3.25}$$

where $\delta v_{e\parallel}$ and $\delta v_{e\perp}$ are the longitudinal and the transverse rms velocity spread of the electrons. L_1 and L_2 are constants. The first terms in both equations are smaller than the

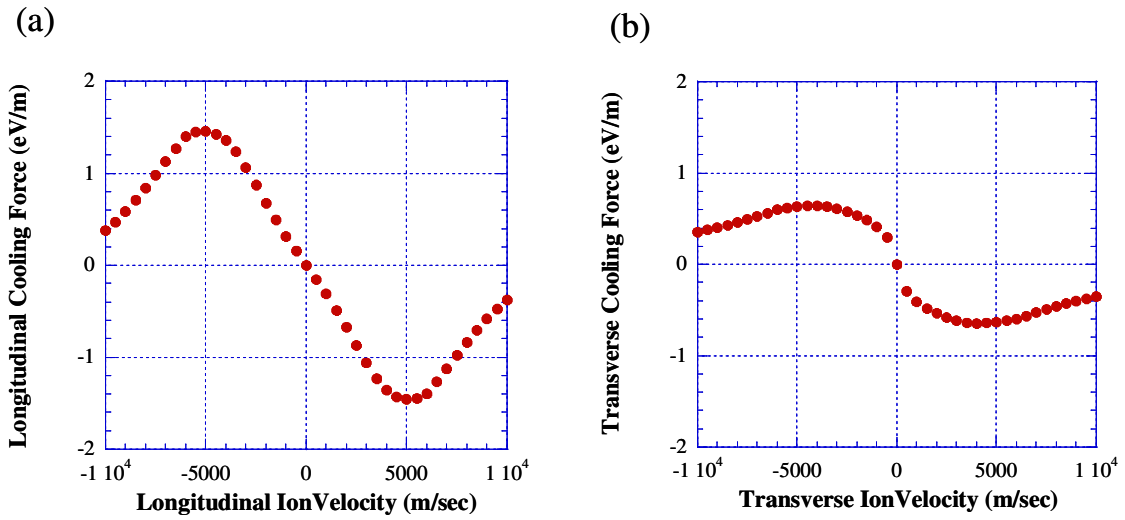

Figure 3.3: Numerical calculation of the longitudinal (a) and transverse (b) magnetized cooling force. They are calculated by the program code BETACOOL [54]. The electron density is 10^7 e^-/cm^3. The longitudinal and transverse electron temperatures are 0.1 meV and 10 meV, respectively.

second terms because of $\delta v_{e\parallel} < \delta v_{e\perp}$. Therefore, the longitudinal and the transverse cooling forces have similar values. However, the calculation of the magnetized electron cooling uses approximations and the calculated cooling forces are higher than the measurements in the existing electron coolers.

Figure 3.3 shows a numerical example of the magnetized cooling force at the electron density of 10^7 e^-/cm^3. The longitudinal and transverse electron temperatures are 0.1 meV and 10 meV, respectively. The cooling force becomes larger by one order of magnitude than the non-magnetized cooling force. The longitudinal cooling force has a maximum at the ion velocity close to the rms electron velocity spread. In Fig.3.3, the maximum cooling force is at 5000 m/sec, while the rms electron velocity spread is 4200 m/sec (0.1 meV). From this relation, the electron temperature can be estimated.

3.2 Electron Cooler at S-LSR

Figure 3.4 shows the electron cooler at S-LSR. The electron cooler consists of an electron gun section (up-right), two toroid sections (90 degree bend), a cooling solenoid (center) and an electron collector (up-left). There is a solenoid field along the passage of the electron beam. Table 3.1 shows the major parameters of the electron cooler. The maximum electron energy is 5 keV and the operating energy is 3.8 keV for 7 MeV protons. The expansion factor is 3 in the standard operation mode. The magnetic field around the electron gun is

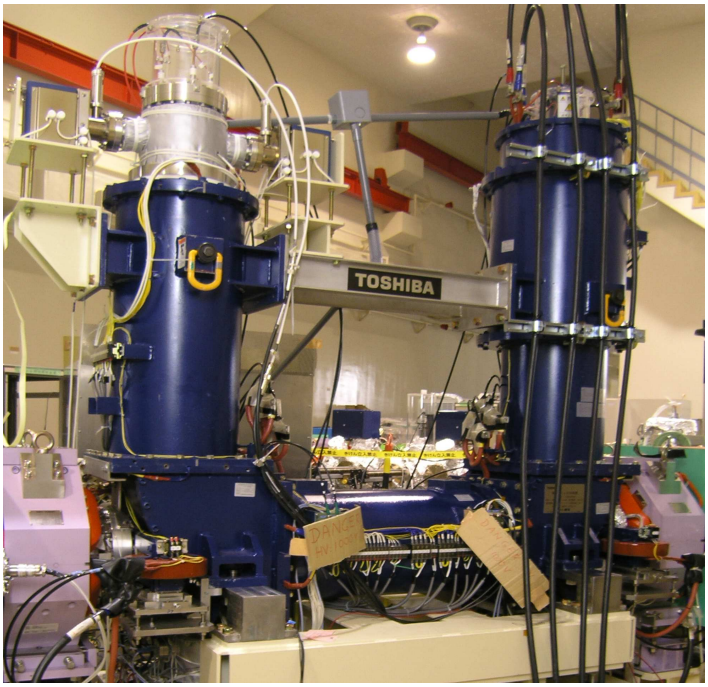

Figure 3.4: Photo of the electron cooler at S-LSR.

1.5 kGauss and it is 500 Gauss in the other sections. The cathode diameter is 30 mm and the electron beam diameter at the cooling solenoid is 50 mm with the expansion factor of 3. The length of the cooling solenoid is 800 mm, while the effective length of the cooling is 440 mm, which was determined from the magnetic field measurement.

The design issue of the electron cooler is a compactness to install in the short drift space (1.86 m) at S-LSR. On the other hand, the long cooling length is necessary for the fast cooling. In order to satisfy the contradictory requirements, various ideas are implemented in the cooler. For example, electrostatic deflectors are installed in the toroid coils. It was proposed at Indiana University and put into practical use by the BINP group to reduce a secondary electron loss [55]. The beam loss is a serious problem in this cooler, because the aperture of the electron beam is small due to the space limitation. The benefit of the electrostatic deflector is demonstrated in the cooling experiment at S-LSR [56].

The design of the cooling solenoid coil is also important task. The magnetic field has been calculated by the three-dimensional code, TOSCA [40]. Figure 3.6 is the calculation model of TOSCA. The most important parameter is the transverse magnetic field in the cooling solenoid. The electron moves around the magnetic field line and if there is a non-homogeneous transverse field, the direction of the electron beam is changed and the electron has a large transverse velocity to the ion beam. As the results, the ion beam is no longer cooled in the transverse direction. The transverse field determines the effective cooling length.

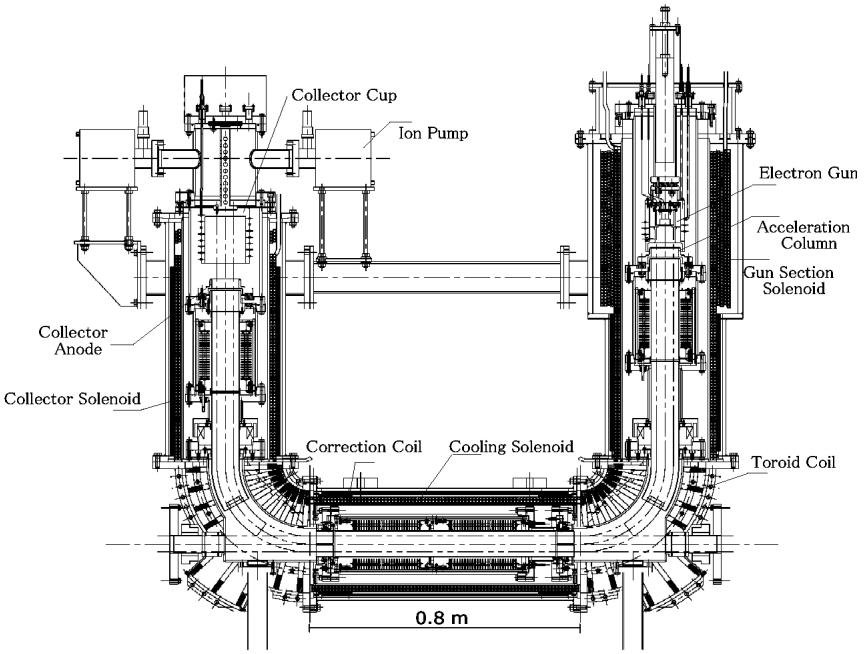

Figure 3.5: Cross section view of the electron cooler.

Table 3.1: Major parameters of the electron cooler at S-LSR.

Maximum Electron Energy	5 keV
Electron Energy for 7 MeV $p+$	3.8 keV
Electron Beam Current	0.025-0.3 A
Gun Perveance	2.2 μP
Cathode Diameter	30 mm
Expansion Factor	1-3
Maximum Solenoid Field at Gun Section	1.5 kGauss
Maximum Solenoid Field at Cooler Section	0.5 kGauss
Toroid Angle	90 degree
Toroid Radius	0.25 m
Cooling Solenoid Length	0.8 m
Effective Cooling Length	0.44 m

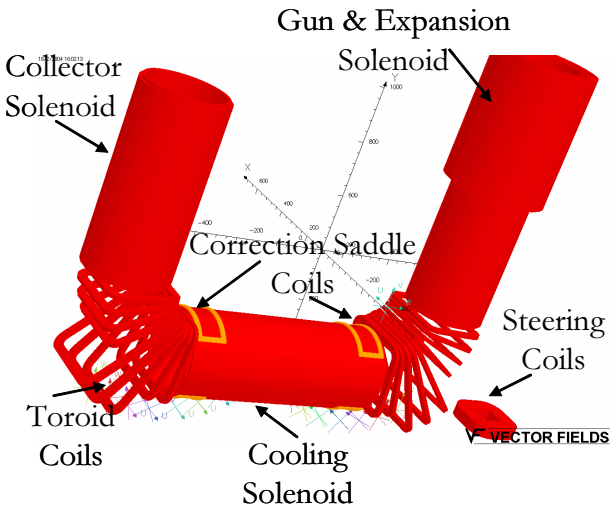

Figure 3.6: Calculation model of 3-dimensional electro-magnetic field code, TOSCA.

In the field simulation by TOSCA, the effective cooling length became 500 mm, where the field flatness $B_\perp/B_\parallel$ was within $\pm 2\times 10^{-4}$. However, the field flatness of $\pm 2\times 10^{-4}$ corresponds to the transverse field of ± 0.1 Gauss. It is easily changed by the production error of the coil and the leakage of the magnetic field. Therefore, we measured the magnetic field of the cooling solenoid without vacuum chambers at National Institute for Radiological Sciences (NIRS). The three Hall sensors (Group3 - MPT141) were used for the measurement. As the result, the flat region was very small and the leakage field of the horizontal steering magnets created the vertical magnetic field of 0.5 Gauss, which is shown in Fig.3.7(a).

In order to compensate the field, four fine correction coils and iron rings were installed (see Fig.3.7(b)). The iron rings were attached to shunt the vertical magnetic field at the outside of the coil. The fine correction coils created the vertical fields in the different positions, which are shown in Figure 3.8. With the linear combination of the four coils, the magnetic field in the cooling solenoid was optimized. Figure 3.7(a) shows the magnetic field after the correction. The effective length became 440 mm with the field flatness of $\pm 2\times 10^{-4}$.

After the installation of the vacuum chamber, the magnetic field of the cooling solenoid was measured again. It was found that the magnetic field distribution was changed from the previous measurement. The reason might be a reassembling of the toroid coils and an effect of the vacuum chamber. The result of the field re-optimization by the correction coils is shown in Fig.3.9. The effective cooling length is recovered to be 440 mm. The field flatness in the horizontal and vertical directions are $\pm 5\times 10^{-4}$ and $\pm 2\times 10^{-4}$, respectively. The rms deviations of the field flatness are 3×10^{-4} and 1×10^{-4}, respectively. The horizontal field cannot be optimized, because there is no horizontal correction coils in the cooling solenoid.

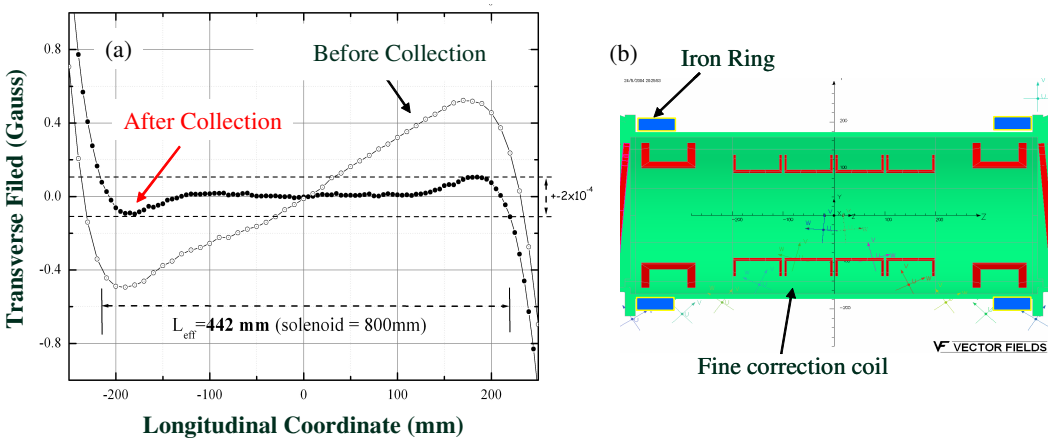

Figure 3.7: Measured magnetic field in the cooling solenoid before and after the correction (a). The four correction coils and the iron rings for the field correction (b).

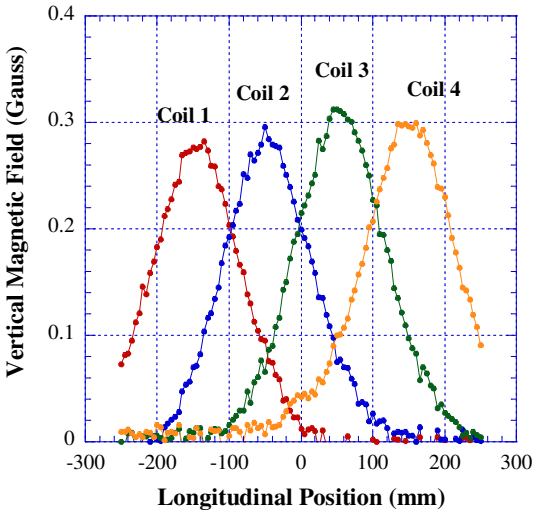

Figure 3.8: Vertical magnetic field created by four fine correction coils. The excitation current is 1 A.

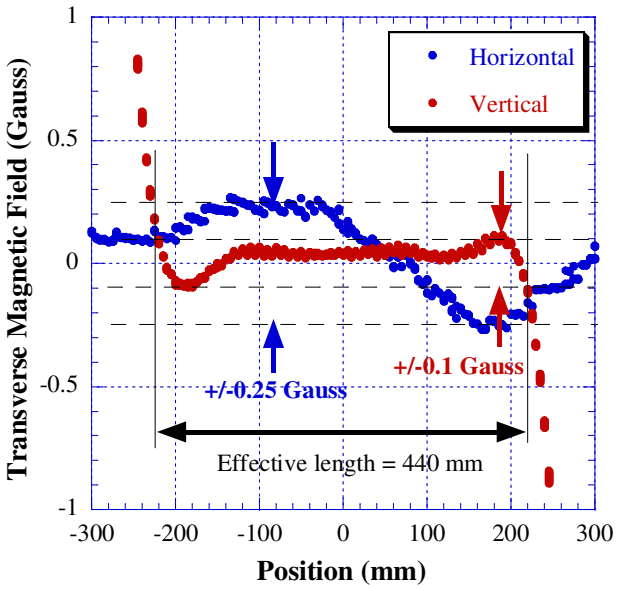

Figure 3.9: Measured horizontal and vertical magnetic field in the cooling solenoid with vacuum chamber. The vertical field was optimized again by the fine correction coils.

3.3 Optimization of Electron Cooling

In the commissioning of the electron cooling for 7 MeV protons, the cooling was succeeded in the first day of the beam test. Figure 3.10 shows the momentum spread and the horizontal profile of the cooled protons. The proton beam current was 50 μA, which corresponded to 2×10^8 particles in the ring. The electron current was 60 mA. The momentum spread was measured by a Schottky noise monitor and the horizontal beam profile was measured by an ionization residual gas monitor using a micro channel plate. The monitors are explained in the next Chapter. The initial momentum spread of 4×10^{-3} was reduced to 2×10^{-4} after the cooling. The initial beam size of 26 mm was reduced to 1.2 mm.

However, after the first beam cooling, it took almost a half year to optimize the cooling and to improve the electron cooling device for the ordering experiment. The important points were an alignment of the ion and electron beam and the stability of the electron energy.

3.3.1 Beam-Beam Alignment

As described in the previous section, the overlapping of the ion and the electron beam is important for the electron cooling. Especially, the error of the angle between two beams must be comparable with the magnetic field error of 10^{-4} (=0.1 mrad). The positions of the ions and the electrons were measured at the entrance and exit of the cooling solenoid by the electrostatic position monitors. The electron beam position was adjusted by the Helmholtz

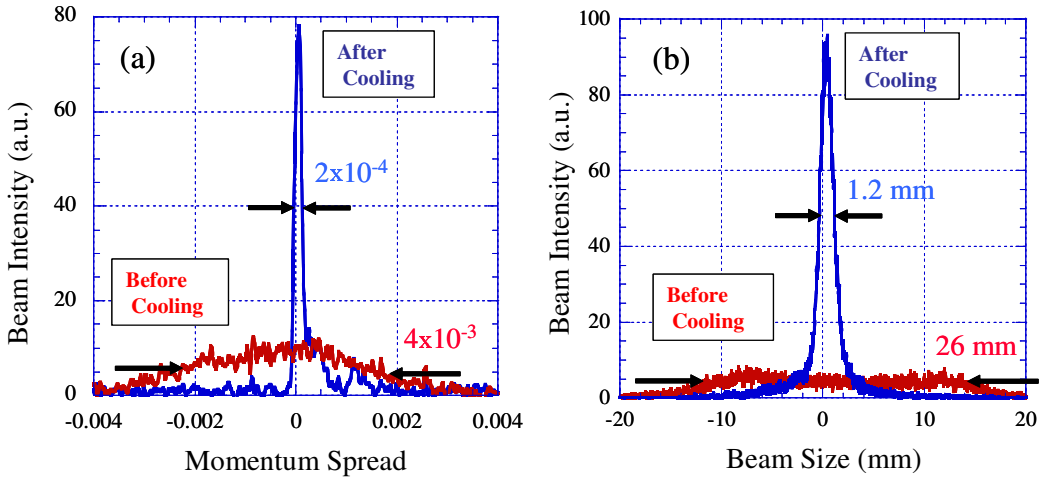

Figure 3.10: Momentum spread (a) and a horizontal profile (b) of 7MeV protons before and after the electron cooling. They are measured by a Schottky noise monitor and an ionization residual gas monitor using a micro channel plate, respectively. The proton beam current was 50 μA and the electron current was 60 mA.

coils. However, the accuracy of the position monitor was only about 0.3 mm and it was not enough. In addition, the vertical electron position at the monitors was not exactly same as that in the cooling area, because of the variation of the magnetic field.

In the commissioning period of the electron cooling, the horizontal beam profile was used for the beam-beam alignment. If the misalignment angle was large, the transverse cooling force was decreased and the beam size was increased (see Eq.(3.25)). Figure 3.11 shows the relation between the measured beam radius and the misalignment angle. The beam radius was measured by the ionization residual gas monitor. The misalignment angle was created by Helmholtz coils in the cooling solenoid. The beam size increased with the large misalignment angle but it was constant within the misalignment angle of $\pm$0.5 mrad. The minimum beam radius of 0.25 mm was the limit of the monitor resolution and not a real beam radius. The alignment with the accuracy of 0.1 mrad was difficult due to this resolution limit.

Finally, the longitudinal cooling force is used for the optimization of the beam-beam alignment, because it has a correlation to the transverse electron velocity (see Eq.(3.24)). An induction accelerator is used for the cooling force measurement. This scheme was developed at TSR [57]. The schematic diagram is shown in Fig.3.12(a). The induction accelerator is an iron core with a primary winding. The power supply provides the time-varying current. The ion beam corresponds to a secondary winding and gets an induction voltage through the time-varying magnetic flux. It can apply a constant acceleration or deceleration voltage on the ion beam for a certain period. The energy gain of ions per a revolution is ZeU_{ind}, where U_{ind} is the constant induction voltage. When the induction voltage is applied on the cooled

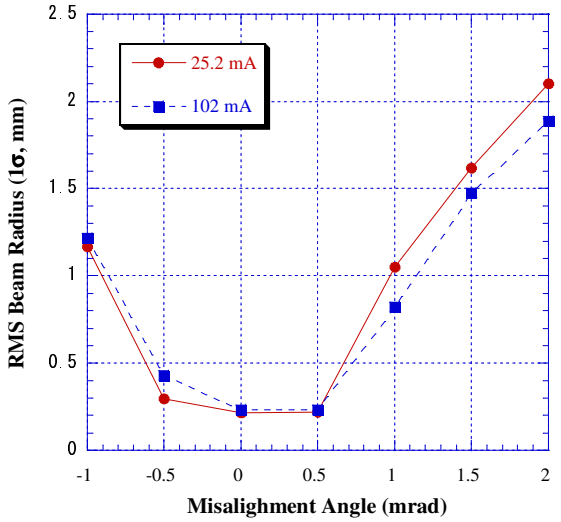

Figure 3.11: Relation between the measured rms beam radius and the misalignment angle. The electron current of the cooler was 25.2 mA and 102 mA. The beam radius was measured by the ionization monitor. The particle number is 10^7.

ions, the velocity of ions is shifted (see Fig.3.12(b)). In the equilibrium state,

$$ZeU_{ind} = F_{\parallel}(v_{\parallel})L_{EC}, \tag{3.26}$$

where $F_{\parallel}(v_{\parallel})$ is the longitudinal cooling force and L_{EC} is the effective length of the cooling. The cooling force is given by,

$$F_{\parallel}(v_{\parallel}) = \frac{ZeU_{ind}}{L_{EC}}. \tag{3.27}$$

Figure 3.13 shows the maximum longitudinal cooling force as a function of the horizontal misalignment angle. The electron current was 25.2 mA. The artificial misalignment angle was created by Helmholtz coils in the cooling solenoid. The cooling force is very sensitive to the alignment angle and it is possible to make the alignment with the accuracy of 0.1 mrad.

3.3.2 Cooling Force

After the optimization of the beam-beam alignment, the longitudinal cooling force was measured precisely. Figure 3.14(a) shows the cooling force at the electron current of 56 mA ($=4.9\times10^6\ e^-/cm^3$). The cooling force was measured from the negative peak to the positive peak. It has a maximum of 0.12 eV/m at the relative velocity of $\pm$3500 m/sec. The linear coefficient α_c is $4.8\times10^{-5}eVs/m^2$ in the linear region. Figure 3.14(b) shows the electron current dependence of the maximum cooling force. The cooling force is proportional to the electron current except for 215 mA. It is supposed that the space charge of the electron beam induces the heating above 215 mA.

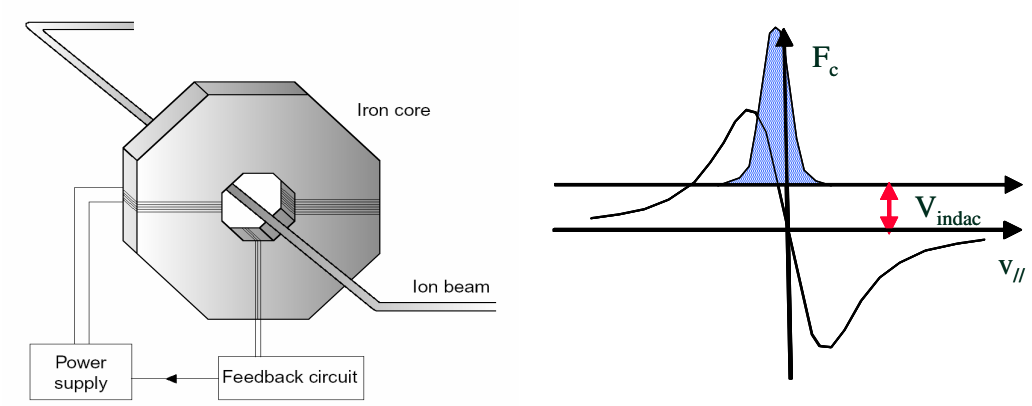

Figure 3.12: (a) Schematic diagram of the induction accelerator. (b) Principle of the longitudinal cooling force measurement by the induction accelerator.

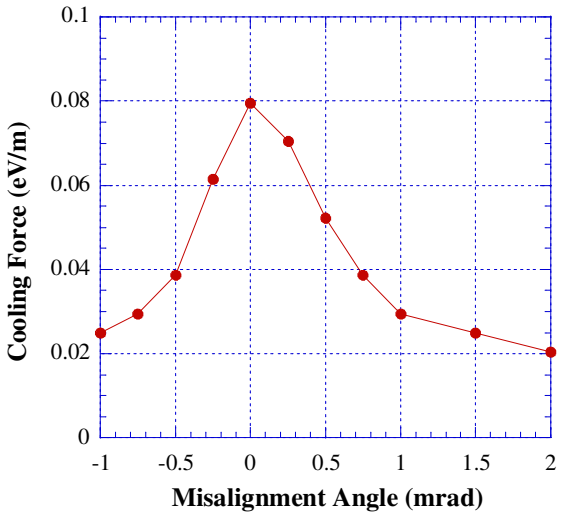

Figure 3.13: Maximum longitudinal cooling force as a function of the misalignment angle. The electron current of the cooler was 25.2 mA. They were measured by the induction accelerator. The particle number is 10^7.

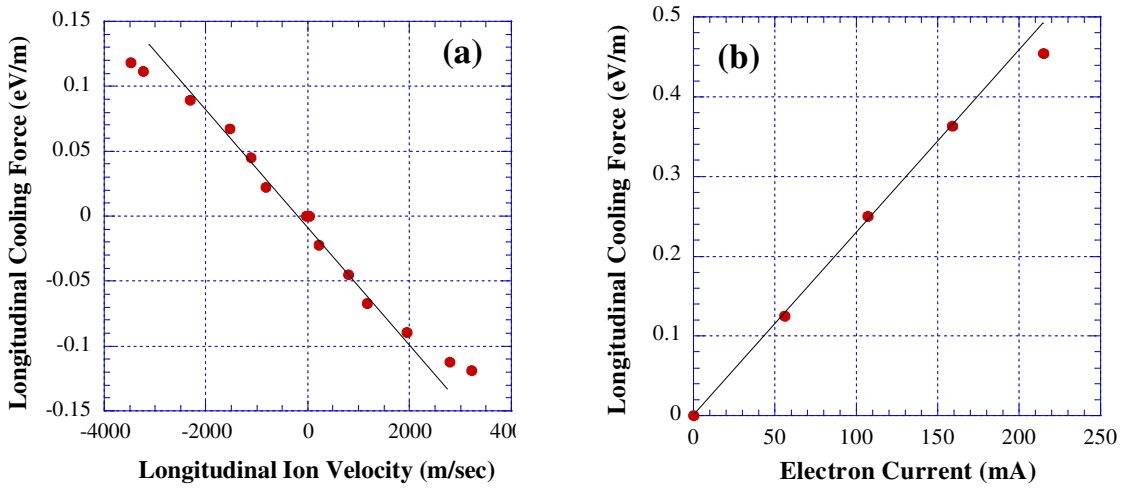

Figure 3.14: (a) Cooling force with the electron current of 56 mA (4.9×10^6 e^-/cm^3) as a function of the relative velocity. (b) The electron current dependence of the maximum cooling force.

3.3.3 Electron Temperature

The transverse electron temperature $T_{e\perp}$ is given by Eq.(3.8). When the cathode temperature is 1150 K and the expansion factor is 3 at S-LSR, the calculated transverse electron temperature is 34 meV. The longitudinal electron temperature $T_{e\|}$ is given by Eq.(3.16). When the electron energy is 3.8 keV and the electron current is 56 mA (=4.9×10^6 e^-/cm^3), the first term in Eq.(3.16) is 1.3 μeV, the second is 24 μeV and the total calculated value is 25 μeV. The calculated electron temperature is 20 μeV at the electron current of 25 mA (2.2×10^6 e^-/cm^3).

Figure 3.15 shows the calculated longitudinal magnetized cooling force by the BETACOOL code at the electron current of 56 mA. The longitudinal and transverse electron temperatures are 25 μeV and 34 meV, respectively. Although the longitudinal cooling force is 10 times larger than the measured one, it has a maximum value at the ion velocity of 3500 m/sec. It agrees well with the measurement. It suggests that the longitudinal electron temperature is close to the expected one.

3.3.4 Stability of Electron Energy

The electron energy is determined by the voltage of the cathode power supply (see Fig.3.1). The ripple of the power supply induces the rise of the electron temperature. Figure 3.16(a) shows the measured ripple voltage of the cathode power supply. The voltage divider with the ratio of 1/500 was used for the measurement. The ripple voltage is $\pm$0.4 V (p-p) and the frequency is 60 Hz. The rms ripple voltage is 0.3 V. The cathode power supply itself does

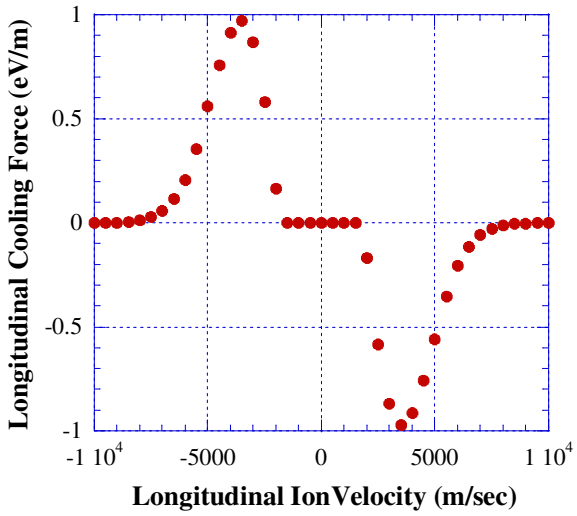

Figure 3.15: Calculation of the longitudinal magnetized cooling force. The electron current is 56 mA (4.9×10^6 e^-/cm^3) the longitudinal and transverse electron temperatures are 25 μeV and 34 meV, respectively.

not have such a ripple voltage but the ripple mixed through the isolation transformer. If there is the ripple voltage δV on the cathode, it causes the effective temperature rise. From Eq.(3.16), the electron temperature is,

$$k_B T_{e\|} \cong \frac{\left(k_B T_{c\|}\right)^2 + (e\delta V)^2}{m_e v_0^2} + \frac{e^2 n_e^{1/3}}{4\pi\epsilon_0}. \tag{3.28}$$

The electron temperature increased from 25 μeV to 60 μeV with the rms ripple voltage of 0.3 V.

In order to remove the ripple, an RC filter was inserted, which is shown schematically in

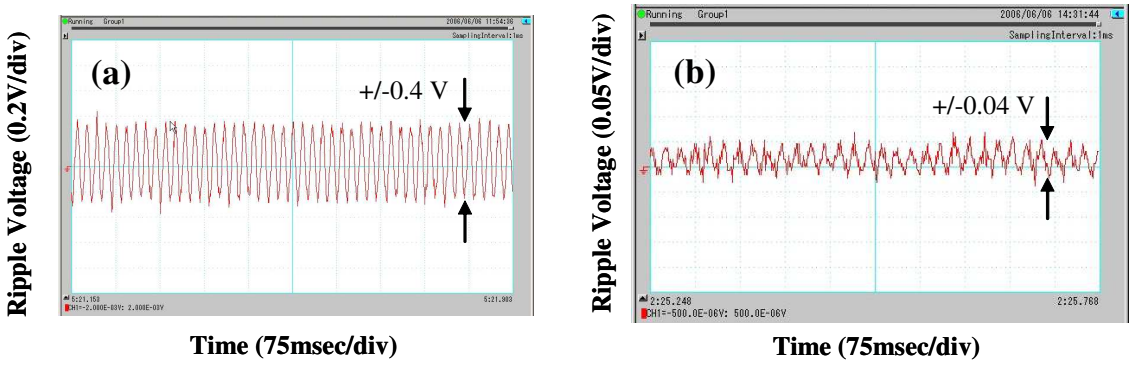

Figure 3.16: Voltage ripple on the cathode without (a) and with RC filter (b).

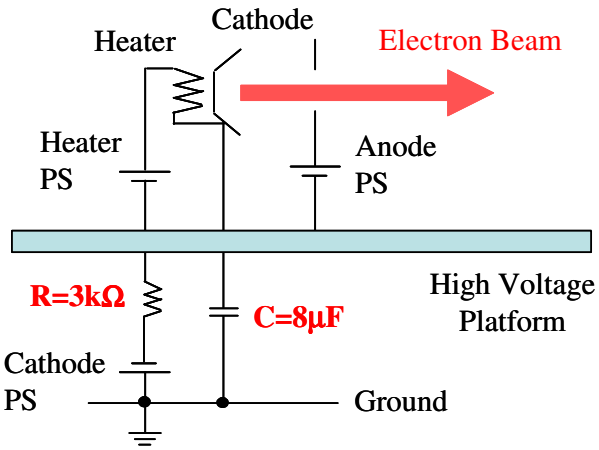

Figure 3.17: Schematic diagram of the RF filter. The resistance of 3 kΩ and the capacitance of 8 μF are inserted.

Fig.3.17. The capacitance C is 8 μF. It has an impedance of 330 Ω for 60 Hz component, which was lower than other impedance. The resistance R was 3 kΩ and the RC time constant is 6.6 Hz. It is higher than that of the feedback circuit of the cathode power supply to avoid the anomalous oscillation. The ripple was reduced ten times by the filter (see Fig.3.16(b)). The ripple voltage is less than ±0.04 V (p-p). The rms ripple voltage is less than 0.03 V, which is smaller than the thermal energy (0.1 eV) on the cathode.

If the cathode power supply has a drift of the voltage ΔV in a measurement period, the measured momentum spread of ions becomes,

$$\left(\frac{\delta p}{p}\right)_m = \sqrt{\left(\frac{\delta p}{p}\right)^2 + \left(\frac{\Delta V}{2V_c}\right)^2}. \tag{3.29}$$

In the ordering experiment, the minimum momentum spread was around 1×10^{-6} and the typical averaging time of the momentum spread was a few minutes. The rms drift voltage must be lower than 8 mV for a few minutes. In the early days of the experiment, the control system of the cathode power supply had a large drift (around 400 mV/hour). It was improved and the present drift is 80 mV/hour. It is almost tolerable for a few minutes measurement.

Chapter 4

Beam Monitors for Proton Ordering

In the one-dimensional ordering experiment, a momentum spread and an emittance of the cooled beam were measured as a function of a particle number. Since the typical particle number at the ordering transition was expected to be some thousands from the cases of the heavy ions, special beam diagnostics were necessary for such very low intensity, especially for singly charged protons. It was one of the reasons why the ordering of protons was not observed yet.

Four kinds of beam monitors were used for the measurements of three beam parameters.

- Particle number : Ionization residual gas monitor and a bunch signal monitor.
- Momentum spread : Schottky noise spectrum.
- Beam emittance : Beam scraper and an ionization residual gas monitor.

The particle number was measured by the two methods. One is an ionization residual gas monitor and the other is a bunch signal monitor. The data of the ionization residual gas monitor is used for the analysis. The bunch signal monitor is used for the check of the data.

The momentum spread was measured from the frequency spread of the Schottky noise spectrum. The beam emittance ϵ is calculated from the measured beam size σ_b,

$$\epsilon = \frac{\sigma_b^2}{\beta}. \tag{4.1}$$

where β is the β-function at the monitors. The value of the β-function is calculated by MAD8. The difference of the β-function between the calculation and the measurement is within 10 % at the positions of the quadrupole magnets (see Fig.2.22). The beam size was mainly measured by a beam scraper. When the beam size was larger than 0.1 mm, it was also measured by an ionization residual gas monitor.

The total setup of the experiment is shown in Fig.4.1. The device controllers (Nichizou Multi-Control Unit (MCU)) are attached to all power supplies for the magnets [58]. The

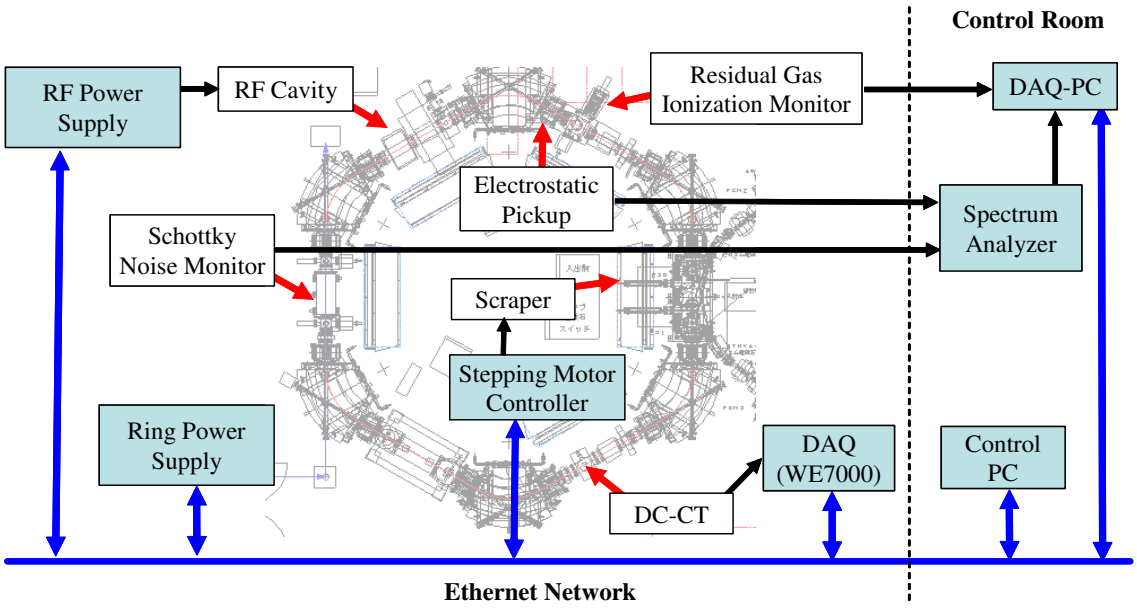

Figure 4.1: Total setup of the ordering experiment.

stepping motor for the scraper is controlled by another device controller (Tsuji-densi PM3C-05A-NT). They are connected each other though the Ethernet network and controlled by the server computer. Two client computers were used for the experiments. One PC communicated with the server computer and changed the parameters of the power supply and the position of the beam scraper. The other PC collected the data from the beam monitors, such as a Schottky noise monitor, bunch signal monitor, a DC-CT and an ionization residual gas monitor.

The detail for each monitor is described in the following sections.

4.1 Particle Number Measurement

4.1.1 Ionization Residual Gas Monitor

An ionization residual gas monitor using a micro channel plate (MCP) was developed at TSR [59]. A similar type of the monitor has been developed at S-LSR [49]. Figure 4.2(a) shows the vacuum chamber for the ionization monitor and Fig.4.2(b) shows the assembly of the electrode and the MCP. Figure 4.3 shows the scheme of the ionization residual gas monitor. The residual gas ionized by the circulating protons drifts to an upper MCP along an electrostatic field. The electric field is 1 kV/cm around the beam. The side electrode is designed to form the uniform field. The voltage of -1.75 kV is applied on the top plate and +3.25 kV on the bottom plate. The MCP is a Chevron type with the size of 15 mm $\times$ 100 mm. It has two layers and the gain of 10^7 with a voltage of 2 kV. It can detect a single ion.

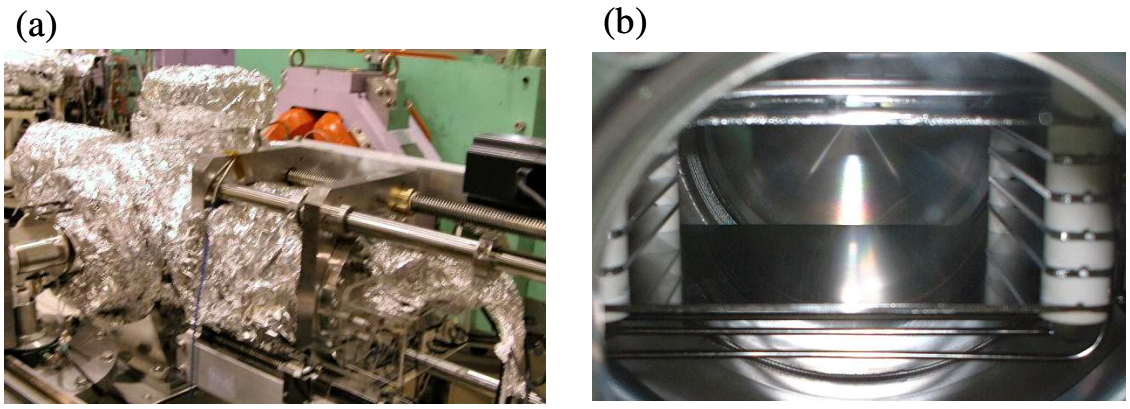

Figure 4.2: Photo of the ionization residual gas monitor. The left is the vacuum chamber of the monitor and the right is the assembly of the electrode and the MCP.

The block diagram of the signal processing for the ionization monitor is shown in Fig.4.4. The timing difference between two signals from the RAE is measured by a time-to-amplitude converter (TAC). This circuit is originally developed for the beam profile measurement, which is discussed later. It is also convenient for the counting of the ion number, because a background event generated at the different point on the MCP or an electric noise in the signal lines can be eliminated with the narrow timing window, which is typically 50 nsec.

The counting rate N_c can be estimated from the energy loss per unit length -dE/dz of the beam. The Bethe-Bloch formula is,

$$-\frac{dE}{dz} = 4\pi r_e^2 m_e c^2 \frac{Z N_0 z^2}{\beta^2} \left(\ln \left(\frac{2 m_e \beta^2 c^2}{(1-\beta^2) I} \right) - \beta^2 \right), \tag{4.2}$$

where r_e is the classical radius of electron, βc is the velocity of the beam, N_0 is the particle number of the residual gas in a unit volume, I is the mean ionization energy, z and Z are the charge numbers of the beam and the residual gas, respectively. The residual gas of more than 95 % is hydrogen from the mass analysis [26]. The mean ionization energy I is 15.4 eV and the average energy to create one ion-electron pair W is 37 eV for hydrogen [60]. The calculated energy loss is 6×10^{-8} eV/m at the average vacuum pressure of 1×10^{-8} Pa. The counting rate is given by,

$$N_c(sec^{-1}) = \frac{-dE/dz}{W} L_{mcp} \eta f_0 N_p, \tag{4.3}$$

where L_{mcp} is the effective length of the MCP in the longitudinal direction, η is the detection efficiency, f_0 is the revolution frequency and N_p is the number of the particle in the ring. The counting rate is proportional to the particle number and the coefficient is,

$$N_c = 4 \times 10^{-5}\ N_p \ \ (count/sec), \tag{4.4}$$

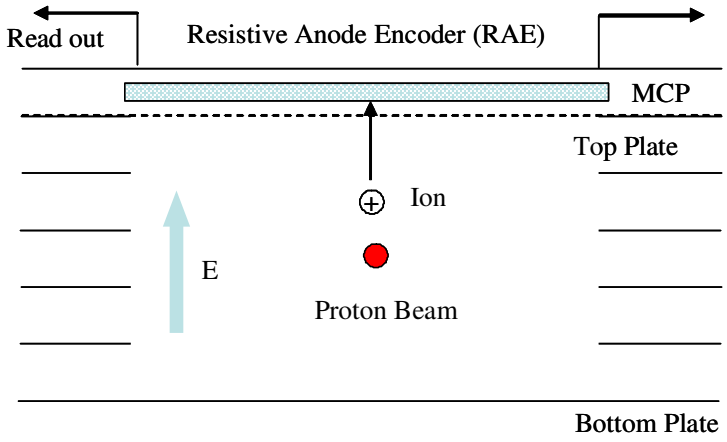

Figure 4.3: Scheme of the ionization residual gas monitor. The ionized residual gas drifts to the upper MCP along the electric field.

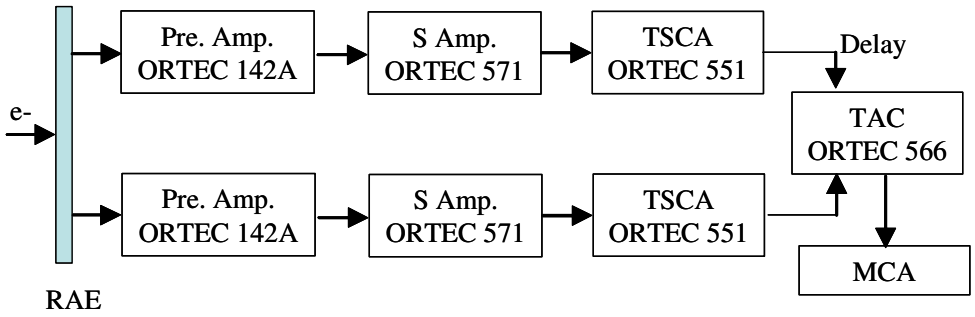

Figure 4.4: Block diagram of the signal processing for the ionization residual gas monitor.

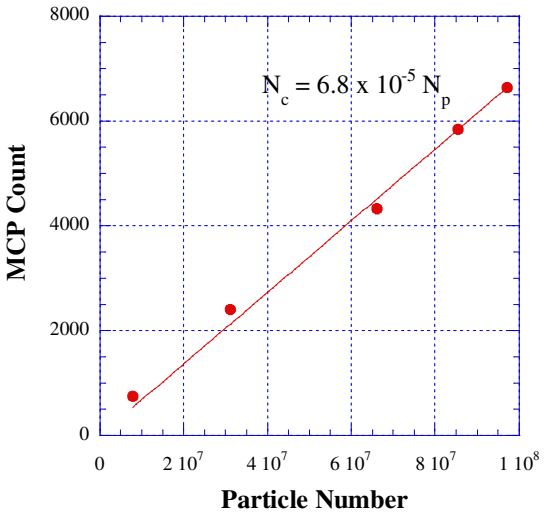

Figure 4.5: Relation between the circulating particle number and the counting rate of the ionization monitor. The particle number was calculated from the DC-CT.

where L_{mcp} is 15 mm, f_{rev} is 1.61 MHz and η is 1.0.

The absolute number of this coefficient was measured experimentally by a DC current transformer (DC-CT, Bergoz-PCT) at a high intensity of the beam. Figure 4.5 shows the relation between the counting rate and the particle number. The particle number is calculated from the DC-CT. The counting rate is proportional to the stored particle number as expected. The coefficient is,

$$N_c \;=\; 6.8 \times 10^{-5}\; N_p \;\; (count/sec). \tag{4.5}$$

It is supposed that the difference from the calculation mostly comes from the variation of the vacuum pressure.

The most important parameter of the monitors at this experiment is the lowest limit of the measurable particle number. It is determined by the competition between the signal rate and the background rate. The advantage of this monitor is the low background using discriminators and the TAC. The typical background rate is around 0.01 count/sec. From Eq.(4.5), the minimum number becomes around 200 particles, but in practice, 500 particles is the lowest limit in the measurement. The typical measurement time is 600 sec at a particle number of 1000, which is enough short compared with the beam lifetime of 17000 sec.

The disadvantage of this monitor is that the counting rate depends on the vacuum pressure. The independent measurement is necessary in order to avoid the effect of the uncontrollable change of the vacuum pressure.

4.1.2 Bunch Signal Monitor

When the beam is bunched by the RF voltage, a electric signal is induced at the pickup electrode. Let us consider the bunched beam current I(t) as the Gaussian profile,

$$I(t) = \frac{ZeN_p}{\sqrt{2\pi}\sigma_t} \exp\left(\frac{-t^2}{2\sigma_t^2}\right) \tag{4.6}$$

where Ze is the ion charge, σ_t is the rms bunch length. This formula can be expanded,

$$I(t) = \frac{ZeN_p}{T_0} + \sum_{n=1}^{\infty} I_n \cos(n\omega_0 t) \tag{4.7}$$

$$I_n \equiv \frac{2ZeN_p}{T_0} \exp\left(\frac{-(n\omega_0\sigma_t)^2}{2}\right) \tag{4.8}$$

where T_0 and ω_0 are the revolution time and the revolution frequency of the beam. The induced charge Q(t) on the pickup electrode is,

$$Q(t) = \frac{\phi}{2\pi}\frac{I(t)}{\beta c} L_p \tag{4.9}$$

where ϕ is the opening angle covered by the electrode, βc is the velocity of the ion, L_p is the length of the electrode. The equation of the system is (see Fig.4.6),

$$\frac{-dQ(t)}{dt} = \frac{V(t)}{R} + C\frac{dV(t)}{dt}, \tag{4.10}$$

where R is the input impedance of the amplifier and C is the total capacitance in this system. We define the n-th harmonic of the voltage V_n,

$$V(t) \;=\; \sum_{-\infty}^{\infty} V_n \exp(\mathrm{i}n\omega_0 t). \tag{4.11}$$

From Eqs.(4.10, 4.11)

$$V_n \;=\; \frac{2ZeN_p}{T_0}\frac{\phi}{2\pi}\frac{\mathrm{i}n\omega_0 R}{1+\mathrm{i}n\omega_0 RC}\frac{L_p}{\beta c}\exp\left(\frac{-(n\omega_0\sigma_t)^2}{2}\right). \tag{4.12}$$

The output voltage V_n is proportional to the particle number N_p. If the coefficient is known, the particle number can be calculated from the pickup voltage.

For the bunch signal monitor, two kinds of pickups are used. One is a position monitor pickup. It is already shown in Fig.2.19. It has four triangle plates with the length of 20 cm. One of the plates is used for the bunch signal monitor. The head amplifier is a SA-230F5 (NF Corporation). The input and output impedance is 50 Ω and the voltage gain is 200. The bandwidth is 400 Hz to 140 MHz. The noise level of this amplifier is very low. The noise figure is 0.6 dB and the input referred noise voltage is 0.25 nV/$\sqrt{\mathrm{Hz}}$.

Another pickup is a helical type pickup. It was developed for the storage ring, TARN at INS, Tokyo University [61]. Figure 4.7(a) shows the schematic view of the electrode. It is a

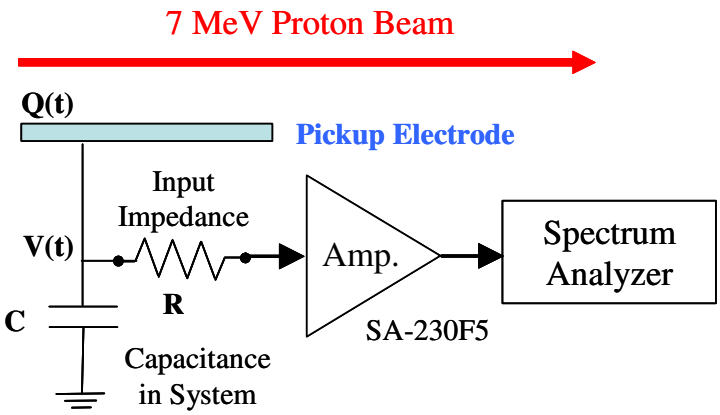

Figure 4.6: Relation between the circulating particles number and the measured voltage by the position monitor pickup. The particle number was calculated from the DC-CT.

traveling-wave type electrode and the phase velocity of the electric signal coincides with the ion velocity (7 MeV proton) in order to increase the signal amplitude. The geometry of the electrode satisfies the relation,

$$2\beta(L_w + L_h) = L_p, \tag{4.13}$$

where the dimensions of L_w, L_h and L_p are shown in Fig.4.7(a). The turn number of the electrode is 11.5. Figure 4.7(b) shows the photo of the helical electrode. The helical type pickup is more sensitive than the position monitor pickup and suitable for the small particle number measurement. Figure 4.8 shows the block diagram of the electric circuit for the helical type pickup. The helical type pickup can be considered as a long strip line. The one end is connected to the amplifier and the terminator is attached on the other end. The amplifier is a SA-230F5, which is the same amplifier as that of the position monitor pickup.

The absolute number of the particle was calibrated using the DC-CT. Figure 4.9 shows the relation between the particle number and the measured voltage from the position monitor pickup. The particle number was calculated from the DC-CT output. The pickup voltage V_p was measured by the spectrum analyzer (Agilent 4395A). The measured frequency is 3.22 MHz, which is the second harmonic. The first harmonic of 1.61 MHz cannot be used with the small particle number, because the leakage of RF signal from the RF cavity is mixed. The fitted result is,

$$V_p \quad = \quad 8.0 \times 10^{-8} N_p \ (mV). \tag{4.14}$$

The calculated coefficient from Eq.(4.12) is $7{\times}10^{-8}$ mV/particle. The measurement is consistent with the calculation.

The difference of the sensitivity between the position monitor pickup and the helical type pickup is 35.4 dB at the same beam intensity. The output voltage of the helical type pickup

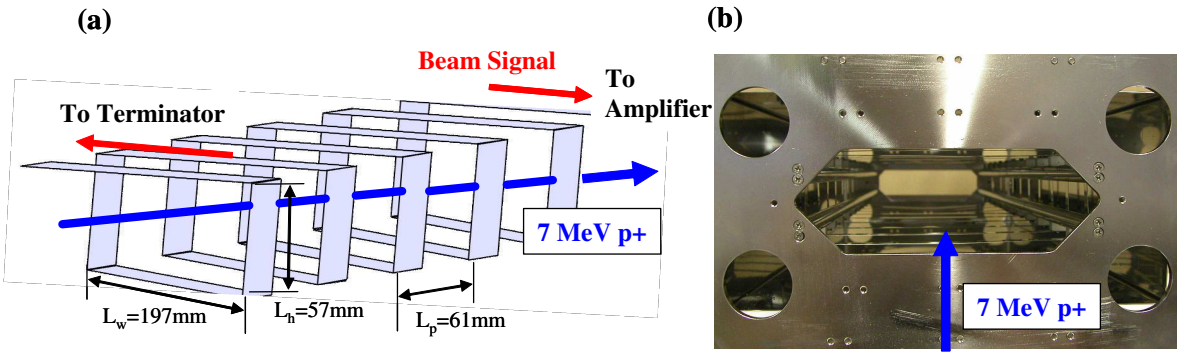

Figure 4.7: Schematic view of the helical electrode (a) and the photo of the a helical type pickup (b).

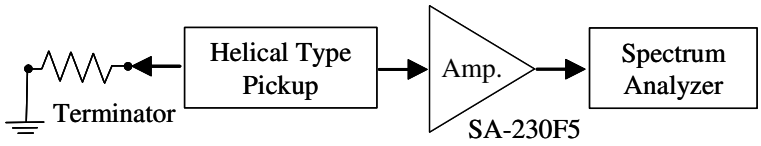

Figure 4.8: Block diagram of the electric circuit for the helical type pickup.

V_h is,

$$V_h \quad = \quad 4.7 \times 10^{-6} N_p \ (mV). \tag{4.15}$$

The background level of the spectrum analyzer is -116 dBm, which corresponded to 0.3 μV. The minimum measurable numbers are 10000 and 200 by the position monitor pickup and the helical type pickup, respectively.

4.1.3 Comparison of the Measurements

Table 4.1 shows the list of the above measurement methods and the minimum measurable particle number. Figure 4.10 shows a comparison of the ionization monitor and the bunch signal monitor. The horizontal axis is the particle number measured by the ionization monitor from Eq.(4.5). The vertical axis is the particle number measured by the bunch signal monitor from Eq.(4.14, 4.15). The position monitor pickup was used at the high intensity and the helical type pickup was used at the low intensity. The results of the two methods agree within ± 10 % from 1×10^8 to 500 protons.

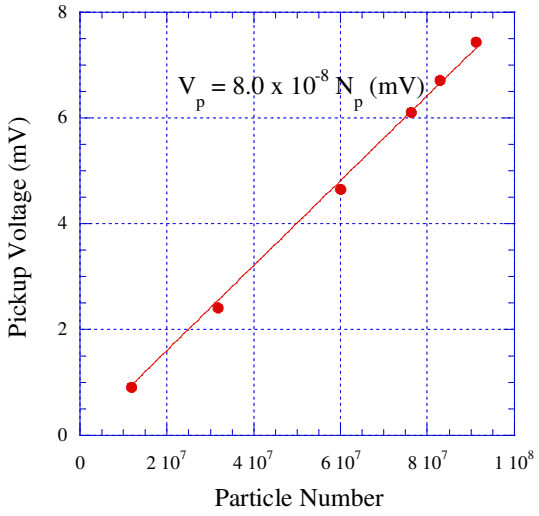

Figure 4.9: Relation between the circulating particles number and the measured voltage by the position monitor pickup. The particle number was calculated from the DC-CT.

Table 4.1: Comparison of the methods for the particle number measurement.

Method	Minimum Particle Number
DC-CT	10^7
Residual gas monitor	500
Position monitor pickup	10000
Helical type pickup	200

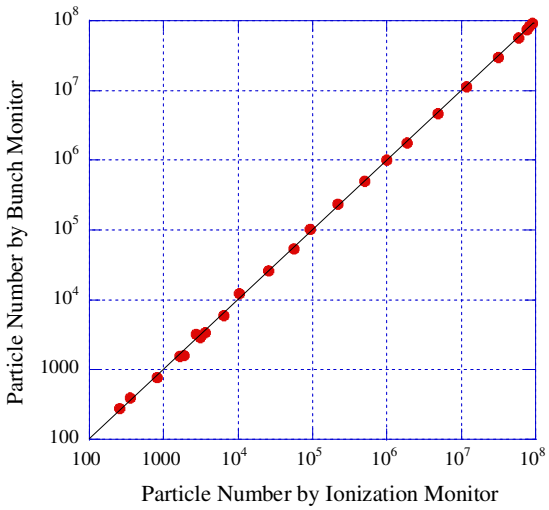

Figure 4.10: Comparison of the particle number measured by the ionization monitor and the bunch signal monitor. The position monitor pickup was used at the high intensity and the helical type pickup was used at the low intensity.

4.2 Momentum Spread Measurement

4.2.1 Basics of Schottky Noise

In the ordering experiments, the ion beam is coasting without RF bunching. The momentum spread of the protons is measured from the Schottky noise spectrum. Let us consider a single particle circulating in the ring. The beam signal is observed by a beam pickup. The schematic view of the observed signal is shown in Fig. 4.11 in the time domain (a) and in the frequency domain (b), where T_{rev} and f_{rev} are the revolution time and frequency, respectively. The pickup signal I(t) in the time domain is,

$$I(t) = Zef_{rev} \sum_{n=-\infty}^{\infty} \delta\left(2\pi f_{rev} t - 2\pi n\right). \tag{4.16}$$

In the frequency domain

$$I(t) = Zef_{rev}[1 + 2\sum_{n=0}^{\infty} \cos(2\pi n f_{rev} t)]. \tag{4.17}$$

For N particle with the same revolution frequency and the random phase, the Schottky noise power of n-th harmonic P_n is

$$P_n = R\langle I^2\rangle = R\langle[2Zef_{rev}\sum_{i=0}^{N}\cos(n\theta_i)]^2\rangle, \tag{4.18}$$

$$= 4RZ^2e^2f_{rev}^2\left(\frac{N}{2}\right), \tag{4.19}$$

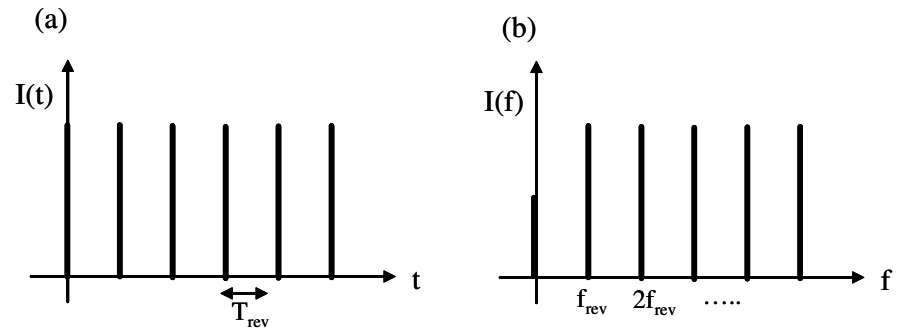

Figure 4.11: Signal from a single particle in the time domain (a) and in the frequency domain (b) [62].

where R is the input impedance of the amplifier. This equation shows that the Schottky noise power is proportional to the particle number. If the particle have a different revolution frequency,

$$\delta f = -n f_0 \eta \frac{\delta p}{p}, \tag{4.20}$$

where f_0 is the revolution frequency of the reference particle and η is given by the following formula (see Appendix B.1),

$$\eta = \left(\frac{1}{\gamma_{tr}^2} - \frac{1}{\gamma^2} \right). \tag{4.21}$$

Using this relation, the momentum spread can be measured from the frequency spread of the Schottky noise spectrum.

4.2.2 Schottky Noise Spectrum

The Schottky noise power is proportional to the particle number from Eq.(4.19), while the power of the bunch single is proportional to square of the particle number from Eq.(4.12). Therefore, the Schottky noise power is smaller than the bunch signal and only the helical type pickup is used for the Schottky noise measurement because of its high sensitivity.

Figure 4.12 shows Schottky noise spectra of the cooled proton beam. The particle number was 9×10^7 (a) and 1×10^7 (b). The center frequency was 48.3 MHz, which was the 30th harmonic of the revolution frequency (1.61 MHz). The harmonic is determined to maximize the signal to noise ratio. When the particle number is larger than 1×10^7, the density modulation is induced in the velocity space due to the collective effect [63]. Two peaks appears in the Schottky noise spectrum (see Fig.4.12a). In order to extract the information of the momentum spread from this spectrum, we have to introduce a model of the instability (beam

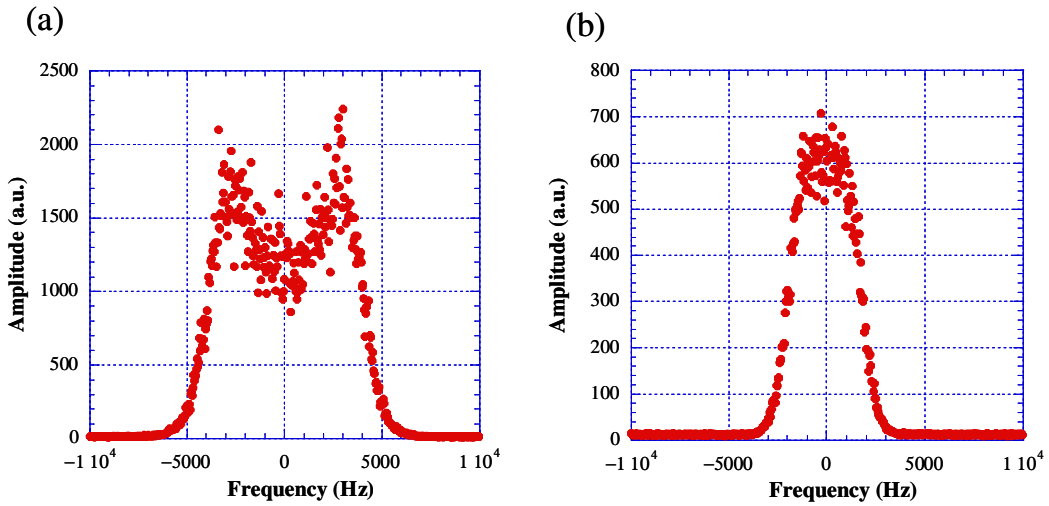

Figure 4.12: Schottky noise spectrum of the cooled proton beam with the particle number of 9×10^7 (a) and 1×10^7 (b).

impedance) and the results depend on the accuracy of the model. In the ordering experiments, the momentum spread was measured at less than 1×10^7 particles, because the high intensity beam was not interesting for the ordering.

The frequency spread is defined as 1σ of the fitted Gaussian function on the measured spectrum. It is 1.5×10^3 Hz at the spectrum (b), which corresponds to the momentum spread of 6.2×10^{-5} from Eq.(4.20).

4.2.3 Limit of Schottky Noise Measurement

The Schottky power $P_{Schottky}$ is defined by the integral of the Schottky noise spectrum. If the spectrum is Gaussian distribution, the Schottky power is,

$$P_{Schottky} = \sqrt{2\pi} P_S \sigma_f, \tag{4.22}$$

where P_S is the Schottky peak power and σ_f is the rms frequency spread of the Schottky noise spectrum. Because $P_{Schottky} \propto N_p$ and $\sigma_f \propto N_p^{0.3}$ (see Section 5.2.1), the Schottky peak power is proportional to $N_p^{0.7}$, where N_p is the particle number. At Fig.4.12(b), the peak power corresponds to -92 dBm at the particle number of 10^7. The Schottky peak power P_S can be written empirically,

$$P_S\ (dBm) = -92 + 7\log_{10}\left(\frac{N_p}{10^7}\right). \tag{4.23}$$

When the particle number is 10^3 and 10^4, the expected Schottky peak power is -120 dBm and -113 dBm, respectively.

On the other hand, the noise power P_N is,

$$P_N = \int \frac{\left(V_A^2 + V_R^2 + V_S^2\right)}{4R} F(f) df, \tag{4.24}$$

where V_A is the input referred noise voltage of the amplifier. V_R and V_S are the thermal noise voltage of the terminator and the helical type pickup. R is the characteristic impedance of 50 Ω and $F(f)$ is the filter function of the spectrum analyzer (Rohde & Schwarz - FSEA), which is determined by the resolution band width (RBW). For the Schottky measurement, the frequency span is small and the noise power is constant within the span. The noise power is,

$$P_N \cong \frac{\left(V_A^2 + V_R^2 + V_S^2\right)}{4R} \int F(f) df, P_N \cong \frac{\left(V_A^2 + V_R^2 + V_S^2\right)}{4R} \alpha \Delta f, \tag{4.25}$$

where Δf is the RBW and the α is the constant of 1.03, which was measured using a single frequency signal from a signal generator. Each noise voltage was measured in the following way. When the short plug was attached on the amplifier without helical type pickup, the value of V_A was measured. The sum of the V_A and V_S was measured with the helical type pickup and the short plug and the sum of the V_A,V_S and V_R was measured with the helical type pickup and the terminator.

Table 4.2 shows the measured values for each components. The input referred noise voltage of the amplifier was 0.18 nV/$\sqrt{\text{Hz}}$, while the catalog specification was 0.25 nV/$\sqrt{\text{Hz}}$. The noise of the helical type pickup itself was smaller than others. The thermal noise of 50 Ω terminator was 0.66 nV/$\sqrt{\text{Hz}}$. The amplitude of the thermal noise is given by Nyquist formula,

$$V_R(R) = \sqrt{4 k_B T B R}, \tag{4.26}$$

where B is the band width and R is the resistance. It is 0.91 nV/$\sqrt{\text{Hz}}$ at the temperature of 300 K. The measured one is about 70 % of this calculation but the terminator was the largest noise source.

The amplifier terminator is a trick to reduce this noise. If the input referred noise voltage of the amplifier is smaller than the thermal noise of 50Ω, the amplifier is the better termination. When the same type of the amplifier was attached instead of the resistive terminator, it became 0.36 nV/$\sqrt{\text{Hz}}$. It attained the 44 % reduction of the noise voltage. The total input noise voltage of the amplifier was 0.43 nV/$\sqrt{Hz}$. Since the typical RBW is 50 Hz and the voltage gain of the amplifier is 200, the noise voltage is 0.6 μV, which corresponded to the noise power P_N of -117 dBm. Therefore, the lowest particle number for the momentum spread measurement is around 2000. In practice, the minimum particle number depends on the background condition and usually around 1000.

Table 4.2: Measured noise voltage for each component.

Noise Source	Noise Voltage
Amplifier (input referred)	V_A : 0.18 nV/$\sqrt{\text{Hz}}$
Helical type pickup	V_S : 0.16 nV/$\sqrt{\text{Hz}}$
50 Ω Terminator	V_R : 0.66 nV/$\sqrt{\text{Hz}}$
Amplifier Terminator	V_R' : 0.36 nV/$\sqrt{\text{Hz}}$

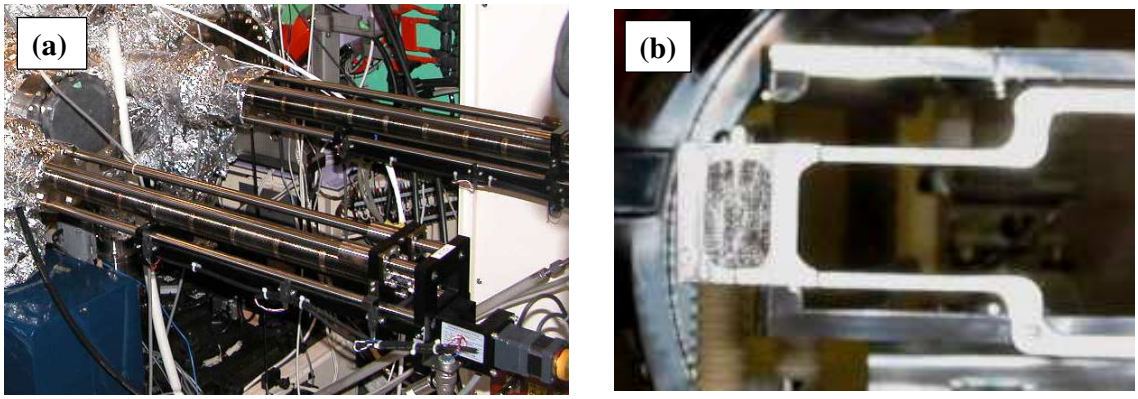

Figure 4.13: External view of the beam scraper (a) and head of the scraper (b). It is inserted into the circulating beam in the horizontal direction.

4.3 Transverse Emittance Measurement

4.3.1 Beam Scraper

The beam radius is measured by a beam scraper. This method was used at ESR in Ref.[18] to measure the beam radius of the highly charged heavy ions. The photo of the beam scraper is shown in Figure 4.13. It is inserted into the circulating beam in the horizontal direction. The scraper is controlled by a stepping motor with the minimum step of 0.8 μm.

The sequence of the beam size measurement is expressed schematically in Fig.4.14. At first, the particle of 10^8 is injected and cooled in the ring. The typical beam diameter is around 1 mm. Then the scraper is moved into the circulating beam and stopped at a certain position for 0.1 second, and then removed back away. The scraper kills a part of the beam and reduces the particle number. Because the intrabeam scattering is reduced under the constant electron cooling, the beam size gets smaller.

The rms beam radius σ_b is determined from the distance L_s (see Fig.4.14) between the stopped position of the scraper and that where the beam is completely lost. The relation between σ_b and L_s is estimated from the beam simulation by the BETACOOL program [54].

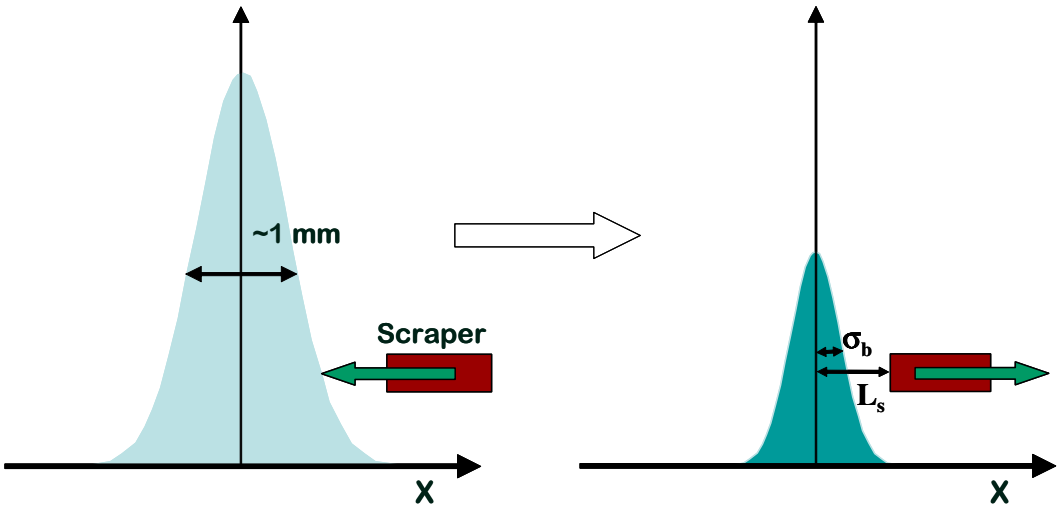

Figure 4.14: Schematic view of the sequence of the beam size measurement. The cooled beam was reduced by the scraper (left) and the rms beam radius σ_b was determined from the distance L_s (right).

This code has been developed by the electron cooling group of Joint Institute for Nuclear Research (JINR). It can calculate the beam dynamics in a storage ring with many effects, such as the cooling, the intrabeam scattering, the scattering with the residual gas and so on. The input parameters of the simulation are the measured cooling force, the intrabeam scattering based on the Martini model and the scattering with the residual gas. The measured vacuum pressure and the gas components are used for the simulation. The simulation results are shown in Fig.4.15. The calculated beam radius is proportional to the position of the scraper. The distance L_s corresponds to $3.5\times\sigma_{beam}$.

The measurement errors of the beam radius came from the drift of the beam center and the reproducibility of the mechanical positioning of the scraper. The error of σ_{beam} was estimated to be $\pm 7\mu m$.

4.3.2 Comparison with Ionization Monitor

The ionization residual gas monitor can measure the horizontal beam profile. The electric charge amplified by the MCP reaches to a certain point on the RAE and read out from the both sides of the RAE. Because the RAE has a large resistance of 250 kΩ, the time constant (RC) of the signal pulse depends on the initial position of the RAE. This characteristic is used for the profile measurement. Figure 4.16 shows an example of the horizontal beam profile for the cooled proton beam.

The drawback of this monitor is the resolution. Because the ionized gas has an initial thermal energy, it moves in the horizontal direction during the drift time. This horizontal

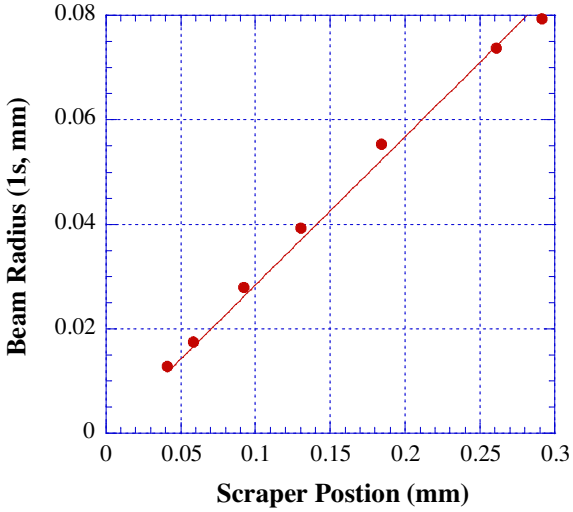

Figure 4.15: Calculated rms beam radius σ_b as a function of the stopped position of the scraper. σ_b was determined by the beam simulation using BETACOOL program.

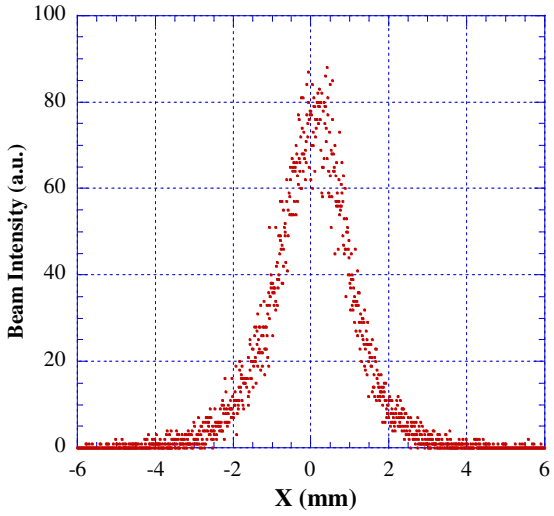

Figure 4.16: Beam profile measured by the ionization residual gas monitor. The particle number was 10^7.

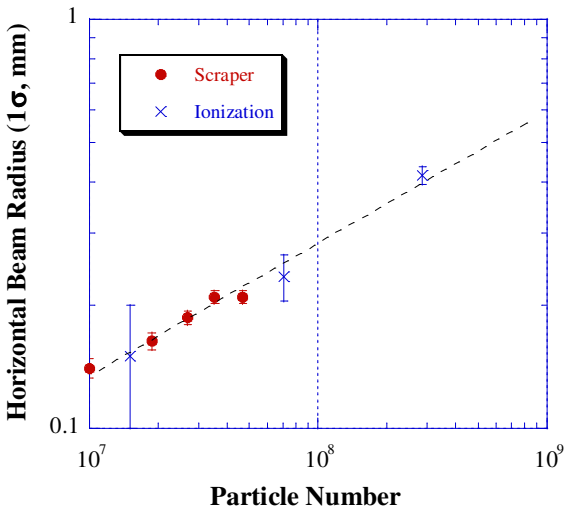

Figure 4.17: Comparison of the measured horizontal beam radius (1σ) between the two methods. The electron current of the cooler was 25 mA. The data by the scraper is shown by the mark $\bullet$ and the data by the ionization monitor is shown by the mark $\times$.

drift X_d determines the resolution in the horizontal direction,

$$X_d = \sqrt{\frac{2m_i L_d}{eE}} v_x, \tag{4.27}$$

where m_i is the mass of the residual gas ion, L_d is the drift length between the ionization point and the MCP and E is the electric field. Because this resolution was normally 0.3 mm and it was impossible to measure the beam radius less than 0.1 mm by this monitor. However, the ionization monitor was very useful to verify the scraper method. Especially, the calculated ratio of 3.5 between σ_b and L_s had to be checked experimentally.

The beam profiles of the cooled protons were measured by two methods with the large particle numbers. Figure 4.17 shows the results. The difference of the β-function at the two monitors was only 4 % and the effect on the beam size was smaller than the measurement error. Both methods gave the consistent results. This result shows that the scraper method is valid for the beam size measurement.

Chapter 5

Experiments of Proton Ordering

At the beginning, a longitudinal and a transverse beam temperature are defined using the momentum spread $\delta p/p$ and the transverse emittance ϵ, following Ref.[18].

From Eq.(1.1), the longitudinal temperature $T_{\parallel}$ is defined,

$$k_B T_{\parallel} \equiv m_i \langle v_z^2 \rangle \tag{5.1}$$

$$= m_i \beta^2 c^2 \left(\frac{\delta p}{p} \right)^2, \tag{5.2}$$

where βc is the velocity of the particle. The effective transverse temperature $T_{\perp}$ is defined,

$$k_B T_{\perp} \equiv \frac{1}{2} m_i \left(\langle v_x^2 \rangle + \langle v_y^2 \rangle \right), \tag{5.3}$$

$$= \frac{1}{2} m_i \beta^2 c^2 \gamma^2 \left(\theta_x^2 + \theta_y^2 \right), \tag{5.4}$$

$$where \qquad \theta_x^2 \equiv \langle \left(\frac{dx}{ds} \right)^2 \rangle, \quad \theta_y^2 \equiv \langle \left(\frac{dy}{ds} \right)^2 \rangle, \tag{5.5}$$

where γ is the Lorentz factor of the beam. The divergence $\theta_{x,y}$ can be written by the emittance ϵ,

$$\theta_{x,y} = \sqrt{\frac{\epsilon}{\beta_{x,y}}}, \tag{5.6}$$

where $\beta_{x,y}$ is the horizontal and vertical β-functions, respectively. The horizontal and vertical emittances are assumed to be equal, because the cooling force is symmetric in the horizontal and the vertical directions. Note that the transverse temperature in Eq.(5.4) varies in the ring due to the periodic focusing structure, while the transverse emittance is constant in the ring. The ring-averaged temperature is defined in the following. In a circular accelerator, the mean betatron function is given by the approximation,

$$\langle \beta_{x,y} \rangle \cong \frac{R_{ring}}{\nu_{x,y}}, \tag{5.7}$$

where R_{ring} is the average radius of the ring, and $\nu_{x,y}$ are the horizontal and vertical betatron tunes, respectively. The transverse temperature is,

$$k_B T_\perp \cong \frac{1}{2} m_i c^2 \beta^2 \gamma^2 \frac{\nu_x + \nu_y}{R_{ring}} \epsilon. \tag{5.8}$$

5.1 Experimental Procedure

The procedure of the ordering experiments is following.

1. The proton beam is injected into S-LSR and cooled.
2. The particle number is reduced by the horizontal scraper.
3. The number of the survived particles is measured by the residual gas ionization monitor and the bunch signal monitor.
4. The momentum spread is measured from the Schottky noise spectrum.

In the step (1), the typical number of the injection protons is 10^8 with the stored current of 30 μA. After the electron cooling of around 20 seconds, the beam size and the momentum spread become 1 mm and 2×10^{-4}, respectively.

In the step (2), the horizontal scraper is inserted into the circulating beam. The number of the particle is reduced from 10^8 to a certain number. Figure 5.1 shows the relation between the position of the scraper and the number of the survived particles. The horizontal axis is the stopped position of the beam scraper. When the scraper is inserted to 105.5 mm, the whole beam was lost completely. By this scraper method, the particle number is well controlled from 10^7 to 1000.

In the step (3) and (4), the particle number and the momentum spread are measured. It takes about 10 minutes for the event accumulation at the ionization residual gas monitor and for the averaging of the spectrum analyzer. This measurement time is short enough compared with the beam lifetime of 17000 seconds.

The operating parameters of the storage ring and the electron cooler are shown in Table 5.1 in the ordering experiment. The beam energy of the proton is 7 MeV, which is the same as the injection energy from the linac. The betatron tunes are 1.645 and 1.206 in the horizontal and vertical directions, respectively. It is the standard operating point for electron cooling experiments. The twiss parameters of one period in the ring are shown in Fig.5.2. It is calculated by MAD8. The vertical β-function and the horizontal dispersion is almost constant in the ring and the averaged values are 3.1 m and 1.7 m, respectively. The horizontal β-function varies from 1.6 m at the drift space to 3.9 m at the bending magnet.

The electron cooler is located at the center of the drift space. The lattice has mirror symmetry at the center of the drift space and the beam size is almost constant in the effective area (440 mm) of the electron cooler. The electron currents of the cooler are 25 mA, 50 mA

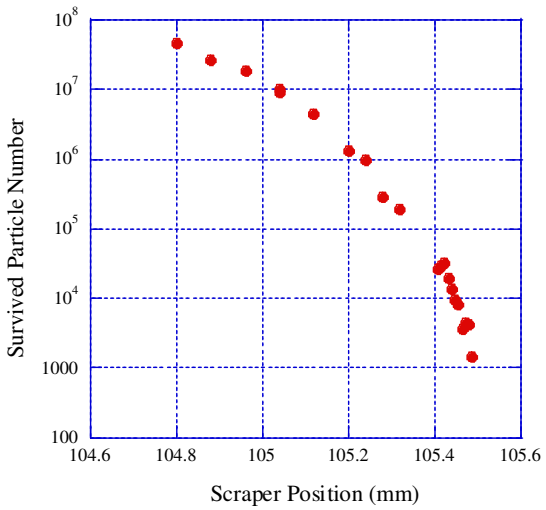

Figure 5.1: Number of the survived particles after the horizontal scraper is inserted. The horizontal axis is the position of the scraper.

and 100 mA in the experiment. We have never measure with the higher electron current, because the beam heating was observed at the cooling force measurement (see Fig.3.13(b)). Most of the data have been taken with the electron current of 25 mA. The higher electron current leads to the larger cooling force from Eq.(3.24) but the electron temperature also becomes higher from Eq.(3.16). The effect of the electron current on the ion temperature is discussed later.

5.2 Longitudinal Dynamics of Beam Ordering

5.2.1 Anomalous Behavior of Momentum Spread

The first systematic measurement of the momentum spread for cooled protons was carried out at S-LSR in February, 2006. Figure 5.3 shows the momentum spread as a function of the particle number [56]. The electron current was 50 mA. The momentum spread decreased according to the reduction of the particle number down to 20000. It is well known that the relation between the momentum spread δp/p and the particle number N_p can be fitted by the function,

$$\frac{\delta p}{p} = A N_p^{\alpha}, \tag{5.9}$$

where A is the constant. The fitted α was 0.38 above the 20000 particles. On the other hand, the momentum spread became constant at 5×10^{-6} below 20000 particles. This result was similar to that of NAP-M [16] but the saturated momentum spread and the coefficient α at

Table 5.1: Operating parameters of the storage ring and the electron cooler.

Beam	
Ion Species	Proton, 7 MeV
Revolution Frequency	1.61 MHz
Life Time (with Cooling)	1.7×10^4 sec
Ring	
Betatron Tune	(1.645, 1.206)
Maximum β-function	(3.9 m, 3.2 m)
Maximum Horizontal Dispersion	1.8 m
Momentum Compaction	0.502
Vacuum Pressure	$1 \times 10^{-8} Pa$
Electron Beam	
Energy	3.8 keV
Beam Current	25 mA, 50 mA, 100mA
Beam Diameter	50 mm
Beam Density	2.2×10^6 e^-/cm^3 at I_e=25 mA
Expansion Factor	3

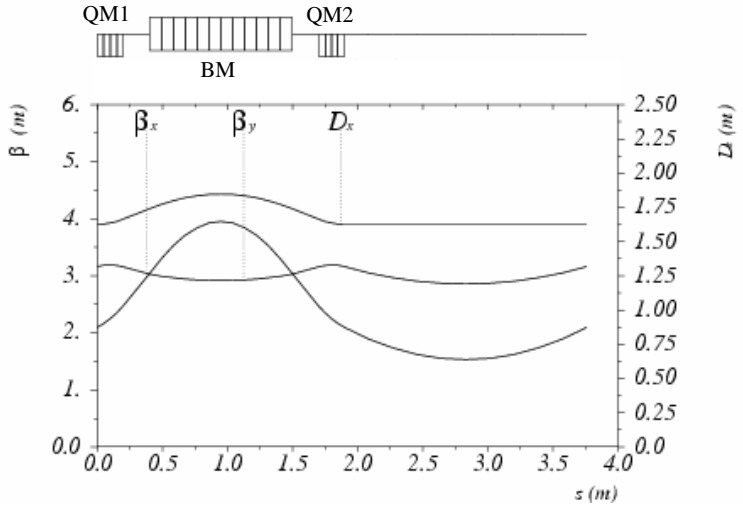

Figure 5.2: Twiss parameters in one period at the ordering experiment. The betatron tune is (1.645, 1.206).

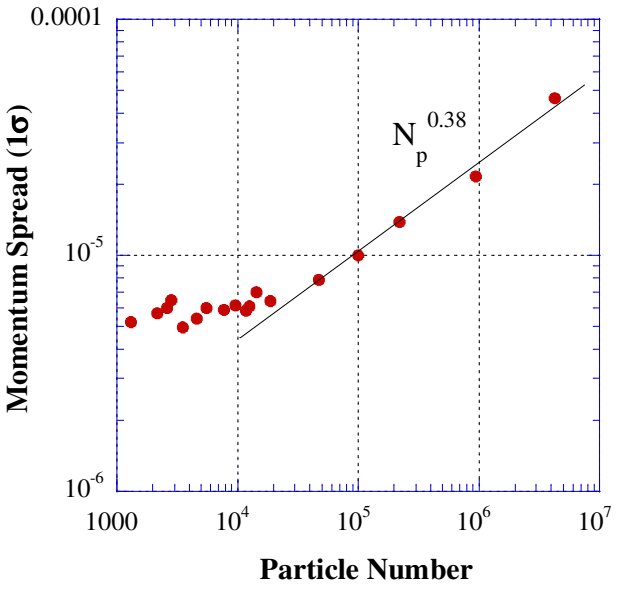

Figure 5.3: Measured momentum spread of protons as a function of the particle number. The electron current was 50 mA. It was performed in February, 2006.

NAP-M were 1×10^{-6} and around 1, respectively. The jump of the momentum spread like ESR experiment was not observed.

After the experiments, the following improvements were performed in the ring and the electron cooler.

1. Fine optimization of the ion and the electron beam alignment,
2. Improvements of the cathode power supply for the electron cooler,
3. Improvements of the power supply for the dipole magnets,
4. Reduction of the background noise of the Schottky monitor.

Concerning the item (1), we developed the optimization scheme of the beam-beam alignment using the induction accelerator, which was described in the Section 3.3. Figure 5.4 shows the momentum spread as a function of the particle number with different alignment conditions. The data of "0 mrad" is an exact alignment determined by the induction accelerator method. In the data of "0.5 mrad", the artificial misalignment of 0.5 mrad is created in the horizontal and vertical directions. The electron beam orbit is steered by Helmholtz coils in the cooling solenoid. The electron misalignment induces the beam heating and the momentum spread is saturated [64].

The item (2) was also already described at the Section 3.3. We succeeded to reduce the ripple less than 1×10^{-5}. The ripple was also a cause of the saturation of the momentum

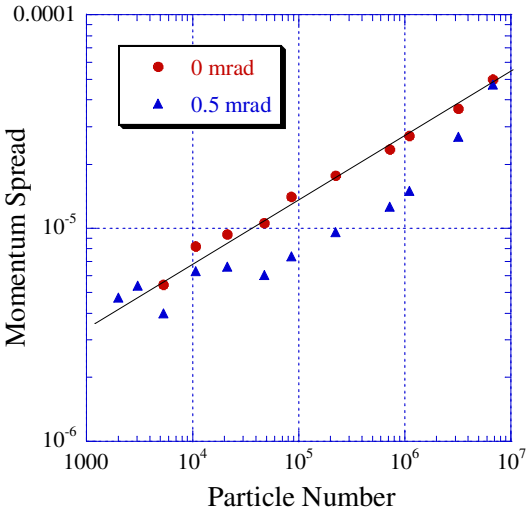

Figure 5.4: Momentum spread as a function of the particle number with (0.5 mrad) and without (0 mrad) misalignment. The misalignment angle was 0.5 mrad in the horizontal and vertical directions.

spread. The reduction of the cathode voltage drift described at the Section 3.3 is also important, because it takes some minutes for the averaging of the Schottky noise spectrum. If the electron energy drifts during the averaging, the momentum spread appears larger than the true value. The drift is 2×10^{-5}/hour after the improvement of the control system, which corresponds to the momentum spread of 1×10^{-5}/hour. This is almost tolerable for the averaging for some minutes.

The power supply for the bending magnet was adjusted to minimize the ripple. The ripple level was decreased from 5×10^{-5} to 5×10^{-6}. The drift of the output current is less than 1×10^{-6}/hour. In the same reasons of the electron cathode power supply, the ripple and the drift of the bending magnet power supply increased the momentum spread of protons. However, the bending magnets at S-LSR are made of a block iron and the magnetic response is rather slow. Therefore, it is considered that the effect of the power supply ripple was small at the experiment in February, 2006.

Concerning the item (4), the most effective improvement is the amplifier termination, which is described in the Section 4.2.3. The background level of the Schottky noise spectrum was improved by 4 dB by replacing the terminator. It enables the observation of the momentum spread even with the particle number of 1000.

After these improvements, we succeeded to observe the first indication of the jump of the momentum spread for protons in July, 2006 and reported in Ref.[37]. The final results were reported in Ref.[25] after the additional measurements. Figure 5.5 shows a momentum spread of the proton beam as a function of the particle numbers N_p in the ring. The electron current

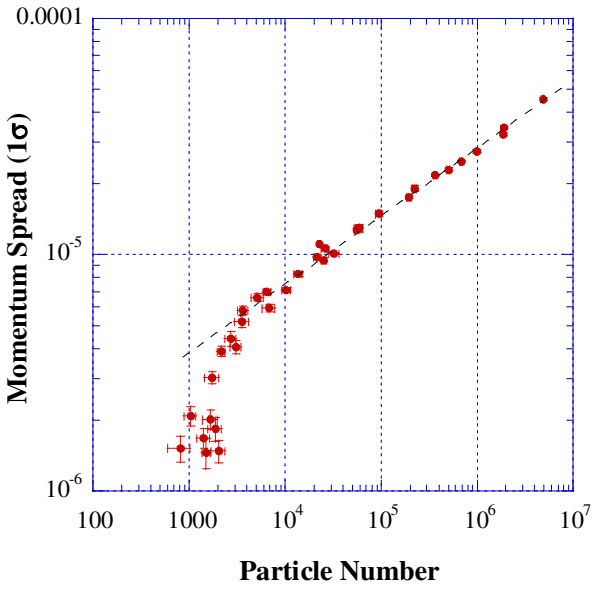

Figure 5.5: Momentum spread as a function of the particle numbers in the ring with electron current of 25 mA. The momentum spread drops at a particle number of 2000.

was 25 mA. The particle number and the momentum spread were measured by the ionization monitor and the Schottky noise spectrum, respectively, which were described in the previous Chapter. The momentum spread is defined as 1σ of the fitted Gaussian function to the momentum distribution. The momentum spread decreased monotonically above a particle number of 4000 without saturation. The coefficient α in Eq.(5.9) was 0.29. Compared with Fig.5.3, the value of α changed and the saturation of the momentum spread disappeared. At the particle number of 2000, the momentum spread dropped abruptly at 3.5×10^{-6}. From Eq.(5.2), the corresponding longitudinal transition temperature was 0.17 meV. This is the first observation of the jump of the momentum spread for protons. It is considered that the abrupt drop is evidence of ordering of the protons. In contrast, the momentum spread of protons became constant below certain particle numbers at NAP-M [16] and COSY [23], instead of the abrupt drop.

Figure 5.6 shows the Schottky noise spectra above and below the transition of the momentum spread. The particle numbers are 3600 and 2000, respectively. The resolution and video bandwidth of the spectrum analyzer are 50 Hz. The background spectrum without beams is subtracted from the measured spectra and smoothing processing is applied on them. It is clear that the width of the peak changes by factor of 4 above and below the transition. The Schottky power, which is defined by the area of the spectrum, is also greatly reduced. It will be discussed in the next section. However, there are still small noise peaks with the amplitude of ±0.1 in Fig.5.6(b), because the signal level with 2000 particles is close to the

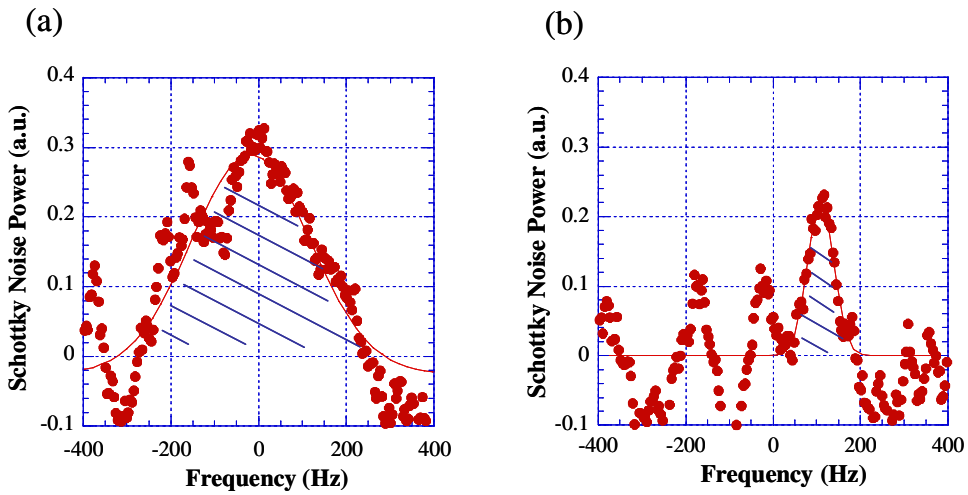

Figure 5.6: Schottky noise spectra with particle numbers of 3600 (a) and 2000 (b), respectively. The resolution and video bandwidth of the spectrum analyzer are 50 Hz.

background noise level. The width of the noise peak is almost same as the resolution band width. Such noise peaks are the source of the measurement errors.

Figure 5.7 shows the momentum spread with three different electron currents of the cooler: 25 mA, 50 mA and 100 mA. The transitions are observed with all electron currents. Above the transition, the momentum spread with an electron current of 100 mA is smaller than those of the lower electron currents, because the cooling force is proportional to the electron current. On the other hand, below the transition, the momentum spread is estimated to be 1.4×10^{-6} with electron currents of 25 mA and 50 mA. The momentum spread with the electron current of 100 mA is 1.7×10^{-6}. From Eq.(5.2), the longitudinal transition temperature with an electron currents of 25 mA is 26 μeV. The plasma parameter of protons is 2×10^{-3} with the average inter-particle distance of 1 cm from Eq.(1.6). Note that a careful treatment is necessary for an application of Eq. (4.20) below the ordering transition, because the ion motion is different below the transition. The above momentum spread is simply calculated from Eq. (4.20).

5.2.2 Anomalous Behavior of Schottky Noise Power

The areas of the Schottky noise of the two spectra in Fig.5.6 are quite different. It suggests a big drop of the Schottky noise power above and below the transition. The frequency spread of the Schottky noise is created by the momentum spread of the beam and the resolution band width of the spectrum analyzer. Therefore, the Schottky noise power P_n of the n-th

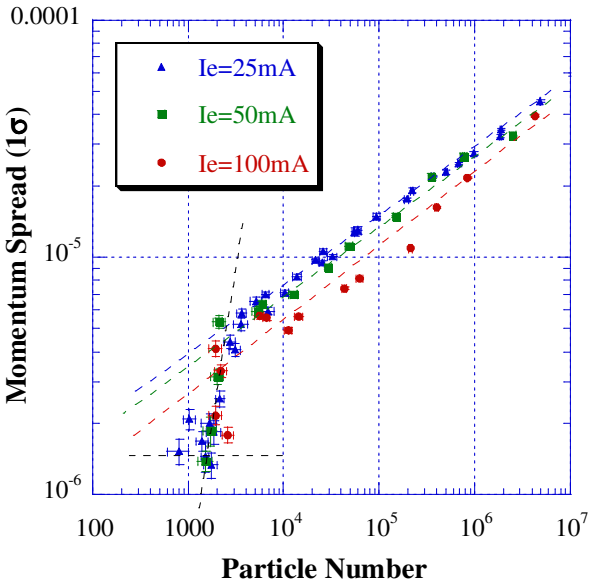

Figure 5.7: Momentum spread (1σ) as a function of the particle numbers with three different electron currents, 25 mA, 50 mA and 100 mA. The transitions are observed with all electron currents.

harmonic is defined as the integrated area of the spectrum,

$$P_n = \int_{f_n-\delta f/2}^{f_n+\delta f/2} F_{Schottky}(f)df \tag{5.10}$$

where $F_{Schottky}(f)$ is the Schottky noise spectrum, f_n is the frequency of the n-th harmonic and δf is the appropriate range of the frequency spread. Figure 5.8 shows the Schottky noise power as a function of the particle number with an electron current of 25 mA. It is proportional to $N^{0.99}$ above a particle number of 6000. This result is consistent with the relation of Eq. (4.19). At the transition point, it drops by one order of magnitude. Similar phenomena have been observed for highly charged heavy ions at CRYRING [19]. This phenomenon is one feature of the beam ordering. Because the particle motion is not random and has a sort of order below the transition, the relation of Eq. (4.19) is no longer valid.

5.3 Transverse Dynamics of Beam Ordering

5.3.1 Transverse Beam Temperature at Phase Transition

The transverse beam temperature can be estimated from the beam size. Figure 5.9 shows the measured horizontal beam size as a function of the particle numbers. The beam size was measured by the ionization residual gas monitor and the beam scraper. The electron

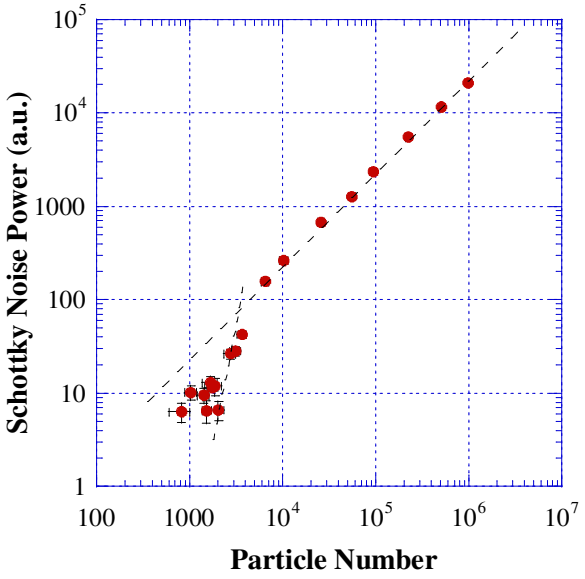

Figure 5.8: Schottky noise power as a function of a particle numbers with electron current of 25 mA. The Schottky noise power is defined as the integrated area of the spectrum. It drops at a similar transition point as the momentum spread.

current of the cooler was 25 mA. The horizontal beam radius is defined as 1σ of the fitted Gaussian function to the horizontal beam profile. The beam radius is proportional to $N^{0.28}$, and monotonically decreased even below a particle number of 10^4. The beam radius is 17 μm at a particle number of 4000, where the momentum spread starts to drop. It is impossible to determine whether there is an abrupt jump of the beam size, because of the insufficient resolution of the scraper measurement.

The horizontal emittance is $1.7{\times}10^{-4}\pi{\cdot}mm{\cdot}mrad$ at the transition of the momentum spread from Eq.(4.1), because the β-function at the scraper was 1.7 m. If it is assumed that the horizontal and vertical emittances were equal, the transverse temperature is 1 meV from Eq.(5.8). The transverse temperature is 6 times higher than the longitudinal one. The reason of this thermal imbalance state in the longitudinal and transverse direction is unknown. It might come from the characteristics of the cooling force or the field error of the solenoid coil.

The transverse electron temperature is 34 meV from Section 3.3.3. The transverse proton temperature of 1 meV is more than thirty times smaller than that of the electron. It is unusual in the standard thermodynamics. The effect of the solenoid field on electrons was pointed out by Skrinskii and Derbenev [53]. The electrons rotate around the magnetic field line with a Larmor radius. The ions interacted with a small Larmor ring of an electron, not a free electron. The Larmor radius r_L is given by,

$$r_L = \frac{m_e v_\perp}{eB_s}. \tag{5.11}$$

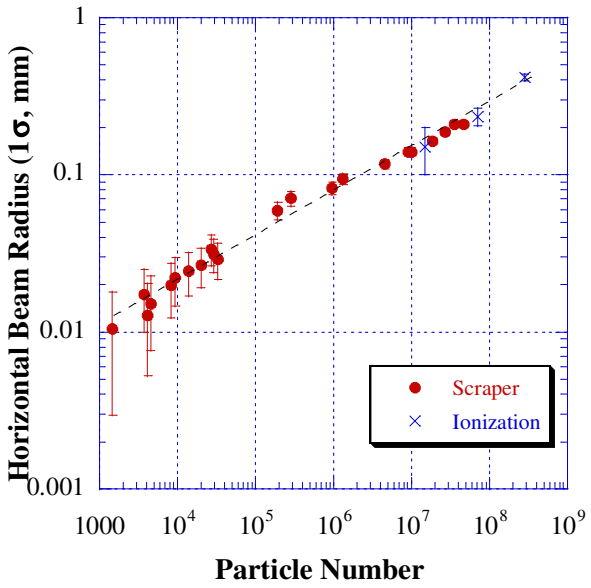

Figure 5.9: Horizontal beam radius (1σ) as a function of the particle numbers with electron current of 25 mA. They were measured by the scraper (mark $\bullet$) and the ionization residual gas monitor (mark $\times$).

where B_s is 500 Gauss, $v_\perp$ is 1.1×10^5 m/sec at S-LSR. The Larmor radius is 12 μm, which is smaller than the average inter-particle distance of electrons, $n_e^{-1/3}$=76 μm at an electron current of 25 mA. The transverse motion of the electrons looks frozen from the ions. In this condition, the ion temperature is determined only by the longitudinal electron temperature.

The magnetized electron effect was predicted theoretically [53] but it was only partially observed in the ordering experiment of C^{6+} at ESR [22], because the transverse temperature was usually determined by an intrabeam scattering, not an electron temperature. This fact is the key for the ordering of the proton beam, which is discussed in the next Chapter.

Chapter 6

Discussion of Ordering Condition

I discuss three questions about the proton ordering in this Chapter. One is a mechanism of ordering transitions for protons and highly charged heavy ions; whether they are the same or not ? The experiment of NAP-M in 1984 might suggest a singularity of protons. The second is a physics of the ordering and the crystalline beam; what are common points and differences ? Although the cooling methods and the final beam structure are different between them, the phase transition is a common keyword. The third is the lowest temperature of protons below the transition; what limits the minimum temperature ?

6.1 Ordering of Proton and Heavy Ions

The one-dimensional ordering of the highly charged heavy ions was interpreted by R.W. Hasse [21]. The illustration of his model is shown in Fig.6.1. His model is already described in Section 1.2 but is expressed in detail here. In the particle rest frame, the cooled ions with very low density move slowly in the longitudinal direction. At the same time, the ions oscillate quickly in the transverse direction with a betatron frequency. When the ions is cooled enough, the kinetic motion of the ions cannot overcome the Coulomb potential between them and the ions do not pass through each other in the longitudinal direction. Even if the particle has a finite beam size, the particles collide with the minimum impact parameter, because the typical collision rate is kHz, while the typical betatron oscillation frequency is MHz. On the other hand, when the ions are far from each other, they move freely in the longitudinal direction without Coulomb interaction, because the average inter-particle distance is very large (typically 100 mm). Although the ion position is not fixed in the particle rest frame, the time-averaged position is fixed. In this condition, the particle collisions work for the longitudinal confinement of the ions and do not induce the beam diffusion. The structure of the beam is changed from the gaseous state to this string-like ordered state through the phase transition.

This interpretation has been considered for the highly charged heavy ions, which have a strong Coulomb interaction. It is a question whether the same physical picture is valid for

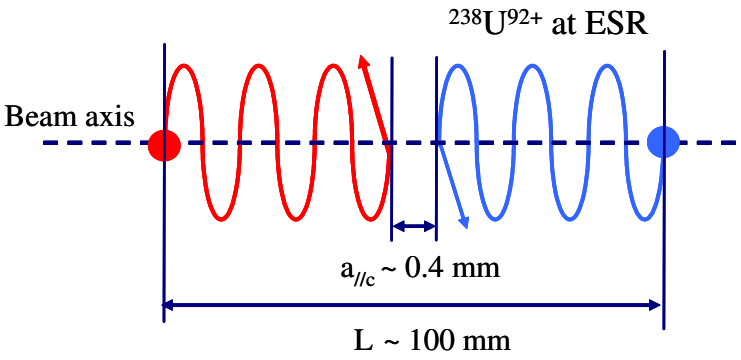

Figure 6.1: Illustration of the model of the one-dimensional ordered beam for $^{238}U^{92+}$ at ESR. The ions moves freely in the longitudinal direction with transverse betatron motion but reflected when they are close each other.

the single charged ions, especially protons, because the Coulomb interaction is much weaker than that of heavy ions. At first, let us consider the critical inter-particle distance $a_{\parallel c}$, where the Coulomb potential and the kinetic energy becomes equal.

$$a_{\parallel c} = \frac{(Ze)^2}{4\pi\epsilon_0}\frac{1}{k_B T}. \tag{6.1}$$

At ESR, the minimum longitudinal temperature of $^{238}U^{92+}$ is 30 meV and the critical distance is 400 μm, while the average inter-particle distance is 100 mm. The plasma parameter is 4×10^{-3}. At S-LSR, the minimum longitudinal temperature of p^+ is 26 μeV and the critical distance is 55 μm, while the average inter-particle distance is 10 mm. The plasma parameter is 6×10^{-3}. In both cases, the critical distances are much shorter than the average inter-particle distances. It suggests that the protons move freely in the longitudinal direction most of the time even below the transition.

For the discussion of the transition condition, the effect of the betatron oscillation must be considered. In the electron cooling, the transverse temperature is usually higher than the longitudinal one and the transverse motion has an important role for the ion ordering. I. Meshkov calculated the ordering condition, which is called "Γ_2 parameter" [65, 66]. R.W. Hasse and H. Okamoto independently calculated the reflection probability between ions by Monte Carlo simulations [21, 67]. I will compare the transition conditions of protons and heavy ions using these criteria.

6.1.1 Γ_2 Parameter

The Γ_2 parameter was introduced in Ref.[65]. This is a simple model but a good indicator of the ordering for the heavy ions. I describe it briefly according to his derivation, because it is useful to understand the physical picture of the ordering. In the model of ordering, it is

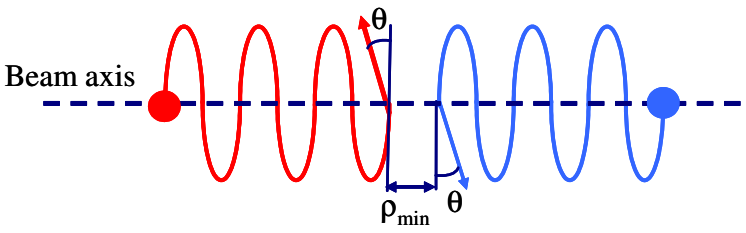

Figure 6.2: Illustration of the Rutherford scattering between two particles. The transverse motion is the betatron oscillation.

enough to consider only two particles, because the inter-particle distance is very large. Let us consider the collision of two particles in Fig.6.2. From the Rutherford scattering formula, the impact parameter ρ is given by the scattering angle θ,

$$\rho = \frac{1}{4\pi\epsilon_0}\frac{Z^2e^2}{2k_BT}\cot\frac{\theta}{2}, \tag{6.2}$$

$$\cong \frac{1}{4\pi\epsilon_0}\frac{Z^2e^2}{2k_BT_\perp}\cot\frac{\theta}{2}, \tag{6.3}$$

where the approximation of $k_BT \cong k_BT_\perp$ is used. The conditions of the reflection in the longitudinal direction are,

$$\theta > \frac{v_\parallel}{v_\perp}, \tag{6.4}$$

$$\frac{\rho_{min}}{v_\parallel} > \frac{\tau_\beta}{4}, \tag{6.5}$$

where τ_β is the period of the betatron oscillation, $v_\perp$ and $v_\parallel$ are the transverse and longitudinal velocity in the particle rest frame, respectively. The first condition is clear from Fig.6.2. The scattering angle must be large so that the longitudinal velocity changes its sign. From Eqs.(6.3, 6.4), the minimum impact parameter ρ_{min} is determined. The second condition means that if the ion traveling time along the distance of ρ_{min} is longer than the quarter of the betatron oscillation period at least, the collision with the minimum impact parameter is guaranteed. From these conditions, the following relation is derived,

$$\Gamma_2 \equiv \frac{Z^2e^2}{4\pi\epsilon_0\sigma_\perp k_BT_\parallel} > \pi. \tag{6.6}$$

In the recent study, it is reported that the threshold constant becomes 1 not π [68]. In any cases, the parameter Γ_2 is a good indicator of the ion ordering.

Table 6.1 gives the longitudinal and transverse transition temperatures and the calculated Γ_2 parameters for the experimental data. The temperature of the proton was obtained at S-LSR, and the other three kinds of ions were measured at ESR [22]. The Γ_2 parameters at the transitions are smaller than π for any ion species. They are close to around 1.

Table 6.1: Longitudinal and transverse transition temperatures and the Γ_2 parameters for the proton at S-LSR and the other three kinds of ions at ESR, which were extracted from Table 1 in Ref.[22]. It is assumed that the transverse temperature is twice of the horizontal one.

	$T_\parallel$	$T_\perp$	Γ_2
p^+	0.17 meV	1 meV	0.5
$^{12}C^{6+}$	4.0 meV	11 meV	1.8
$^{70}Zn^{30+}$	78 meV	0.64 eV	0.70
$^{238}U^{92+}$	470 meV	3.4 eV	0.88

The transition temperatures are different in three order of magnitude between $^{238}U^{92+}$ and p^+ because of the difference of the Coulomb interaction. However, the variation of Γ_2 parameter is within factor 4 from $^{238}U^{92+}$ to p^+. The difference becomes within twice, except for $^{12}C^{6+}$. This result suggests that the ordering of the highly charged heavy ions and a single charge proton are the same phenomena.

6.1.2 Reflection Probability

The reflection probability was calculated by numerical simulations in Ref.[21, 67]. Let us consider the two particles again in Fig.6.2. If the longitudinal and transverse temperatures are determined, the reflection of the particle depends on the initial betatron phase of each particle. It can be calculated by a Monte Carlo method with various phases. The result is called as "the reflection probability". For example, the probability of 100 % means that the reflection occurs with any initial betatron phase.

The scaling (normalization) is important in order to compare the different ion species with different kinetic energy. The scaling based on the general Hamiltonian formalism was proposed by H. Okamoto [67]. In general, the Hamiltonian of the two particles in the rest frame is,

$$H = \sum_{i=1,2} \left(\frac{p_{xi}^2 + p_{yi}^2 + p_{zi}^2}{2} + \left(\frac{\nu}{R}\right)^2 \frac{x_i^2 + y_i^2}{2} \right) + \frac{r_i}{\beta^2\gamma^2} \frac{1}{\sqrt{(x_1 - x_2)^2 + (y_1 - y_2)^2 + (z_1 - z_2)^2}} \quad (6.7)$$

where ν is the betatron tune, R is the average radius of the ring, r_i is the classical ion radius of $Z^2e^2/4\pi\epsilon_0 m_i c^2$. The first term is the energy of the kinetic motion, the second term describes the betatron oscillation in the transverse directions and the third term is the Coulomb interaction between two particles. He shows that if appropriate scaling and

variables are introduced, the Hamiltonian becomes,

$$\widehat{x} = \frac{\widehat{p_x}^2 + \widehat{p_y}^2 + \widehat{p_z}^2}{2} + \frac{\widehat{x}^2 + \widehat{y}^2}{2} + \frac{1}{\sqrt{\widehat{x}^2 + \widehat{y}^2 + \widehat{z}^2}}. \tag{6.8}$$

It does not include any information of the ions, such as the kinetic energy and ion species. According to this scaling, the beam temperatures are converted to the normalized one from Eqs.(5.2, 5.8),

$$\widehat{T}_{\parallel} = \frac{2}{m_i c^2} \left(2 r_i \beta\gamma \frac{\nu}{R}\right)^{-2/3} k_B T_{\parallel}, \tag{6.9}$$

$$\widehat{T}_{\perp} = \frac{2}{m_i c^2} \left(2 r_i \beta\gamma \frac{\nu}{R}\right)^{-2/3} k_B T_{\perp}. \tag{6.10}$$

Figure 6.3 shows the calculated reflection probability from 100 % to 60 % [67] as a function of the normalized temperatures defined in Eqs.(6.9, 6.10). Figure 6.3 also shows the normalized transition temperature of the proton at S-LSR and those of other ions at ESR [22, 69]. It shows a tendency that the light ions undergo transitions at a lower reflection probability than heavy ions, except for C^{6+}. The reflection probability of the proton at the transition is close to those of the heavy ions. This result also supports the similarity of the ordering between the heavy ions and the proton. The model of the two particle reflection agrees with the experimental results from the highly charged heavy ions to a single charge proton.

At last, I would like to comment the importance of the magnetized electron cooling. If the minimum transverse temperature of the proton is determined by the transverse electron temperature, the transverse proton temperature becomes 34 meV, which corresponds to $\widehat{T}_{\perp}$ of 230. The reflection probability would be close to zero in this case (see Fig.6.3) and the ordering of the proton would never happen. The low transverse temperature of 1 meV by the magnetized electron cooling plays an essential role for the ordering of the proton. In other word, the ordering of the proton is evidence of the magnetized electron cooling. On the other hand, the transition temperatures of the highly charged heavy ions are higher than the transverse temperature of the free electrons (see Table 6.1). Therefore, the importance of the magnetized electron has not been recognized.

6.2 Molecular Dynamics Beam Simulation

6.2.1 Molecular Dynamics Method

One-dimensional ordering has been explained by the two particle collisions. However, the relation between the one-dimensional ordering and the crystalline beam is not clear in this analysis. The formation process of the crystalline beam has been explained from the nature of the intrabeam scattering. The schematic behavior of the heating rate is shown in Fig.6.4. Normally, when the beam is cooled, the beam density increases and the heating rate

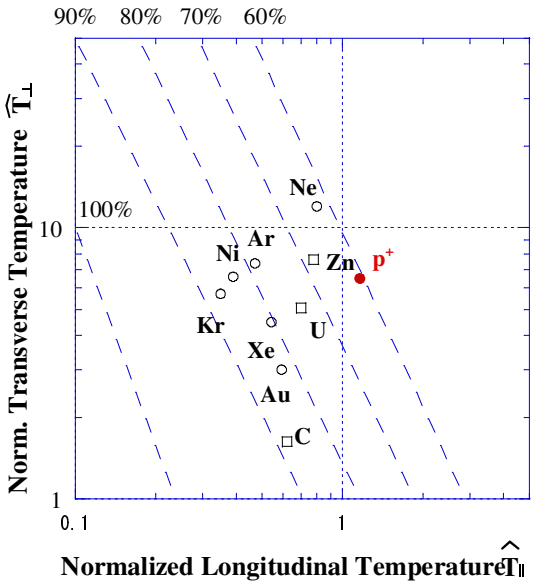

Figure 6.3: Contour plot of the reflection probability in Ref.[67]. The mark of the proton (• p^+) is the present data at S-LSR. Some data points of ions (mark ∘) were extracted from Table 1 in Ref.[69] and three data points (mark □) from Table 1 in Ref.[22].

by the intrabeam scattering also increases. However, from the study of the crystalline beam, it is found that there is a local maximum of the heating rate. When the Coulomb potential exceeds the kinetic energy of the particles in the rest frame below a certain temperature, the scattering between the particles is suppressed and the heating rate decreases. This behavior was calculated by J. Wei and H. Okamoto in Ref.[35]. They used a molecular dynamics (MD) simulation code with the lattice of TARN II and the ions of 1 MeV Mg^+. The heating rate has a local maximum at the beam temperature of around 0.3 K. If the cooling rate is higher than the maximum heating rate, the ion beam temperature is not determined by the IBS heating rate and the final temperature is determined by other reasons. This final lowest temperature state is considered to be an crystalline beam.

However, most of the MD simulations has been performed for the high density beam ($\Gamma > 1$), for example in Ref.[35, 70, 71], because the Coulomb crystal cannot be formed without the strong Coulomb interaction. It is not clear whether such a physical picture is valid for the ultra low density beam, like a one-dimensional ordering. The applications of the MD simulation on the one-dimensional ordering have been performed by some groups, for example in Ref.[72, 73]. At S-LSR, a simulation work has been carried out by A. Smirnov [74]. I described here the comparison of the MD simulation and the experimental results.

For the simulation of the one-dimensional ordering or the crystalline beam, an exact Coulomb interaction must be calculated, because such phenomena are based on the Coulomb

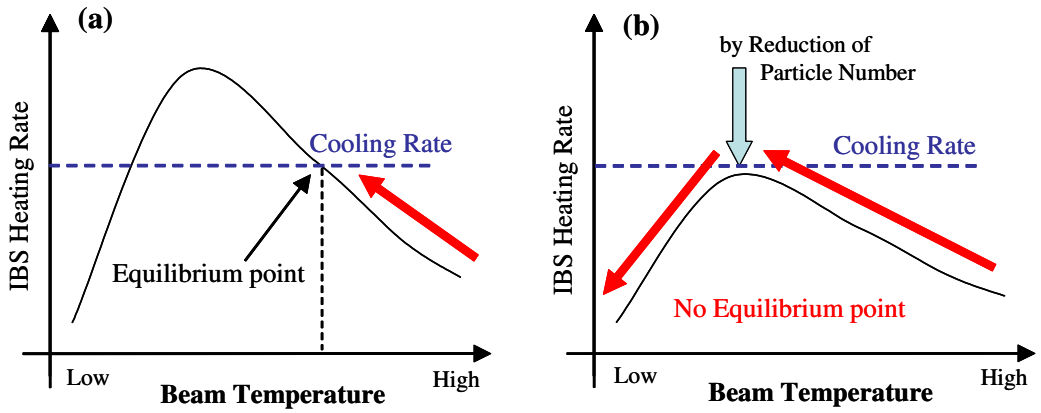

Figure 6.4: Schematic behavior of the heating rate of the intrabeam scattering. The heating rate has a maximum at a certain temperature. When the cooling rate is lower than the maximum heating rate, there is an equilibrium state (a). If the cooling rate is higher than the maximum heating rate, there is no equilibrium state and the beam is cooled down without limitation (b). It is quantitatively calculated by J. Wei and H. Okamoto in Ref.[35].

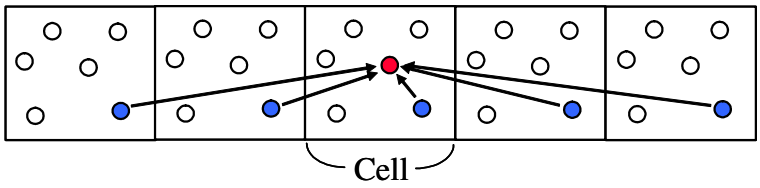

Figure 6.5: Schematic model of the MD method. It is assumed that the particle distribution is periodic and the same in all cells.

interaction between each particle. A macro particle tracking cannot be used, because one model particle represents an ensemble of the real particles. The molecular dynamics (MD) methods is used to treat the interaction accurately. The model of the MD method is shown in Fig.6.5. The ring is divided into the multiple cells. It is assumed that the particle distribution is periodic and the same in all cells. Due to this assumption, we can concentrate the beam dynamics simulation only in one cell and calculate it with the reasonable computing resources.

For the ordering simulation at S-LSR, the particle number in the cell is 6, 8 and 10, which is limited by the tolerable calculation time. The cell length is varied from 10 mm to 100 mm, because the interesting particle number in the ring is from 1000 to 10000. The program code of BETACOOL is used for the simulation, which has a MD simulation mode [54]. The effect of the electron cooling is treated as a constant cooling rate. The momentum spread of each circulating particle is reduced with the constant rate. From Fig.3.14, the cooling coefficient

is 2.1×10^{-5} eVsec/m^2 with the electron current of 25 mA. From Eq.(3.23), the cooling rate is 40 sec^{-1} with η_c of 0.020 at S-LSR.

The other heating sources in the ring, such as a field error of the magnets, a power supply ripple and a scattering with the residual gas are not included in the simulation. The particle motion in the simulation is determined only by the cooling rate, the external magnetic focusing and the Coulomb interaction between particles.

6.2.2 Results of Beam Simulation

In the simulation, the initial emittance is $1\times10^{-3}\pi{\cdot}mm{\cdot}mrad$ and the initial momentum spread is 1×10^{-5}, which are the measured beam parameters at the particle number of 30000. Due to the limitation of the calculation time, it is difficult to use the larger initial parameters. The time evolutions of the momentum spread are shown in Fig.6.6 with the particle number of 2000, 4000 and 6000. The simulation particle number in the cell is 6. With the particle number of 6000, the momentum spread reaches the equilibrium one in a short period and constant during the simulation. With the particle number of 2000, the result is different. The momentum spread decreases monotonically and there is no limit of the lowest momentum spread. The reduction rate of the momentum spread is almost the same as the input cooling rate. The heating of the intrabeam scattering does not limit the momentum spread. With the particle number of 4000, the result is similar to that of the particle number of 2000. The momentum spread stays at a certain value for a short while and then, starts to decrease with the constant cooling rate.

Figure 6.7 shows the trajectory of the cooling process on the space of the horizontal emittance and the momentum spread. The particle numbers are 2000 and 6000, respectively. In both cases, the beams are cooled down along the similar trajectory but the beam with the particle number of 6000 stops at the point with the momentum spread of around 6×10^{-6} and the horizontal emittance of around $10^{-4}\pi{\cdot}mm{\cdot}mrad$. They are almost consistent with the measured beam parameters at the particle number of 6000, which are the momentum spread of 6×10^{-6} and the horizontal emittance of $2\times10^{-4}\pi{\cdot}mm{\cdot}mrad$.

Figure 6.8 shows the final momentum spread obtained by the MD simulation with various particle numbers. The measured momentum spread is also shown in the same figure. The momentum spread drops at the particle number of 4000 in the simulation, while it drops between the particle number of 4000 and 2000 in the measurement. The simulation is globally consistent with the measurement.

These simulation results suggest that the cooling rate is close to the maximum IBS heating rate with the particle number of 4000. At the particle number of 2000, the cooling rate exceeds the maximum heating rate. Concerning the transition, the mechanism in the one-dimensional ordering is the same as that of the crystalline beam. This result also explains why the ordering happens at very small particle number. Because of the small cooling rate of the electron cooling, it can exceed the IBS heating only with the very small particle number.

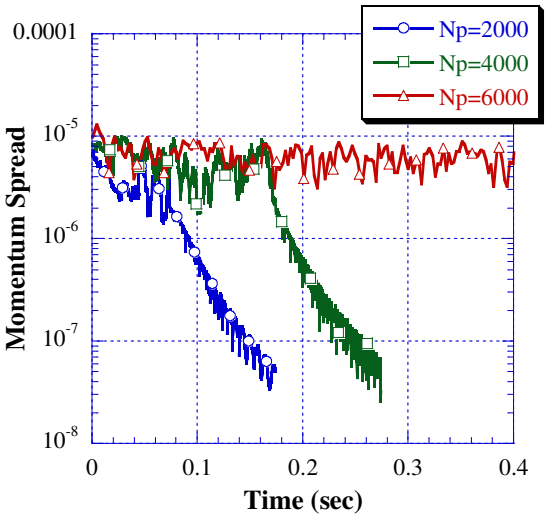

Figure 6.6: Time evolutions of the momentum spread at the particle number of 2000, 4000 and 6000. It was calculated by the MD method of the BETACOOL program.

It is different from the crystalline beam simulation by laser cooling. The laser cooling has a large cooling rate and can overcome the intrabeam scattering even with the large particle number.

6.3 Limit of Beam Temperature

In the previous section, the difference of the transition particle number between the one-dimensional ordering and the crystalline beam is discussed. The other difference is the final temperature. The beam temperature of the crystalline beam in the simulation is less than 0.1 μeV (1 mK), while the lowest temperature below the transition is 26 μeV at S-LSR.

Below the transition, the heating of the intrabeam scattering does not determine the beam temperature. Although the ripple of the power supply for the electron cathode and the bending magnet might affect on the beam temperature, the most probable cause is the temperature of the electron beam. The longitudinal electron temperature $T_{e\|}$ is given by Eq.(3.16),

$$k_B T_{e\|} \cong \frac{(k_B T_{cath})^2}{\beta^2\gamma^2 m_e c^2} + \frac{e^2 n^{1/3}}{4\pi\epsilon_0}. \tag{6.11}$$

It is 20 μeV with the electron current of 25 mA. The measured lowest temperature of the proton is close to this value. The electron itself becomes a heating source below the transition. The cooling of the proton beam stops by the heating of the electron. Due to this thermal energy, the proton moves in the longitudinal direction below the transition. Figure 6.9 shows the particle distribution in x-s plane in the MD simulation. The momentum spread and

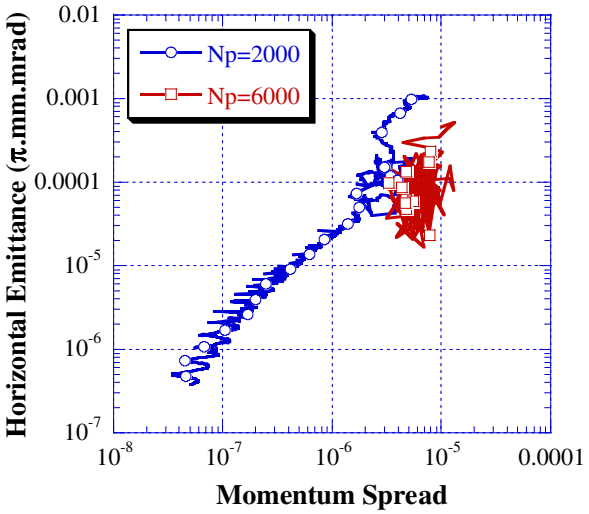

Figure 6.7: Beam trajectory on the phase space of the horizontal emittance and the momentum spread. The particle numbers are 2000 and 6000, respectively.

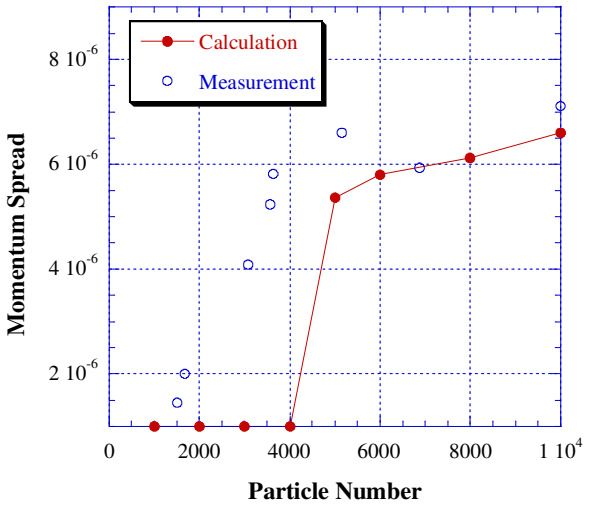

Figure 6.8: Final momentum spread obtained by the MD simulation (mark •) and the measured momentum spread in the experiment (mark ○).

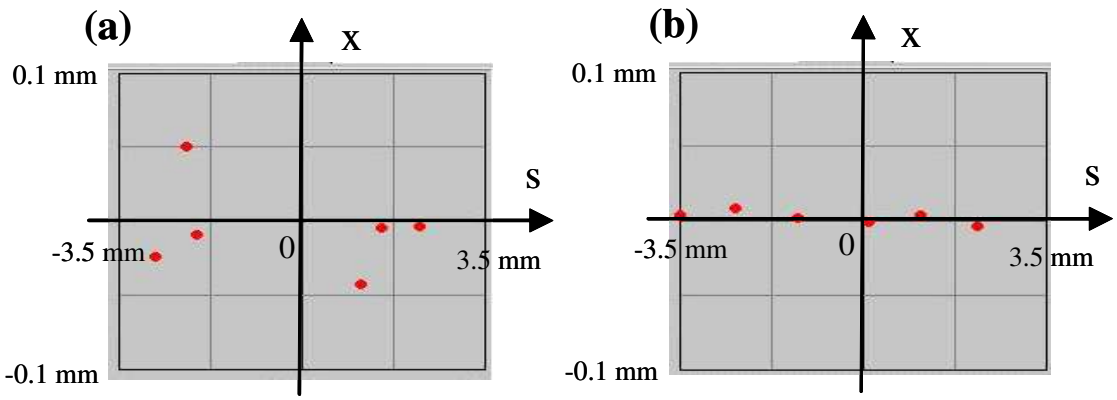

Figure 6.9: Particle distribution in x-s plane in the MD simulation. The momentum spreads are 1×10^{-6} (a) and 1×10^{-7} (b). The horizontal emittances are 2×10^{-5} $\pi{\cdot}mm{\cdot}mrad$ (a) and 2×10^{-6} $\pi{\cdot}mm{\cdot}mrad$.

the emittance are 1×10^{-6} and 2×10^{-5} $\pi{\cdot}mm{\cdot}mrad$ in Fig.6.9(a). There is no longitudinal crossing of the pariticles but the longitudinal position is random. When the proton beam is cooled down to δp/p=1×10^{-7} (0.1 μeV) in Fig.6.9(b), the longitudinal ion motion almost freezes in the particle rest frame and the plasma parameter is around 1 from Eq.(1.6). It would be a real "string".

Chapter 7

Summary

We have constructed the compact ion storage ring, S-LSR at Institute for Chemical Research, Kyoto University. It is a dedicated ring for the ion beam cooling using the electron cooling and the laser cooling. One of the main subjects of S-LSR is the study of the phase transition of the cooled ion beam. In order to realize the extreme cold ion beam, the storage ring has the same importance as the cooling devices. The keyword is the symmetry of the lattice in the ring to suppress the beam heating. Some results of the construction are reported in this thesis, such as the lattice design, the magnetic field error, the alignment of the magnets and the variation of the beam parameters in the ring.

We have performed the one-dimensional ordering experiment for the proton beam at S-LSR since February, 2006. The one-dimensional ion orderings have been observed for the highly charged heavy ions at ESR, SIS and CRYRING. We have succeeded for the first time to observe the abrupt drop of the momentum spread of the proton, when the particle number was decreased to 2000. It is considered to be the phase transition of the one-dimensional proton ordering. Although the phase transition of the transverse temperature is not confirmed due to the limitation of the measurement device, we have demonstrated the very low transverse proton temperature, which is more than 30 times lower than the transverse electron one. It was expected from the magnetized electron cooling theory years ago and this is the first clear experimental verification. It is also important for the study of the electron cooling. The proton ordering has been achieved due to this low transverse temperature.

From the analysis of the particle reflection model, it is found that the transition temperature of the proton coincides with those of the highly charged heavy ions at ESR using the appropriate scaling. It shows that the one-dimensional ordering is the common phenomena of the electron cooled ion beam from the heavy ions to the proton. The experimental result of the proton at NAP-M is considered to be a different phenomenon. The interpretation remains to be solved and we have continued the experimental and the simulation work [64].

The molecular dynamics simulation gives the consistent result with the measurement. It also gives the various information. The abrupt drop of the momentum spread is induced by the fact that the electron cooling rate exceeds the maximum IBS heating rate. The reason

why the one-dimensional ordering occurs only at the very low particle number, is explained by the low electron cooling rate. Below the transition temperature, there is a thermal motion in the particle rest frame but the longitudinal crossing is not observed in the simulation, which is expected from the particle reflection model. If the ion temperature decreases down to 0.1 μeV without the electron heating, the ion motion would freeze and the string crystal might be realized.

Acknowledgements

The presented work has been supported by many people. First of all, I would like to thank to the supervisor Prof. A. Noda in Kyoto University. Not only he has given me many important advises and fruitful discussions, but also he has encouraged me to perform and continue the ordering experiment. I thank to all members of the accelerator group at Institute for Chemical Research, Kyoto University; Prof. Y. Iwashita, Mr. H. Tongu, Dr. T. Takeuchi, Dr. M. Ikegami, Dr. H. Fadil, Dr. S. Nakamura, Dr. A. Yamazaki, Dr. S. Fujimoto, Mr. M. Tanabe, Mr. H. Souda, Mr. H. Itoh and Mr. T. Shintaku. Some of them have already graduated. The fruitful results at S-LSR have been achieved by the contributions of all members. Especially, I am grateful to Mr. H. Souda and Mr. H. Tongu. They have performed the ordering experiment with me and made many contributions to this subject. I am also grateful to Dr. H. Fadil. He has played the important role in the design of the electron cooler and the commissioning of the electron cooling of the proton.

The construction of S-LSR has been performed with the collaboration with National Institute of Radiological Sciences (NIRS) and Accelerator Engineering Corporation (AEC). I would like to thank to Dr. S. Yamada, Dr. K. Noda in NIRS and Dr. S. Shibuya, Mr. T. Fujimoto, Mr. S. Iwata, Mr. H. Fujiwara, Mr. A. Takubo in AEC. Dr. K. Noda always encouraged me to do this work and Mr. S. Iwata joined the ordering experiment.

The electron cooling and the ordering experiment have been performed with the collaboration with Max-Planck-Institut für Kernphysik (MPI-K) and Joint Institute for Nuclear Research (JINR). I would like to thank to Dr. M. Grieser (MPI-K) and Prof. I. Meshkov, Dr. E. Syresin, Dr. A. Smirnov, Dr. I. Seleznev (JINR). Dr. M. Grieser gave us many advices about the electron cooler for S-LSR and I got a lot of experiences of the electron cooling from the TSR experiments with him at MPI-K. Prof. I. Meshkov has encouraged me to do the ordering experiment and given me the fruitful advices. I am very grateful for his support. The ordering simulation by Dr. A. Smirnov has been a guideline of the experiment.

Concerning the lattice design of S-LSR, the beam physics group in Hiroshima University has made the extensive beam simulation work. I am very grateful to Prof. H. Okamoto, Dr. Y. Yuri and Dr. K. Okabe. Prof. H. Okamoto has advised us not only about the crystalline beam, but also about the one-dimensional ordering conditions.

I further thank to Dr. J. Dietrich (Jülich), Dr. M. Wakasugi (Riken) and Dr. F. Caspers

(CERN) for their helpful advices about the measurements, especially for the Schottky noise measurement. The improvement of the measurement according to their advices becomes one of the key of the successful observation. I also thank to Dr. R.W. Hasse (GSI) for his advice about the ordering condition.

And many thanks to Dr. I. Watanabe, Mr. T. Nagafuchi and Mr. E. Ono in TOSHIBA Co. for their invaluable efforts on the electron cooler.

This work has been supported by the Advanced Compact Accelerator Development project by MEXT of the Japanese Government and 21st Century COE at Kyoto University - Diversity and Universality in Physics.

Appendix A

Crystalline Beam

A crystal of one component plasma was studied by E. Wigner [75]. He predicted that the cold electron plasma with low density formed a crystal structure by the Coulomb interaction. Now the crystalline structures of electrons and ions are called "Wigner Crystal". A Wigner crystal of electrons has been observed experimentally above a surface of liquid helium and on a semiconductor. A crystal of ions has been achieved in a trap by a laser cooling [31, 32]. In the ion trap, the ion plasma is confined by the external field and cooled by a laser. When the kinetic energy of ions becomes smaller than the Coulomb potential, ions start to align and form the crystalline structure.

After the successful achievements of the ion crystal in the trap, the possibility of the crystalline beam by the cooling technique was discussed seriously. In the theoretical work, Schiffer and Kienle showed the possibility of Coulomb crystal beam [76] and it was confirmed using molecular dynamics (MD) simulations [77, 78]. In the early study of the crystalline beam, the stability of the crystalline state was mainly discussed. In practice, the beam is cooled from the high temperature state to the cold crystalline state. J. Wei found the necessary conditions of the ring to attain the crystalline beam [33, 35, 79]. It is so called "maintenance conditions", which is discussed in the Section 2.1.1.

In the experimental work, a laser cooling for heavy ion beams were first realized in 1990s at TSR and ASTRID [80, 81]. Be^+ and Li^+ were cooled by the laser at TSR and Li^+ and Mg^+ at ASTRID. They have achieved the very low longitudinal temperature. However, the crystalline beam has not been realized. At S-LSR, the experiment for the crystalline beam using Mg^+ is ongoing using a laser cooling system [82].

The crystalline beam is the ultimate goal of the low temperature state of the ion beam. It has some special features [36],

- Zero beam temperature and zero-emittance,
- Large plasma parameter ($\Gamma \ll 1$),

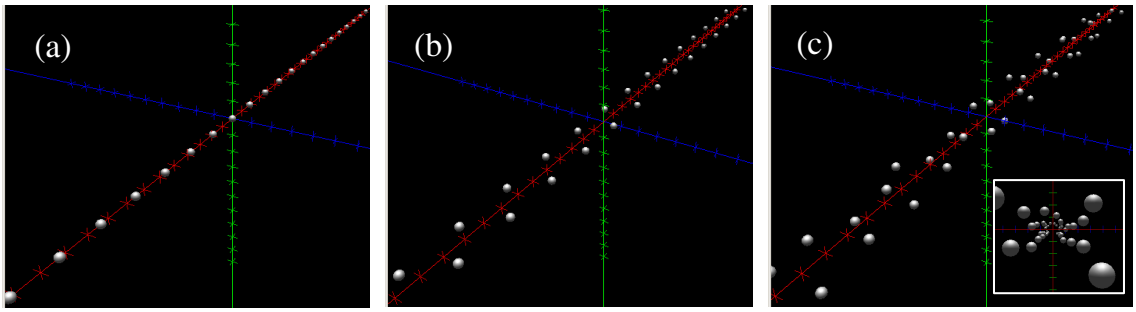

Figure A.1: Results of the molecular dynamics simulation for the crystalline beam. The particle is 35 keV, Mg^+ at S-LSR. The structure is call (a):"String", (b):"Zigzag" and (c):"1-Shell" with the particle density of 5.6×10^4 ions/m, 8.0×10^4 ions/m and 1.1×10^5 ions/m, respectively.

- Particle trajectory $x_n(s)$ is proportional to the function $D(s)$,

$$x_n(s) = c_n D(s), \quad (n = 1, 2, 3, \ \ldots \ N_p), \tag{A.1}$$

  where N_p is the number of the particle and c_n is the constant for each particle.

Figure A.1 shows examples of the calculated crystalline beam [83]. They are results of the molecular dynamics simulations. The particle is 35 keV, Mg^+. The ring is S-LSR with dispersion free mode [30], which cancels the shear force in the dipole magnets. The stable structure of the crystalline beam depends on the particle density. Figure A.1 shows the three kinds of structure, "String", "Zigzag" and "1-Shell (spiral)" with the particle density of 5.6×10^4 ions/m, 8.0×10^4 ions/m and 1.1×10^5 ions/m, respectively.

Appendix B

Transverse Beam Dynamics without Space Charge

B.1 Basics of Particle Motion in Circular Accelerator

At first, let us consider the ideal storage ring without a magnetic field error or a misalignment. It is also assumed the particle motion is on the horizontal plane. The coordinate system is defined in Fig.1.1. In a circular accelerator, a charged particle is focused periodically by magnets. The general behavior of the particle is described by,

$$\frac{d^2x(s)}{ds^2} + K(s)x(s) = \frac{1}{\rho}\frac{\delta p(s)}{p_0}, \tag{B.1}$$

$$K(s) = K(s+L), \tag{B.2}$$

where L is the length of one period of the ring. $K(s)$ is the periodic function and describes the linear focusing of the particle. It usually consists of a radial focusing of bending magnets $(1/\rho^2)$ and a focusing of a quadrupole magnet. The vertical motion is essentially identical with the horizontal one or simpler. Here, only the horizontal motion is considered. When K(s) is constant and $\delta p = 0$, Eq.(B.1) is an equation of the harmonic oscillator. The particle motion is represented by $\sin\left(\sqrt{K}x\right)$ around the reference orbit.

At first, let us consider $\delta p = 0$. Eq.(B.1) becomes,

$$\frac{d^2x(s)}{ds^2} + K(s)x(s) = 0. \tag{B.3}$$

It is a homogeneous Hill equation and has a periodic solution. The general solution of Eq.(B.3) is given by the linear combination of cosine like functions C(s) and sine like function S(s),

$$x(s) = C(s)x(0) + S(s)\frac{dx(0)}{ds}, \tag{B.4}$$

where C(s) and S(s) are two independent solutions of Eq.(B.3),

$$\frac{d^2C(s)}{ds^2} + K(s)C(s) = 0, \tag{B.5}$$

$$\frac{d^2S(s)}{ds^2} + K(s)S(s) = 0. \tag{B.6}$$

When the initial values are defined,

$$C(0) = 1, \quad \frac{dC(0)}{ds} = 0, \quad S(0) = 0, \quad \frac{dS(0)}{ds} = 1, \tag{B.7}$$

the particle orbit x(s), dx(s)/ds is given by the matrix form,

$$\begin{pmatrix} x(s) \\ \frac{dx(s)}{ds} \end{pmatrix} = \begin{pmatrix} C(s) & S(s) \\ \frac{dC(s)}{ds} & \frac{dS(s)}{ds} \end{pmatrix} \begin{pmatrix} x(0) \\ \frac{dx(0)}{ds} \end{pmatrix}. \tag{B.8}$$

This matrix is called "transfer matrix". If the transfer matrix is known, the particle orbit can be derived by the matrix calculation.

From Eq.(B.4), the general solution can be written by the quasi-harmonic form,

$$x(s) = a\sqrt{\beta(s)}\cos\left(\Psi(s) - \Psi_0\right), \tag{B.9}$$

where Ψ_0 is the arbitrary initial phase. $\sqrt{\beta(s)}$ is the amplitude function and β is called "β-function". β-function has the same periodicity as K(s),

$$\beta(s) = \beta(s + L). \tag{B.10}$$

The phase function $\Psi(s)$ is called the "betatron phase". By differentiation,

$$\frac{dx(s)}{ds} = -\frac{a}{\sqrt{\beta(s)}}\left(\alpha\cos\left(\Psi(s) - \Psi_0\right) + \sin\left(\Psi(s) - \Psi_0\right)\right), \tag{B.11}$$

$$\alpha = -\frac{1}{2}\frac{d\beta(s)}{ds}. \tag{B.12}$$

From Eqs.(B.9, B.11), the particle motion in the phase space (x, dx/ds) is on the ellipse. The illustration of the ellipse is shown in Fig.B.1 and the ellipse equation is

$$\gamma x^2 + 2\alpha x\left(\frac{dx}{ds}\right) + \beta\left(\frac{dx}{ds}\right)^2 = a^2, \tag{B.13}$$

$$\gamma = \frac{1 + \alpha^2}{\beta}. \tag{B.14}$$

The area of the ellipse is πa^2 and it is an invariant of the motion. The a^2 is called the "emittance" (ϵ) and these α, β and γ are called the "twiss parameters".

Substituting Eqs.(B.9, B.11) to Eq.(B.3), the relations is obtained,

$$\frac{d\Psi(s)}{ds} = \frac{1}{\beta(s)}, \tag{B.15}$$

$$\frac{1}{2}\beta(s)\frac{d^2\beta(s)}{ds^2} - \frac{1}{4}\left(\frac{d\beta(s)}{ds}\right)^2 + K(s)\beta^2(s) = 0. \tag{B.16}$$

The first relation shows that the advance of the betatron phase is proportional to the inverse of the betatron amplitude. The second equation determines the β-function. Since the beam

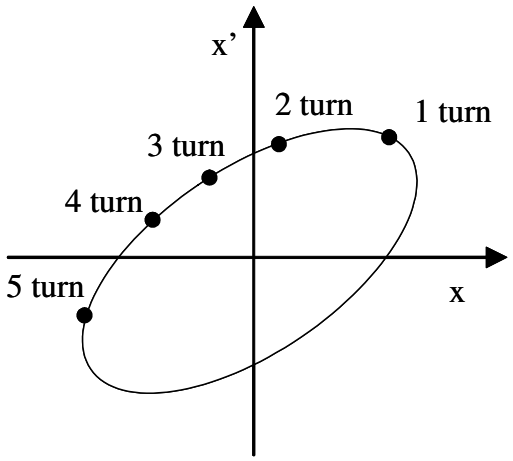

Figure B.1: Coordinate system for particle motion.

envelope $x_m(s)$ is given by $\sqrt{\beta(s)\epsilon}$ from Eq.(B.9), the second equation also determines the beam envelope equation,

$$\frac{d^2x_m(s)}{ds^2} - \frac{\epsilon^2}{x_m(s)^3} + K(s)x_m(s) = 0. \tag{B.17}$$

A betatron tune ν is an important number in a circular accelerator. It is a number of a transverse oscillation around the reference orbit per revolution in the ring. It is defined,

$$\nu = \frac{\Psi(C) - \Psi(0)}{2\pi}, \tag{B.18}$$

$$= \frac{1}{2\pi}\oint_C \frac{1}{\beta(s)}. \tag{B.19}$$

where C is the circumference.

From Eqs.(B.8, B.9, B.11), the transfer matrix of the ring M_0 can be represented by the twiss parameters,

$$M_0 = \begin{pmatrix} \cos\mu + \alpha\sin\mu & \beta\sin\mu \\ -\gamma\sin\mu & \cos\mu - \alpha\sin\mu \end{pmatrix}, \tag{B.20}$$

where μ is the phase advice of the ring. The trace of the transfer matrix is,

$$Trace(M_0) = 2\cos\mu, \tag{B.21}$$

When $Trace(M_0) < 2$, the orbit has a stable solution and the betatron tune ν can be calculated from the trace of the transfer matrix,

$$\nu = \frac{\cos^{-1}\left(Trace(M_0)/2\right)}{2\pi}. \tag{B.22}$$

Next, let us consider a particle with a small momentum deviation. The Hill equation, Eq.(B.1) is the inhomogeneous and a special solution $x_D(s)$ is added. the particle position is

$$x\left(s, \frac{\delta p}{p_0}\right) = x_\beta(s) + x_D(s), \tag{B.23}$$

$$= x_\beta(s) + D(s)\frac{\delta p}{p_0}, \tag{B.24}$$

where D(s) is call the "dispersion function". The first term is the betatron oscillation and the second term is the effect of the momentum deviation. By substituting to Eq.(B.1), the dispersion function must satisfy the equation,

$$\frac{d^2D(s)}{ds^2} + K(s)D(s) = \frac{1}{\rho(s)}, \tag{B.25}$$

$$D(s) = D(s+L). \tag{B.26}$$

The dispersion function is also a periodic solution of the equation. This equation is solved using $\beta(s)$ and $\Psi(s)$,

$$D(s) = \frac{\sqrt{\beta(s)}}{2\sin(\pi\nu)} \oint \frac{\sqrt{\beta(\tau)}}{\rho(\tau)} \cos\left(|\Psi(\tau) - \Psi(s)| - \pi\nu\right) d\tau. \tag{B.27}$$

The particle with a momentum deviation has a different orbit from the reference orbit. The circumference of this particle is

$$C + \delta C = \oint \left(1 + \frac{x_D(s)}{\rho(s)}\right) ds = C + \oint \frac{D(s)}{\rho(s)} ds \frac{\delta p}{p_0}, \tag{B.28}$$

$$\frac{\delta C}{C} = \alpha \frac{\delta p}{p_0}, \tag{B.29}$$

$$\alpha \equiv \frac{1}{C} \oint \frac{D(s)}{\rho(s)} ds. \tag{B.30}$$

This α is called the "momentum compaction factor". The variation of the revolution frequency f_0 is given by

$$\frac{\delta f}{f_0} = \frac{\delta \beta}{\beta} - \frac{\delta C}{C}, \tag{B.31}$$

$$= \left(\frac{1}{\gamma^2} - \alpha\right) \frac{\delta p}{p_0}, \tag{B.32}$$

where γ is the Lorentz factor. The first term is the relativistic effect and the second term is the effect of the difference of the orbit. A Lorentz factor γ_t is defined,

$$\alpha \equiv \frac{1}{\gamma_t^2}. \tag{B.33}$$

The corresponding energy is called "transition energy". When the beam energy is equal to the transition energy, the revolution frequency is independent on the momentum and the phase stability of the synchrotron motion is lost.

B.2 Influence of Field Error and Resonance

Let us consider the effect of a magnetic field error in this section. When there is a dipole field error δB(s) in the ring, the equation of motion is,

$$\frac{d^2x(s)}{ds^2} + K(s)x = \frac{\delta B(s)}{B\rho}, \tag{B.34}$$

where $B\rho$ is the magnetic rigidity. This equation can be solved in the same way as Eq.(B.25),

$$x(s) = \frac{\sqrt{\beta(s)}}{2\sin(\pi\nu)} \oint \frac{\sqrt{\beta(\tau)}\delta B(\tau)}{B\rho} \cos\left(|\Psi(\tau) - \Psi(s)| - \pi\nu\right) d\tau. \tag{B.35}$$

If the field error is localized between $s = s_0 - L/2$ and $s = s_0 + L/2$ and the β-function and the betatron phase is constant in this region,

$$x(s) = \frac{\sqrt{\beta(s)\beta(s_0)}}{2\sin(\pi\nu)} \frac{\delta BL}{B\rho} \cos\left(|\Psi(s_0) - \Psi(s)| - \pi\nu\right). \tag{B.36}$$

This equation gives the closed orbit x(s) in the ring. The particles make the transverse oscillation around this orbit. When the betatron tune ν is close to integer number, the closed orbit becomes large and the particle motion becomes unstable. This is called "integer resonance".

$$\nu = n \quad (n = 1, 2, 3...) \quad ; \; integer \; resonance. \tag{B.37}$$

Next, let us consider a quadrupole field error δK(s) in the ring. The equation of the motion is,

$$\frac{d^2x}{ds^2} + \left(K(s) + \delta K(s)\right) x = 0. \tag{B.38}$$

The transfer matrix of the ring M is written by the ring matrix M_0 without the quadrupole field error,

$$M = mm_0^{-1}M_0, \tag{B.39}$$

where m is the matrix of the error section with the length of ds and the m_0 is the matrix without field error of the same section. Both are,

$$m_0 = \begin{pmatrix} 1 & 0 \\ -K(s)ds & 1 \end{pmatrix}, \qquad m_0 = \begin{pmatrix} 1 & 0 \\ -K(s)ds + \delta K(s)ds & 1 \end{pmatrix}. \tag{B.40}$$

From the matrix formula of m and m_0 and Eq.(B.20),

$$Trace(M) = 2\cos\mu - \beta\delta K(s)ds\sin\mu \tag{B.41}$$

The betatron tune shift by the field error is,

$$\delta\nu = \frac{1}{4\pi}\oint \beta(s)\delta K(s)ds. \tag{B.42}$$

This relation can be used for the measurement of β-function using the artificial field gradient error δK. From the exact calculation of the matrix M, the disturbance of the β-function is derived,

$$\delta\beta(s) = \frac{\beta(s)}{2sin(2\pi\nu)}\oint \beta(\tau)\delta K(\tau)\cos\left(|\Psi(\tau)-\Psi(s)|-2\pi\nu\right)d\tau. \tag{B.43}$$

When the twice of the betatron tune 2ν is close to integer number, the β-function (amplitude of the betatron oscillation) increases and the particle motion becomes unstable. This is called "half integer resonance" or "linear resonance".

$$2\nu = n \quad (n = 1, 2, 3...) \quad ;\ half\ integer\ resonance. \tag{B.44}$$

At the last of this section, I describe about the superperiod. The circular accelerator consists of the repetition of the unit structure of the magnets. One unit structure is called "superperiod". If the symmetry of the superperiod is perfect, the twiss parameter and the transfer matrix become periodic functions of the length of the superperiod L_s,

$$M(s) = M(s + L_s), \tag{B.45}$$

$$\beta(s) = \beta(s + L_s). \tag{B.46}$$

The above resonance conditions in Eqs.(B.37, B.44) are changed to,

$$\frac{\nu}{N_s} = n \quad (n = 1, 2, 3...) \quad ;\ integer\ resonance, \tag{B.47}$$

$$\frac{2\nu}{N_s} = n \quad (n = 1, 2, 3...) \quad ;\ half\ integer\ resonance, \tag{B.48}$$

where N_s is the number of the superperiod. This resonance condition is called "structure resonance". It has stronger effect than other resonances. Since the practical operating tune of S-LSR is between 0.5 and 2.5 with $N_s = 6$, the value of ν/N_s and $2\nu/N_s$ is always less than 1. There is no structure resonance at S-LSR. It is important for the stable operation of the storage ring, especially for the high density beam. The maintenance condition is also based on the similar idea, although the coherent tune in the next section should be considered.

Appendix C

Transverse Beam Dynamics with Space Charge

A single particle motion in an accelerator is described in the previous chapter. It is modified by space charge effects due to the Coulomb field. There are many kinds of effects of the space charge and the related phenomena, such as a tune shift, an envelope instability, a coupling impedance, a two beam instability and an emittance growth. Some effects depend on the total beam charge and others depend on the charge density. The second case is more severe for the cooled beam, because the cooled beam has the high charge density but the beam intensity is not so high in many cases. I discuss the tune shift and the envelope instability in this chapter, which have important effects on the cooled beam.

C.1 Betatron Tune Shift

Let us consider the coasting and the uniform cylinder beam with the particle density of ρ. The electric and magnetic field in the beam are,

$$E_r = \frac{Ze\rho}{2\epsilon_0} r, \tag{C.1}$$

$$B_\phi = \frac{Ze\rho}{2\epsilon_0}\frac{\beta}{c} r. \tag{C.2}$$

The force is,

$$F_{sc} = \frac{Z^2e^2\rho}{2\epsilon_0}(1-\beta^2)r, \tag{C.3}$$

$$= \frac{Z^2e^2\rho}{2\epsilon_0\gamma^2} r. \tag{C.4}$$

When the beam oscillates with the betatron frequency ($\nu\omega_0$), The transverse particle motion is determined by the equation,

$$\frac{d^2x(t)}{dt^2} + (\nu\omega_0)^2 x(t) - \frac{1}{m_i\gamma}\frac{Z^2e^2\rho}{2\epsilon_0\gamma^2} x(t) = 0, \tag{C.5}$$

where ω_0 is the revolution frequency. The tune shift is,

$$\delta\nu = \frac{Z^2 e^2 \rho}{4\epsilon_0 m_i \gamma^3 \nu \omega_0^2}, \tag{C.6}$$

$$= \frac{r_i \lambda}{\beta^2\gamma^3}\frac{R}{\epsilon}, \tag{C.7}$$

$$r_i \equiv \frac{Z^2 e^2}{4\pi\epsilon_0 m_i c^2}, \tag{C.8}$$

where λ is the line density of the beam, R is the average radius of the ring, ϵ is the beam emittance and r_i is the classical ion radius. It represents the tune shift of the individual particle motion and is called "incoherent tune shift".

The resonance conditions in Eq.(B.48) is modified under the space charge to,

$$\frac{\nu - \delta\nu}{N_s} = n \ \ (n = 1, 2, 3...) \quad ; \ integer \ resonance, \tag{C.9}$$

$$\frac{2(\nu - \delta\nu)}{N_s} = n \ \ (n = 1, 2, 3...) \quad ; \ half \ integer \ resonance. \tag{C.10}$$

It shows the possibility that the transverse motion becomes unstable with the space charge, even if the original tune is far from the resonance condition. However, if the operating betatron tune is lower than the lowest resonance condition, the above resonance condition is not satisfied even with the high space charge. The design of S-LSR is based on this idea.

Note that this resonance conditions with the incoherent tune shift are not correct quantitatively, because the beam distribution is changed near the resonance condition. The self-consistent treatment including the beam distribution is necessary for the exact calculation. However, the above discussion is correct qualitatively.

C.2 Beam Envelope Oscillation

Eq.(B.17) gives a beam envelope in an accelerator. The beam envelope (rms beam size) equations with the space charge were given by F. J. Sacherer [84],

$$\frac{d^2\bar{x}(s)}{ds^2} - \frac{\epsilon_{rms}^2}{\bar{x}(s)^3} + K(s)\bar{x}(s) + \frac{r_i}{\beta^2\gamma^3}\frac{\lambda}{\bar{x}(s) + \bar{y}(s)} = 0, \tag{C.11}$$

$$\frac{d^2\bar{y}(s)}{ds^2} - \frac{\epsilon_{rms}^2}{\bar{y}(s)^3} + K(s)\bar{y}(s) + \frac{r_i}{\beta^2\gamma^3}\frac{\lambda}{\bar{x}(s) + \bar{y}(s)} = 0, \tag{C.12}$$

$$\bar{x}(s) \equiv \sqrt{\langle (x^2(s)\rangle}, \tag{C.13}$$

$$\bar{y}(s) \equiv \sqrt{\langle (y^2(s)\rangle}, \tag{C.14}$$

where ϵ_{rms} is the rms emittance and λ is the line density of the beam. For the simplicity, Assuming an axisymmetric beam with $\bar{x}(s) = \bar{y}(s) = \bar{r}(s)$,

$$\frac{d^2\bar{r}(s)}{ds^2} - \frac{\epsilon_{rms}^2}{\bar{r}(s)^3} + K(s)\bar{r}(s) + \frac{r_i}{\beta^2\gamma^3}\frac{\lambda}{2\bar{r}(s)} = 0. \tag{C.15}$$

This equation determines the beam envelope with the space charge. If the beam is not matched to the lattice of the ring, the envelope radius becomes a periodically varying function of distance s. This oscillation also resonates with the lattice structure under the similar conditions. The number of the oscillation is called "coherent tune" ν_c. The resonance instability of the beam envelope is called "envelope instability".

With the space charge, the coherent tune also decreases. The coherent tune shift is evaluated here. The envelope equation can be linearized for the small amplitude of the oscillation $\delta(s)$ due to the mismatching,

$$\bar{r}(s) = a(s) + \delta(s), \tag{C.16}$$

where a(s) is the matched beam envelope and $\delta(s) \ll a(s)$. The linearized equation is,

$$\frac{d^2\delta(s)}{ds^2} + \left(3\frac{\epsilon_{rms}^2}{a^4} + K(s) + \frac{r_i}{\beta^2\gamma^3}\frac{\lambda}{2a^2}\right)\delta(s) = 0. \tag{C.17}$$

In the limit of zero intensity ($\lambda \sim 0$), we have $\nu_c = 2\nu_0$. For a space charge dominated beam. we obtain $\nu_c = \sqrt{2}\nu_0$. It represents that the coherent tune of the envelope oscillation is varied from $2\nu_0$ to $\sqrt{2}\nu_0$ due to the space charge effect.

From Eq.(B.17), the following condition of the coherent tune is necessary for the stability of the beam envelope with the high space charge,

$$\frac{2\nu_c}{N_s} = \frac{2(\sqrt{2}\nu_0)}{N_s} = 1 \quad ; \textit{lowest half integer resonance.} \tag{C.18}$$

This is a part of "maintenance condition". However, this condition guarantees only the stability of the final state. The more strict condition is necessary to guarantee the beam stability during the whole process from $2\nu_0$ to $\sqrt{2}\nu_0$,

$$\frac{2\nu_c}{N_s} = \frac{2(2\nu_0)}{N_s} = 1 \quad ; \textit{lowest half integer resonance.} \tag{C.19}$$

The more exact treatment has been carried out using the Vlasov-Poisson equation by the numerical method [85]. The result is consistent with the discussion in this section.

Appendix D

Electron Cooling Force

Let us consider the collision between the electron and the ion in the particle rest frame without magnetic field (see Fig.D.1). The ion is at the position ($-\infty$, b) with a velocity of $\vec{v_i} = v_i\vec{u_\parallel}$ and the electron is rest at (0, 0) at first. After the scattering, the ion is scattered with the angle Ψ,

$$\cot\left(\frac{\Psi}{2}\right) = -\frac{bm_e v_i^2 4\pi\epsilon_0}{Ze^2}. \tag{D.1}$$

The momentum transfer $\delta\vec{p}$ is

$$\delta\vec{p} = \int_{-\infty}^{\infty} \frac{Ze^2}{4\pi\epsilon_0}\frac{1}{d^2}\vec{u}dt, \tag{D.2}$$

$$where \quad \vec{u} = \frac{-s}{\sqrt{s^2+b^2}}\vec{u_\parallel} + \frac{-b}{\sqrt{s^2+b^2}}\vec{u_\perp}. \tag{D.3}$$

For the small scattering angle, the longitudinal momentum transfer is negligible. Since $s = v_i t$, the transverse momentum transfer $\delta p_\perp$ is

$$\delta p_\perp = \frac{-Ze^2 b}{4\pi\epsilon_0}\int_{-\infty}^{\infty}\frac{dt}{((v_i t)^2+b^2)^{3/2}} = \frac{-2Ze^2}{4\pi\epsilon_0 b v_i}, \tag{D.4}$$

where b is called "impact parameter". The energy loss of the ion $\delta E(b)$ is equal to the energy gain of the electron,

$$\delta E(b) = \frac{(\delta p)^2}{2m_e} = \frac{2Z^2e^4}{(4\pi\epsilon_0)^2 m_e b^2 v_i^2}. \tag{D.5}$$

This is an energy transfer by a single scattering. I have to integrate all possible scattering (see Fig.D.2).

$$\delta E = \int_{b_{min}}^{b_{min}} \delta E(b)dn = \int_{b_{min}}^{b_{min}} \delta E(b) 2\pi b n_e ds db, \tag{D.6}$$

$$= \frac{4\pi Z^2 e^4}{(4\pi\epsilon_0)^2 m_e v_i^2} n_e \ln\left(\frac{b_{max}}{b_{min}}\right), \tag{D.7}$$

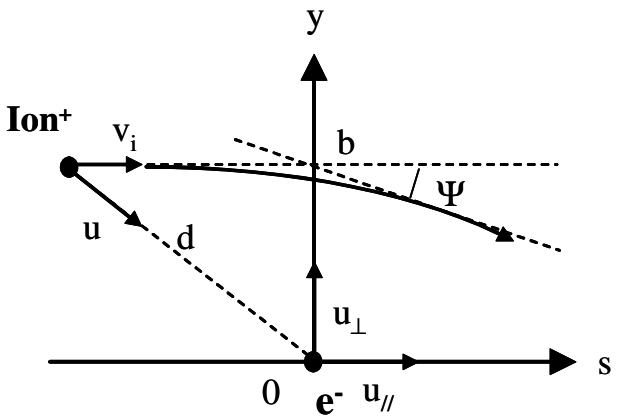

Figure D.1: Geometry of the collision between the electron and the ion.

where n_e is the electron density. The value of $L_c = \ln(b_{max}/b_{min})$ is called "Coulomb logarithm". The value of b_{min} can be estimated by the maximum momentum transfer (so called head-on collision).

$$\frac{2Ze^2}{4\pi\epsilon_0 b_{min} v_i} = \delta p_{max} = 2m_e v_i, \tag{D.8}$$

$$b_{min} = \frac{Ze^2}{4\pi\epsilon_0 m_e v_i^2}. \tag{D.9}$$

The maximum impact parameter is equal to the Debye shielding length,

$$b_{max} = \sqrt{\frac{\epsilon_0 k_B T_e}{n_e e^2}}, \tag{D.10}$$

where T_e is the electron temperature. The Coulomb logarithm has a logarithmically dependence on v_i and it can be considered to be constant.

From Eq.(D.7), the electron cooling force $F_c(v_i)$ is given by,

$$\vec{F_c}(v_i) = -\frac{4\pi Z^2 e^4}{(4\pi\epsilon_0)^2 m_e} L_c n_e \frac{\vec{v_i}}{v_i^3}. \tag{D.11}$$

The cooling force is proportional to v_i^{-2}. It represents that the cooling force is strong for the ion beam with the small velocity spread.

The cooling force in Eq.(D.11) ignores the electron temperature. In practice, the electron beam has a velocity spread $f(v_e)$. I assume the Gaussian form,

$$f(v_e) = \frac{\exp\left(-\frac{v_{e\parallel}^2}{2\Delta_{e\parallel}^2} - \frac{v_{e\perp}^2}{2\Delta_{e\perp}^2}\right)}{(2\pi)^{3/2}\Delta_{e\perp}^2\Delta_{e\parallel}}, \tag{D.12}$$

$$where \quad \Delta_{e\parallel}^2 = \frac{k_B T_{e\parallel}}{m_e}, \quad \Delta_{e\perp}^2 = \frac{k_B T_{e\perp}}{m_e}. \tag{D.13}$$

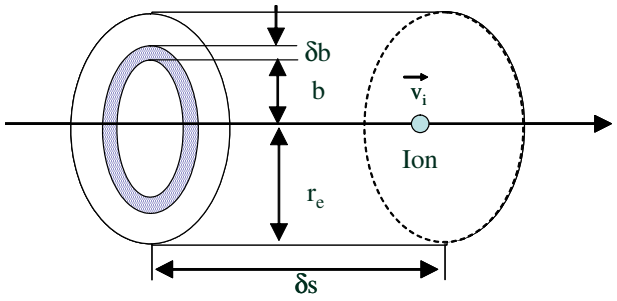

Figure D.2: Geometry of the ion particle in the electron beam.

The friction force $\vec{F}$ is

$$\vec{F}(v_i) = \frac{4\pi Z^2 e^4}{(4\pi\epsilon_0)^2 m_e} L_c n_e \int \frac{\vec{v_i} - \vec{v_e}}{|\vec{v_i} - \vec{v_e}|^3} f(v_e) d^3 v_e. \tag{D.14}$$

From this equation, the asymptotic expressions can be derived for the small ion velocity spread,

$$F_{\parallel}(v_{i\parallel}) = -\frac{4\pi Z^2 e^4}{(4\pi\epsilon_0)^2 m_e} L_c n_e \frac{1}{(2\pi)^{3/2} \Delta_{e\perp} \Delta_{e\perp}^2} v_{i\parallel} \quad ; \; |v_{i\parallel}| << \Delta_{e\parallel}, \tag{D.15}$$

$$F_{\perp}(v_{i\perp}) = -\frac{4\pi Z^2 e^4}{(4\pi\epsilon_0)^2 m_e} L_c n_e \frac{\sqrt{\pi}}{8\Delta_{e\perp}^3} v_{i\perp} \quad ; \; |v_{i\perp}| << \Delta_{e\perp}. \tag{D.16}$$

It shows that the cooling force is linear for the ion beam with the small velocity spread.

Bibliography

[1] G. Budker: "An effective method of damping particle oscillation in proton and antiproton storage ring", Soviet Atomic Energy, **22**, p. 346 (1967).

[2] G. Budker, et al.: "Experimental studies of electron cooling", Particle Accelerators, **7**, p. 197 (1976).

[3] M. BELLL, et al.: "Electron cooling in ice at cern", Nuclear Instruments and Methods in Physics Research Section A, **190**, p. 237 (1981).

[4] R. Forster: "Electron cooling experiments at fermilab", IEEE Transactions on Nuclear Science, **28**, p. 2386 (1981).

[5] S. van der Meer: "Stochastic damping of betatron oscillations in the isr", CERN Report No. ISR-PO-72/31 (1974).

[6] S. van der Meer: "Stochastic cooling and the accumulation of antiprotons", CERN Report No. PS/84-32 (1978).

[7] "The muon ionisation cooling experiment (mice)". http://hepunx.rl.ac.uk/uknf/mice/.

[8] A. A. Mikhailichenko and M. S. Zolotorev: "Optical stochastic cooling", Physical Review Letters, **71**, p. 4146 (1993).

[9] "Osc activities at bates". http://filburt.lns.mit.edu/accelphy/OSC/osc.html.

[10] S. Nagaitsev, et al.: "Experimental demonstration of relativistic electron cooling", Physical Review Letters, **96**, p. 044801 (2006).

[11] F. Sprenger, et al.: "The high resolution electron-ion collision facility at tsr", Nuclear Instruments and Methods in Physics Research Section A, **532**, p. 298 (2004).

[12] D. Möhl: "A comparison between electron cooling and stochstic cooling", Proceedings of Workshop on Electron Cooling and Related Applications (ECOOL84), Karlsruhe, edited by H. Poth, KfK Report No. 3846, p. 293 (1984).

[13] R. E. Pollock: "Some performance predictions for the iucf cooler", Proceedings of Workshop on Electron Cooling and Related Applications (ECOOL84), Karlsruhe, edited by H. Poth, KfK Report No. 3846, p. 109 (1984).

[14] S. Martin: "European cooler storage rings", Proceedings of Workshop on Electron Cooling and Related Applications (ECOOL84), Karlsruhe, edited by H. Poth, KfK Report No. 3846, p. 123 (1984).

[15] T. Tanabe: "Electron cooling project at ins", Proceedings of Workshop on Electron Cooling and Related Applications (ECOOL84), Karlsruhe, edited by H. Poth, KfK Report No. 3846, p. 127 (1984).

[16] V. V. Parkhomchuk: "Physics of fast electron cooling", Proceedings of Workshop on Electron Cooling and Related Applications (ECOOL84), Karlsruhe, edited by H. Poth, KfK Report No. 3846, p. 71 (1984).

[17] A. Piwinski: "Intrabeam scattering", Proceedings of Nineth International Conference on High Energy Accelerators, p. 297 (1974).

[18] M. Steck, K. Beckert, H. Eickhoff, B. Franzke, F. Nolden, H. Reich, B. Schlitt and T. Winkler: "Anomalous temperature reduction of electron-cooled heavy ion beams in the storage ring esr", Physical Review Letters, **77**, p. 3803 (1996).

[19] H. Danared, A. Kallberg, K. G. Rensfelt and A. Simonsson: "Model and observations of schottky-noise suppression in a cold heavy-ion beam", Physical Review Letters, **88**, p. 174801 (2002).

[20] M. Steck and R. W. Hasse: "Ordered ion beams", Proceedings of European Particle Acclerator Conference (EPAC), Vienna, p. 274 (2000).

[21] R. W. Hasse: "Theoretical verification of coulomb order of ions in a storage ring", Physical Review Letters, **83**, p. 3430 (1999).

[22] M. Steck, P. Beller, K. Beckert, B. Franzke and F. Nolden: "Electron cooling experiments at the esr", Nuclear Instruments and Methods in Physics Research Section A, **532**, p. 357 (2004).

[23] J. Dietrich, et al.: "Studies of beam dynamics in cooler rings", Proceedings of Workshop on Beam Cooling and Related Topics (COOL05), Galena, edited by S. Nagaitsev, p. 154 (2005).

[24] A. Noda: "Ion beam cooling at s-lsr project", Nuclear Instruments and Methods in Physics Research Section A, **532**, p. 150 (2004).

[25] T. Shirai, et al.: "One dimensional beam ordering of protons in a storage ring", Physical Review Letters, **98**, p. 204801 (2007).

[26] H. Tongu, et al.: "Vacuum and beam lifetime in s-lsr", Proceedings of 3rd Japanese Accelerator Society Meeting, Sendai, edited by K.Hama, p. 687 (2006).

[27] A. Smirnov: "private communication".

[28] S. P. Moller: "Elisa, and electrostatic storage ring for atomic physics", Nuclear Instruments and Methods in Physics Research Section A, **394**, p. 281 (1997).

[29] T. Tanabe, K. Chida, K. Noda and I. Watanabe: "An electrostatic storage ring for atomic and molecular science", Nuclear Instruments and Methods in Physics Research Section A, **482**, p. 595 (2002).

[30] M. Ikegami: "Beam Dynamics in a Dispersionless Ion Storage Ring", PhD thesis, Kyoto University (2005).

[31] F. Diedrich, et al.: "Observation of a phase transition of stored laser-cooled ions", Physical Review Letters, **59**, p. 2931 (1987).

[32] D. Wineland, et al.: "Atomic-ion coulomb clusters in an ion trap", Physical Review Letters., **59**, p. 2935 (1987).

[33] J. Wei, X. Li and A. M. Sessler: "Low energy state of circulating stored ion beams: Crystalline beam", Physical Review Letters, **73**, p. 3089 (1994).

[34] L. Tecchio, et al.: "A storage ring for crystalline beam studies", Nuclear Instruments and Methods in Physics Research Section A, **395**, p. 147 (1997).

[35] J. Wei, H. Okamoto and A. M. Sessler: "Necessary conditions for attaining a crystalline beam", Physical Review Letters, **80**, p. 2606 (1998).

[36] H. Okamoto and J. Wei: "Theory of tapered cooling", Physical Review E, **58**, p. 3817 (1998).

[37] A. Noda, M. Ikegami and T. Shirai: "Approach to ordered structure of the beam at s-lsr", New Journal of Physics, **8**, p. 288 (2006).

[38] T. Shirai, et al.: "Design of new compact cooler ring at icr, kyoto university", Proceedings of the Workshop on Ion Beam Cooling Toward the Crystalline Beam, Uji, edited by A.Noda and T.Shirai, p. 29 (2001).

[39] "Computer program mad (methodical accelerator design)". http://mad.web.cern.ch/mad/mad8web/mad8.html.

[40] H. Fadil, et al.: "Design of a compact electron cooler for the s-lsr", Nuclear Instruments and Methods in Physics Research Section A, **532**, p. 446 (2004).

[41] T. Takeuchi, et al.: "Optimization of lattice quadrupole magnets for cooler ring, s-lsr", Nuclear Instruments and Methods in Physics Research Section A, **532**, p. 497 (2004).

[42] M. Ikegami, et al.: "Field measurement of bending magnets for s-lsr", Beam Science and Technology, **9**, p. 20 (2005).

[43] T. Takeuchi, et al.: "Magneic field measurement, and indivudual characteristics of quadrupole magnets for s-lsr", Beam Science and Technology, **9**, p. 31 (2005).

[44] H. Okamoto, A. M. Sessler and D. Mohlr: "Three-dimensional laser cooling of stored and circulating ion beams by means of a coupling cavity", Physical Review Letters, **72**, p. 3977 (1994).

[45] J. Wei and A. M. Sessler: "Sensitivity studies of crystalline beams", Proceedings of European Particle Acclerator Conference (EPAC), Sitges, p. 1179 (1996).

[46] "Vector fields ltd.". http://www.vectorfields.com/tosca.htm.

[47] "Group3 technology ltd.". http://maple.he.net/ group3/.

[48] H. Souda, et al.: "Magnets arrangement of s-lsr", Beam Science and Technology, **9**, p. 38 (2005).

[49] S. Fujimoto: "Beam Commissioning and Suppression of Transverse Coherent Instability at S-LSR", PhD thesis, Kyoto University (2007).

[50] H. Fadil: "Electron Cooling of Hot Ion Beeams", PhD thesis, Kyoto University (2005).

[51] H. Danared, et al.: "Electron cooling with an ultracold electron beam", Physical Review Letters, **72**, p. 3775 (1994).

[52] I. Meshkov: "Electron cooling: Status and perspectives", Physics of Particles and Nuclei, **25**, p. 631 (1994).

[53] Y. S. Derbenev and A. N. Skrinskii: "The physics of electron cooling", Physics Reviews (Soviet Scientific Reviews), **3**, p. 165 (1981).

[54] I. Meshkov, et al.: "Physics guide of betacool code version 1.1", BNL Note C-A/AP/262 (2006).

[55] V. V. Parkhomchuk, et al.: "Development of a new generation of coolers with a hollow electron beam and electrostatic bending", Proceedings of Workshop on Beam Cooling and Related Topics (COOL05), Galena, edited by S. Nagaitsev, p. 249 (2005).

[56] T. Shirai, et al.: "Commisioning of electron beam cooling at s-lsr", Proceedings of 39th ICFA Advanced Beam Dynamics Workshop on High Intensity High Brightness Hadron Beams, HB2006, Tsukuba, edited by Y.Chin and H.Yoshikawa, p. 247 (2006).

[57] C. Ellert, et al.: "An induction accelerator for the heidelberg test storage ring tsr", Nuclear Instruments and Methods in Physics Research Section A, **314**, p. 399 (2004).

[58] H. Fujiwara, et al.: "S-lsr control system", Proceedings of 3rd Japanese Accelerator Society Meeting, Sendai, edited by K.Hama, p. 935 (2006).

[59] B. Hochadel, et al.: "A residual-gas ionization beam profile monitor for the heidelberg test storage ring tsr", Nuclear Instruments and Methods in Physics Research Section A, **343**, p. 401 (1994).

[60] K. Kleinknecht: "Detectors For Particle Radiation", Cambridge University Press (1987).

[61] H. Yonehara, N. Tokuda, M. Yoshizawa and T. Hattori: "Equipments for momentum cooling at tarn", INS Report No. INS-NUMA-49 (1983).

[62] F. J. Sacherer: "Stochastic cooling theory", CERN Report No. ISR-TH/78-11 (1978).

[63] V. V. Parkhomchuk and D. V. Pestrikov: "Thermal noise in an intense beam in a storage ring", Sov. Phys. Tech. Phys, **25**, p. 818 (1980).

[64] A. Smirnov, et al.: "Investigation of ordered proton beams at s-lsr", HIMAC Report (to be published) (2007).

[65] I. Meshkov, A. Sidorin, A. Smirnov and E. Syresin: "Ordered state of ion beams", Riken Report No. RIKEN-AF-AC-34 (2002).

[66] I. Meshkov, et al.: "Numerical simulation of crystalline ion beams in storage ring", Nuclear Instruments and Methods in Physics Research Section A, **532**, p. 376 (2004).

[67] H. Okamoto, K. Okabe, Y. Yuri, D. Mohl and A. M. Sessler: "One-dimensional ordering of ultra-low-density ion beams in a storage ring", Physical Review E, **69**, p. 066504 (2004).

[68] I. Meshkov: "private communication".

[69] R. W. Hasse: "Coulomb strings in heavy ion storage rings: explanation and stability criteria", Nuclear Instruments and Methods in Physics Research Section A, **532**, p. 382 (2004).

[70] Y. Yuri and H. Okamoto: "Generating ultralow-emittance ion beams in a storage ring", Physical Review Letters, **93**, p. 204801 (2004).

[71] M. Ikegami, H. Okamoto and Y. Yuri: "Crystalline beams in dispersion-free storage rings", Physical Review ST Accel. Beams, **9**, p. 124201 (2006).

[72] H. Tsutsui, et al.: "Md simulation of beam ordering", Nuclear Instruments and Methods in Physics Research Section A, **532**, p. 371 (2004).

[73] I. Meshkov, et al.: "Simulation of crystalline beams in storage rings using molecular dynamics technique", Nuclear Instruments and Methods in Physics Research Section A, **558**, p. 303 (2006).

[74] A. Smirnov, A. Noda, T. Shirai and M. Ikegami: "Crystalline beams at s-lsr", Beam Science and Technology, **10**, p. 6 (2006).

[75] E. Wigner: "On the interaction of electrons in metals", Physical Review, **46**, p. 1002 (1934).

[76] J. P. Schiffer and P. Kienle: "Coud there be an ordered condensed state in beams of fully stripped heavy ions", Zeitschrift for Physik A, **321**, p. 181 (1985).

[77] A. Rahman and J. P. Schiffer: "The structure of the cylindrically confined coulomb lattice", Physical Review Letters, **57**, p. 1133 (1986).

[78] R. W. Hasse and J. P. Schiffer: "Structure of a one-component plasma in an external field: A molecular-dynamics study of a particle arrangement in a heavy-ion storage ring", Annals of Physics, **57**, p. 1133 (1990).

[79] M. Seurer, C. Toepffer, V. Variale, A. Pisent, L. Tecchio and A. Burov: "Cooling of particle beams: Intrabeam scattering, envelope instability and shear", Nuclear Instruments and Methods in Physics Research Section A, **395**, p. 275 (1997).

[80] S. Schröder, et al.: "First laser cooling of relativistic ions in a storage ring", Physical Review Letters, **64**, p. 2901 (1990).

[81] J. S. Hangst, et al.: "Laser cooling of a stored ion beam to 1mk", Physical Review Letters, **67**, p. 1238 (1991).

[82] M. Tanabe, et al.: "Status of the storage of mg+ beam at s-lsr", Proceedings of 3rd Japanese Accelerator Society Meeting, Sendai, edited by K.Hama, p. 600 (2006).

[83] H. Shintaku: "Extraction of the crystalline beam", Master's thesis, Kyoto University (2007).

[84] F. J. Sacherer: "Rms envelope equation with space charge", IEEE Transactions on Nuclear Science, **18**, p. 1105 (1971).

[85] H. Okamoto, K. Okabe and Y. Yuri: "On the maintenance condition of a crystalline beam", Proceedings of European Particle Acclerator Conference (EPAC), Paris, p. 1389 (2002).